The Seen & the Unseen:
from X-ray Binary Catalogues
to Probabilistic Noise-Processing Techniques

Dissertation

der Mathematisch-Naturwissenschaftlichen Fakultät

der Eberhard Karls Universität Tübingen

zur Erlangung des Grades eines

Doktors der Naturwissenschaften

(Dr. rer. nat.)

vorgelegt von

Marvin Janis Neumann

aus Filderstadt

Tübingen

2025

Gedruckt mit Genehmigung der Mathematisch-Naturwissenschaftlichen Fakultät der Eberhard Karls Universität Tübingen.

Tag der mündlichen Qualifikation:	21.01.2026
Dekan:	Prof. Dr. Thilo Stehle
1. Berichterstatter/-in:	Prof. Dott. Andrea Santangelo
2. Berichterstatter/-in:	Prof. Dr. Klaus Werner

To my mother Elisabeth and my grandmother Mechthilde,
who sparked my interest in the Universe at a very young age.

Abstract

X-ray astronomy provides a unique window into the most energetic and extreme processes in the universe. In particular, compact objects such as neutron stars, or black holes accreting matter from a companion star serving as a natural laboratory for stellar evolution, accretion processes, behavior of matter in strong magnetic fields, and much more. An accurate background modeling is essential for extracting astrophysical signals, especially faint signals in X-ray observations. This thesis consists of two separate parts, the first part is about catalogues of X-ray binaries, the second part presents a novel method to deal with the unwanted background.

The first part of this thesis deals with the X-ray binaries which are known to be a possible endpoint of stellar evolution. These systems consist of compact objects, e.g. neutron stars or black holes, and a non-degenerated companion. Depending on the mass of the companion, the system is classified into two different class. If the mass of the companion is below one solar mass the systems are classified as Low Mass X-ray Binaries (LMXBs), while above eight solar masses they are classified as High Mass X-ray Binaries (HMXBs). In such highly energetic systems, the compact object accretes from the companion, emitting large amount of energies in the X-rays. A variety of such systems are known within and outside our galaxy. It is therefore crucial to create a catalogue containing such a system, specially for a population study. Numerous known catalogues have been created in the past, and most recently between 2003 and 2007 for galactic HMXBs and LMXBs (Liu et al., 2006, 2007; Ritter and Kolb, 2003). Since then, new systems have been discovered and parameters of known systems have changed. The goal of the first project was to publish new catalogues of HMXBs and LMXBs, in cooperation with Dr. Avakyan. This project resulted in two publications (Neumann et al. (2023), and Avakyan et al. (2023)) and a website containing both catalogues, providing users an opportunity to explore them interactively.

The second project deals with new, and alternative method to reduce background in the XMM-Newton observations. Already established methods have their own benefits but also downsides. The simple subtraction of a constant background value might not be computationally demanding; however, in the regime of low count rates, this technique can result in an unphysical negative count. An alternative is to model the source and background, which can yield a more significant result than simple subtraction; however, it is more computationally demanding and requires a prior knowledge of the source which is not always possible, especially for a new object. To deal with such shortcomings of the existing methods, the technique explained in this

part uses a probabilistic approach, which prevents a negative source count and does not require prior knowledge of the object. Since the probabilistic technique needs an estimated background, part of the project was to develop images in different energy ranges which can be used to estimate the background in later observations. Then the technique was first tested on the artificial data and then applied to real observations to evaluate its performance.

Zusammenfassung

Röntgenastronomie bietet die Möglichkeit, Einblicke in die extremsten und energiereichsten Prozesse des Universums zu erhalten. Im speziellen bieten sich Systeme, in denen ein kompaktes Objekt wie ein Neutronen Stern oder ein Schwarzes Loch Materie von einem Begleitstern akkretiert, als natürliches Labor an, um stellare Evolution, Akkretionsprozesse, das Verhalten von Materie in extremen Magnetfeldern und vieles mehr zu untersuchen. Zur gleichen Zeit, ist aber auch eine möglichst genaue Modellierung des Hintergrunds wichtig, zum extrahieren von astrophysikalischen Signalen, besonders für sehr schwache Signale. Deswegen besteht diese Arbeit aus zwei seperaten Teilen. Während es im ersten Teil um Kataloge von Röntgendoppelsternsysteme geht, beschäftigt sich der zweite Teil mit einer neuartigen Methode um Beobachtungen von ungewolltem Hintergrund zu bereinigen.

Wie bereits früher erwähnt, beschäftigt sich das erste Projekt mit Röntgendoppelstern Systemen, welche Endpunkte der stellaren Entwicklung seinen können. Diese Art von Systemen beherbergen ein kompaktes Objekt wie zum Beispiel einen Neutronenstern oder ein schwarzes Loch, sowie einen nicht degenerierten Begleitstern. Abhängig von der Masse des Begleitsterns kann man diese Systeme in zwei Klassen unterteilen. Ist die Masse des Begleitsterns geringer als eine Sonnenmasse so spricht man von einem Röntgendoppelstern System mit geringer Masse (LMXBs). Sollte die Masse des Begleitsterns jedoch größer als acht Sonnenmassen sein so klassifiziert man das System als Röntgendoppelsternsystem mit hoher Masse (HMXBs). Da die kompakten Objekte zumeinst von ihrem Begleitstern Materie akkretieren, und dies zur Freisetzung großer Energiemengen führt, sind diese Objekte meist im Röntgenbereich beobachtbar. Heutzutage ist eine Vielzahl dieser Systeme bekannt sowohl innerhalb unsere Galaxie wie auch außerhalb. Deshalb ist es notwendig für Bevölkerungsstudien diese Systeme zu katalogisieren. Diese Katalogisierung wurde bereits in der Vergangenheit durchgeführt, jedoch zuletzt zwischen 2003 und 2007 für die galaktischen HMXBs und LMXBs (Liu et al., 2006, 2007; Ritter and Kolb, 2003). Seitdem wurden neue Systeme entdeckt und Parameter von bekannten

Systemen haben sich geändert. Deshalb bestand das erste Projekt daraus neue Kataloge für HMXBs und LMXBs zu entwickeln wobei die Entwicklung des Katalogs für LMXBs von Dr. Avakyan übernommen worden ist. Die Entwicklung der Kataloge resultierte in zwei Veröffentlichungen (Neumann et al. (2023) und Avakyan et al. (2023)). Sowie einer Website die beide Kataloge beinhaltet und dem Benutzer die Möglichkeit gibt diese interaktiv zu erkunden.

Das zweite Projekt hingegen beschäftigt sich mit einer neuen und alternative Technik um unerwünschte Event des Hintergrunds bei Beobachtungen mit dem Röntgenobservatorium XMM-Newton zu entfernen. Die bereits etablierten Techniken haben ihre Vor- und Nachteile. So ist das Subtrahieren eines konstanten Hintergrunds zwar nicht rechenintensiv, jedoch kann es vorkommen das besonders im Bereich von wenigen Events die Anzahl der Quellen Events negativ wird, was unphysikalisch ist. Modellierung der Quelle und des Hintergrunds ist weiter Möglichkeit den Hintergrund in Beobachtungen zu berücksichtigen. Während diese Technik bessere Ergebnisse liefert als die Subtraktion eines konstanten Hintergrunds, ist sie jedoch rechenintensiver und setzt voraus das man weiß um was für eine Quelle es sich handelt, dies ist besonders bei neuen Quellen nicht unbedingt möglich. Deshalb verwendet die neue Technik einen probabilistischen Ansatz welcher verhindern soll das die Anzahl der Quellenevents negativ werden und gleichzeitig keinen Wissen über die Quelle voraussetzt. Da die probabilistische Technik eine Schätzung des Hintergrund benötigt wurden Bilder in verschiedenen Energiebereichen entwickelt die zur Schätzung verwendet werden können. Außerdem wurde die neuartige Technik zuerst an künstlich erzeugten Daten und später an echten Beobachtungen getestet um deren Nutzen zu evaluieren.

Contents

List of Figures

List of Tables

Acronyms

2MASS Two Micron All Sky Survey.

ADS Astrophysics Data System.

AGN Active Galactic Nuclei.

AMXPs accreting millisecond X-ray pulsars.

BHs black holes.

CAMEX CMOS Amplifier and MultiplEXer.

CCD Charge-Coupled Device.

CCOs Central Compact Objects.

CIF Calibration Index File.

CRSF cyclotron resonant scattering feature.

CSC Chandra Source Catalogue.

CVs cataclysmic variables.

CXB Cosmic X-ray Background.

CXO Chandra X-ray Observatory.

DEC declination.

EPIC European Photon Imaging Camera.

eROSITA extended ROentgen Survey with an Imaging Telescope Array.

ESA European Space Agency.

FOV Field of View.

GTI Good Time Interval.

HMXBs High Mass X-ray Binaries.

IBIS Imager on-Board the INTEGRAL Satellite.

IMXBs intermediate mass X-ray binaries.

INTEGRAL INTErnational Gamma-Ray Astrophysics Laboratory.

ISCO innermost stable circular orbit.

LMXBs Low Mass X-ray Binaries.

MOS Metal Oxide Semi-conductor.

NSs neutron stars.

ODF Observation Data File.

OM Optical/UV Monitor.

OoT Out-of-Time.

PDF probability density function.

RA right ascension.

RFC Focal Plane Camera.

RGA Reflection Grating Array.

RGS Reflection Grating Spectrometer.

RLO Roche-lobe overflow.

SAS SAS summary file.

SFR Star Formation Rate.

SFXTs Supergiant Fast X-ray Transients.

SGXBs Supergiant X-ray binaries.

SNR Signal-to-noise ratio.

SWCX Solar Wind Charge Exchange.

Swift/BAT Swift Burst Alert Telescope.

Swift/XRT Swift X-ray Telescope.

SXTs Soft X-ray transients.

SyXBs symbiotic X-ray binaries.

tMSRPs transitional millisecond radio pulsars.

UCXBs Ultracompact X-ray binaries.

VVV VISTA Variables in the Vía Láctea.

WDs white dwarfs.

WISE Wide-field Infrared Survey Explorer.

XMM-Newton X-ray Multi-Mirror Mission.

XMM-SAS XMM-Newton Science Analysis System.

XRBs X-ray binaries.

List of publication

Parts of this Thesis are based on the following publications (listed in reverse chronological order). The exact contribution of the author can be found in the acknowledgment of collaboration on the next pages as well as in Chapter 4, and Chapter 5 before the publications:

- "XRBcats: Galactic High Mass X-ray Binary Catalogue";
  Neumann M., Avakyan A., Doroshenko V., Santangelo A.; 2023; A&A, 677, A134
- "XRBcats: Galactic low-mass X-ray binary catalogue";
  Avakyan A., **Neumann M.**, Zainab A., Doroshenko V., Wilms J., Santangelo A.; 2023; A&A, 675, A199

Acknowledgment of Collaboration

XRBcats: Galactic High Mass X-ray Binary Catalogue (Neumann et al., 2023)

The main idea of creating an updated version of the galactic high mass X-ray binary catalogue came from Victor Doroshenko. I wrote most of the code for extracting information and creating finding charts. I did the literature work, together with Artur Avakyan, the overall majority of the literature research was conducted by me. X-ray binaries in question were discussed with Artur Avakyan. I led the writing of the paper with minor contribution of Artur Avakyan in the 'Problematic cases'-section. I created and maintained the website which contains the catalogue. I developed the code for the conversion of the catalogue into the necessary files for the website.

XRBcats: Galactic low-mass X-ray binary catalogue (Avakyan et al., 2023)

Victor Doroshenko had the main idea for this work. I provided Artur Avakyan with the already established code, which was used for the high mass X-ray binary catalogue, which he modified and used for the low mass X-ray binary catalogue. Additionally, I provided Artur Avakyan with the necessary code for the finding chart creation. I helped discuss ambiguous sources and did the literature work together with Artur Avakyan and Victor Doroshenko in his catalogue. I had a minor contribution in writing the paper. I created as well as maintained the website which contains the catalogue. I developed the necessary code to convert the files for their use on the website.

Part I

XRBcats: Galactic X-ray Binary Catalogues

1 Introduction

> *We are part of this universe we are in this universe but perhaps more important than both of those facts is that the universe is in us.*
>
> **— Dr. Peacock**
> (The Universe)

X-ray binaries provide a natural laboratory to study matter under extreme conditions as well as stellar evolution and accretion processes, etc. Nowadays, many X-ray binaries are known inside and outside our galaxy, and new ones are discovered frequently. In order to compile information concerning X-ray binaries in an efficient manner, catalogues are proven to be useful and an essential tool for astronomers to find suitable objects for their studies. Due to the daily new discoveries, an up-to date catalogue is even more important nowadays than it was in the past. Therefore, making it essential to create updated catalogues for HMXBs and LMXBs. The latest catalogues for galactic XRBs were published in the early 2000s (Ritter and Kolb, 2003; Liu et al., 2006, 2007). Many new sources have been discovered since then, and parameters of known systems have changed, hence an updated catalogue of galactic HMXBs and LMXBs is necessary.

This part of the thesis is structured as follows. Chapter 2 provides a short review of the components which make up XRBs. Chapter 3 summarizes the instrument catalogues which were used to create the HMXBs- and LMXBs-catalogue. Chapter 4 and Chapter 5 are the two publications which were published as a result of this undertaking. Because the website, which was developed in parallel to the publication, did not get enough explanation in the publications, Chapter 6 provides a more comprehensive overview of the website. As it is the goal to update the website frequently, Chapter 7 contains a user manual, which explains the steps to update the website in case of the HMXBs catalogue.

Astrophysical Background 2

2.1 Compact Object

X-ray binaries (XRBs) are systems consisting of a non-degenerated companion and a compact object. The compact objects in such systems can either be white dwarfs (WDs), neutron stars (NSs) or black holes (BHs). However, binary systems with a WDs are commonly considered as cataclysmic variables (CVs), a separate class from the XRBs. Nevertheless, all of those compact objects have some characteristics in common.

First, they do not burn any nuclear fuel and therefore do not possess any means to counteract the gravitational force through thermal pressure. However, the degenerated electron pressure counteracts gravity in case of WDs and the degenerated neutron pressure in case of NSs, only the BHs is a special case, which does not have any surface, because nothing is counteracting the gravitational force in a BHs.

Secondly, the compact objects are significantly smaller than a normal star, and therefore their surface gravity is many times higher. Additionally, due to conservation of magnetic flux, their magnetic fields are much stronger than normal stars.

As mentioned earlier, binary systems with WDs are not considered XRBs, therefore, the following parts are concentrating primarily on the physics of NSs and BHs.

Neutron Stars

Even before the discovery of neutrons by Chadwick in 1932, Landau was theorizing about stars heavier than $M_S > 1.5\,\mathrm{M}_\odot$. Apparently, in the evening on the day when Landau heard about the discovery of the neutron, he discussed with Rosenfeld and Bohr about cold and dense stars which are composed solely of neutrons (Shapiro and Teukolsky, 1983).

Two years later in 1934, Baader and Zwicky independently proposed the idea of neutron stars as high density stars with small radii, which are gravitationally bound much more than normal stars, and that those neutron stars are a product of

supernovae (Shapiro and Teukolsky, 1983). The first calculations of neutron stars models were done by Oppenheimer and Volkoff and Tolman in 1939. It took another 28 years before the first pulsar was discovered by Jocelyn Bell (Hewish et al., 1968) and Gold proposing that this pulsar could be a rotating NSs (Gold, 1968).

NSs are one of the possible endpoints of stellar evolution for massive stars between 10–$25\,\mathrm{M}_\odot$. When the proto-neutron star collapses under gravity, it reaches the density of $\rho \sim 10^{14}\,\mathrm{g\,cm^{-3}}$ so that electrons and protons are combined into neutrons. The ongoing collapse is counteracted by the pressure originating from these neutrons. This pressure arises due to Pauli's exclusion principle, which forbids the neutrons from occupying the same quantum state at the same time. While all neutron stars are rotating, not all show pulsations. Only NSs in which the emission region is misaligned with the rotational axis, pulsations are observable, similar to the light beam of a lighthouse. NSs have a typical radii of 10–$12\,\mathrm{km}$ with a mass of 1.2–$2.0\,\mathrm{M}_\odot$ (Özel and Freire, 2016). Due to the conservation of magnetic flux, the magnetic field strength must increase with decreasing radius ($B \sim R^{-2}$) therefore, neutron stars possesses quite strong magnetic fields of up to $10^{15}\,\mathrm{G}$ (see Figure 2.1).

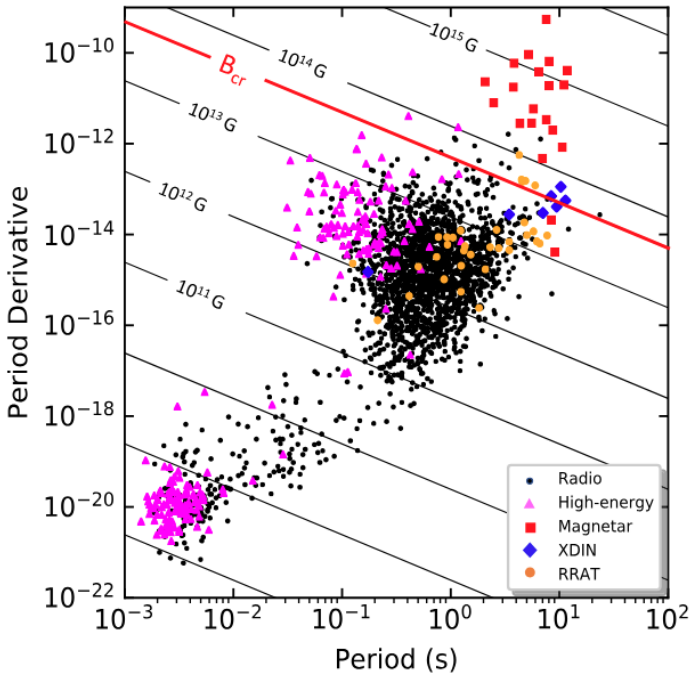

Figure 2.1. – Zoo of neutron stars in the period-period derivative diagramm, with solid line indicating their general magnetic field strength. Adopted from Harding (2023).

NSs can be found in a variety of different systems. Two examples of isolated NSs are Central Compact Objects (CCOs) in the center of a supernova remnant and radio pulsars.

In the case of Central Compact Objects only soft X-rays emissions are detected from the NSs surface which is cooling down after the supernova explosion. The spectrum is characterized by blackbody radiation with a temperature of $\mathrm{kT} \sim 0.2\text{–}0.5\,\mathrm{keV}$ (Pavlov et al., 2004).

Radio pulsars are fast-rotating NSs with stable and short pulsations ($P \gtrsim 30\,\mathrm{ms}$), the pulsations originate from the relativistic electrons being accelerated along the magnetic field lines of the neutron star.

Non-isolated NSs can be found in X-ray binaries. Similar to radio pulsars, these systems show pulsation, with a much longer period and in the X-rays instead of the radio band. Instead of synchrotron emission from the trapped electrons, the X-rays are released as comptonized thermal emission from the poles of the neutron star due to the infalling matter.

NSs in X-ray binaries can be extremely variable sources, depending on the amount of infalling matter. Their luminosity can change by more than five orders of magnitudes during outburst in comparison to quiescence times. This variable nature allows probing different aspects of their physics in quiescence and outburst.

Black Holes

NSs are not the only compact object that can be found in XRBs. BHs are the other compact objects, but in comparison to NSs, they do not possess any surface. Einstein's general theory of relativity predicted the existence of astrophysical objects that are so dense that not even light can escape its influence below a certain boundary the 'event horizon'. The 'event horizon' is located at the Schwarzschild radius $R_S = 2GM/c^2$ which only depends on the mass of the object. An object with a radius smaller than the R_S for its mass, is called a BHs; for the Sun the Schwarzschild radius would be 3 km. However, a particle could still orbit around a BHs in its last stable orbit called the innermost stable circular orbit (ISCO). For a non-rotating BHs it is located at $R_{ISCO} = 3R_S$.

Although light cannot escape from a black hole, it is still possible to observe it, through a hot accretion disk which is formed by the infalling matter, emitting thermal X-rays. The relativistic jets, observable from radio to infrared, also help to dissipate a significant amount of energy released through accretion. While neutron

stars can show pulsations or even X-ray bursts, black holes lack such pulsations or bursts, in addition to that, the luminosity in quiescence is much lower for BHs than for NSs.

While there are different classes of black holes depending on their mass, for example, stellar mass black holes ($2.5\,\mathrm{M}_\odot \lesssim M_{BH} \lesssim 50\,\mathrm{M}_\odot$), intermediate mass black holes ($50\,\mathrm{M}_\odot \lesssim M_{BH} \lesssim 10^5\,\mathrm{M}_\odot$) and supermassive black holes ($10^6\,\mathrm{M}_\odot \lesssim M_{BH} \lesssim 10^{10}\,\mathrm{M}_\odot$) (Camenzind, 2007), the important ones for XRBs are the stellar mass black holes. Such objects are created either directly from the evolution of a massive star or through accretion of matter onto a NSs, while the NSs exceeds the Tolman-Oppenheimer-Volkoff limit (Oppenheimer and Volkoff, 1939).

2.2 Accretion

Accretion (latin: ad crescere - to grow) in astrophysical context is the accumulation of matter or gas under the influence of gravity. While in high energy astrophysics it is typically discussed in the context of binary systems with compact objects, it is not exclusively limited to this case; most astronomical objects like stars and planets are formed by the means of accretion. Here, we focus on accretion in the high energy astrophysical context, which is the conversion of gravitational potential energy into radiation. Assuming that matter with a mass m is free-falling from infinity onto a compact object with mass M and radius R, we can write:

$$\frac{m v_{ff}^2}{2} = \frac{GMm}{r} \tag{2.1}$$

with v_{ff} the free-falling velocity of the matter and the gravitational constant G. When the matter reaches the surface of the compact object ($r = R$) like NSs or WDs, it gets abruptly decelerated and the kinetic energy is radiated away as heat. Assuming that the compact object is accreting matter with a rate $\dot{m}$, then the rate at which the kinetic energy is dissipated would be $\frac{1}{2}\dot{m}v_{ff}^2$ therefore, the luminosity of the compact object is given as:

$$L = \frac{1}{2}\dot{m}v_{ff}^2 = \frac{GM\dot{m}}{R}. \tag{2.2}$$

Since $L \propto M/R$ and NSs are one of the densest objects in the known universe, accretion is quite efficient in these objects. Using the Schwarzschild radius $R_s = 2GM/c^2$ for a star with mass M lets us rewrite Equation (2.2):

$$L = \frac{\dot{m}c^2}{2}\left(\frac{R_s}{R}\right) = \xi \dot{m} c^2, \tag{2.3}$$

with $\xi = \frac{R_s}{2R}$ the efficiency of conversion.
For a typical NSs($R = 10\,\mathrm{km}$ and $M = 1.0\,M_\odot$) the efficiency is $\xi \sim 0.15$ while the efficiency only reaches $\xi \sim 7 \times 10^{-3}$ in case of nuclear fusion from hydrogen to helium. Assuming that the free-fall velocity of the matter at the surface of the NSs is equal to its thermal velocity $v_{th} = \sqrt{k_B T/m}$ with $k_B = 1.38 \times 10^{-23}\,\mathrm{J\,K^{-1}}$, would result in a temperature on the surface of:

$$T = \frac{2GMm}{Rk_B}. \tag{2.4}$$

An electron with mass $m_e = 9.1 \times 10^{-31}\,\mathrm{kg}$ impacting on the surface of the neutron star would result in a temperature of $T \sim 10^9\,\mathrm{K}$ which corresponds to an energy of $E \sim 90\,\mathrm{keV}$ and emission in hard X-rays.

2.3 Matter transfer in binary systems

As seen in Equation (2.2), the luminosity also depends on the mass accretion rate $\dot{m}$. In most cases, the compact object is accreting matter from its companion. There are multiple ways how this matter can be transferred from the companion onto the compact object. LMXBs are in general accreting through Roche-lobe overflow (RLO). To understand the concept of Roche-lobe overflow it is necessary to understand the Roche lobe. The Roche lobe is one of the equipotential surfaces in a binary system, those surfaces are defined by:

$$\Phi = \frac{GM_1}{r_1} + \frac{GM_2}{r_2} - \Omega^2 r^2 = \text{constant}, \tag{2.5}$$

with r_1 and r_2 the distances to the point r from the centers of the stars with mass M_1 and M_2. The equipotential surface which encompasses both objects is called the Roche lobe (see Figure 2.2).

When a donor star in a binary system is fills its Roche lobe, matter is transferred through the inner Lagrangian point L_1, since it is seeking lower gravitational potential (see Figure 2.3). There are known HMXBs which are accreting through RLO,

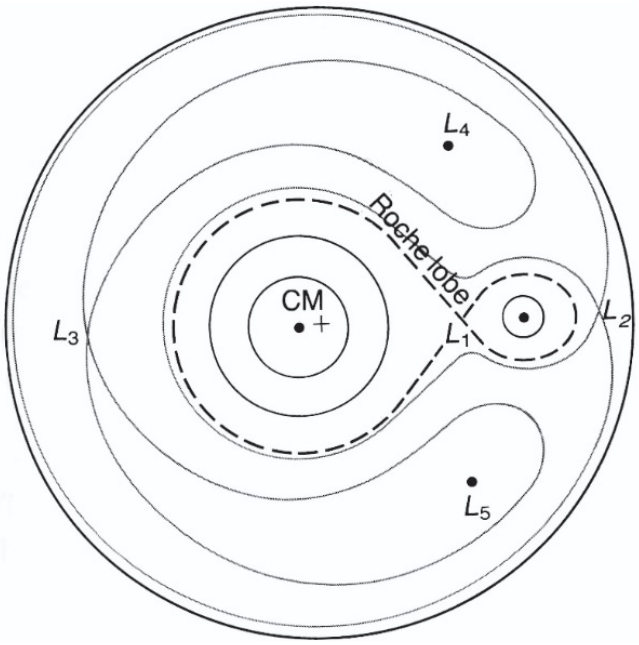

Figure 2.2. – Illustration of equipotential surfaces in a binary system. The dashed line indicates the Roche lobe which is the equipotential surface which connects both objects. L_1 is the inner Lagrangian point at which both lobes are touching each other. Adopted from (Longair, 2011).

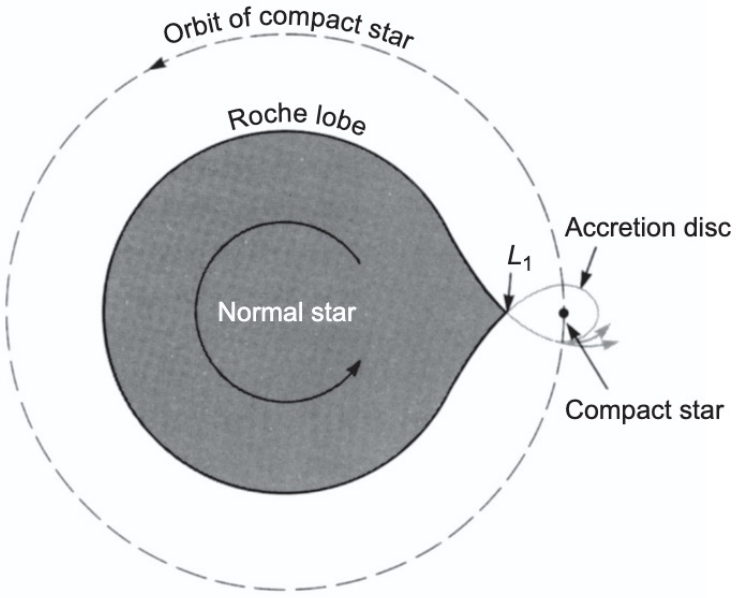

Figure 2.3. – Illustration of a system accreting through RLO. Cropped from Longair (2011).

however, since the mass loss rate is increasing with increasing mass of the donor star, Roche lobe overflow systems which accommodate such massive donor stars are short-lived ($\lesssim 100$ years for companions with $> 10\,\mathrm{M}_\odot$) (Savonije, 1978).

While RLO is the main accretion mechanism in LMXBs, most of the binary systems with supergiant companions are accreting directly from the stellar wind of the supergiant. In this case, the compact object is embedded in the outflow of the massive companion and accretion takes place in the cavity created by the bow shock (see Figure 2.4) (Shapiro and Teukolsky, 1983). Since the angular momentum of the matter in the wind is generally assumed to be low enough, it is assumed that most of the wind accreting systems are accreting spherically. However, if the angular momentum is high enough, the formation of an accretion disk is also possible. The typical mass loss rates in such systems are of the order of $\dot{\mathrm{M}} \sim 10^{-6}\,\mathrm{M}_\odot\,\mathrm{yr}^{-1}$ (Kudritzki and Puls, 2000).

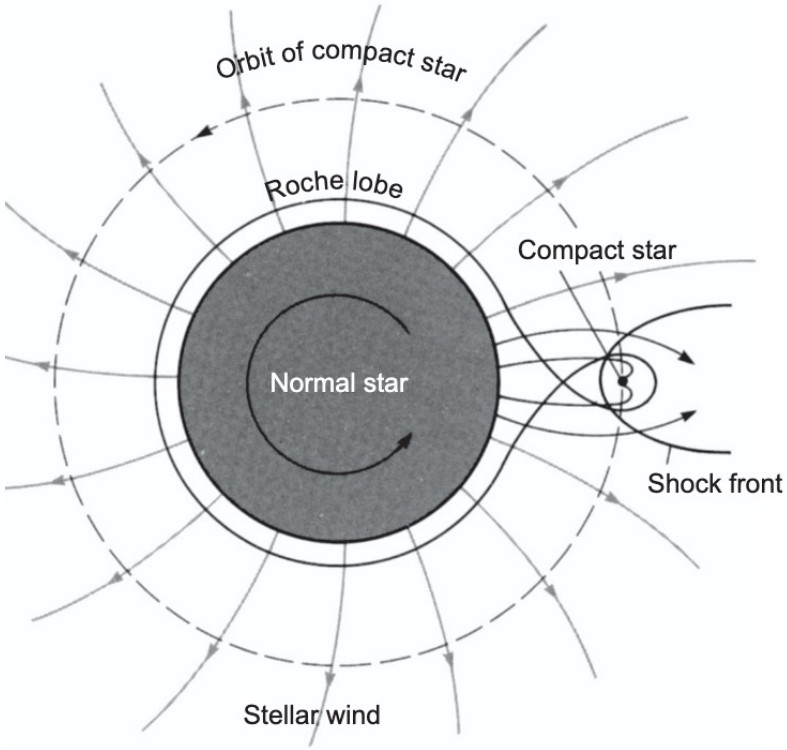

Figure 2.4. – Illustration of a windaccreting system. Cropped from Longair (2011).

There is an additional mechanism that is in between Roche-lobe overflow and wind accretion. This is the case when some parts of the donor stars atmosphere is expanding over the Roche lobe, thus it is called the atmospheric Roche-lobe overflow.

As with the normal RLO, the matter is focussed through the L_1 point onto the compact object. However, this type of accretion is not a run-away process unlike the fully developed RLO, and can sustain mass loss rates between $\dot{M} \sim 10^{-10}\,\mathrm{M}_\odot\,\mathrm{yr}^{-1}$ and $\dot{M} \sim 10^{-7.5}\,\mathrm{M}_\odot\,\mathrm{yr}^{-1}$ for thousands of years, as shown by Savonije (1979).

The last kind of accretion occurs in Be/X-ray binaries. These are systems containing a rapidly rotating O- or B-star with a circumstellar 'decreation' disk in the equatorial region, which is formed by ejected material from the star (Chaty, 2022). As the stellar wind in the equatorial region is both denser and slower in comparison to the fast and less dense stellar wind in the polar region, this results in the creation of the equatorial outflowing disk (Lamers and Cassinelli, 1999). The compact object in most of the Be/X-ray binaries has a high eccentric orbit, it also has two states of accretion. While far away, the compact object accretes spherically through the stellar wind. However, close to the periastron passage, it closely passes the 'decreation' disk or even penetrates it, which leads to a drastic increase in the accretion rate and the creation of an accretion disk around the compact object (Orellana and Romero, 2005). An illustration of a Be/X-ray binary can be seen in Figure 2.5.

Be/X-ray binaries show two different outbursts, type I outbursts occur periodically occurring close to the periastron passage of the NSs and last for a fraction of the orbit. During Type I outbursts, a moderate increase of the X-ray luminosity ($L_X \lesssim 10^{37}\,\mathrm{erg\,s}^{-1}$) can be observed (Kretschmar et al., 2019). In Type II outbursts, however, the luminosity is significantly increased ($L_X \gtrsim 10^{37}\,\mathrm{erg\,s}^{-1}$) (Okazaki and Negueruela, 2001). The Type II outbursts do not show any orbital preferences and can last for weeks or even months (Okazaki and Negueruela, 2001). While the exact mechanism behind the Type II outbursts are not fully understood yet, one of the possible explanations is, that the 'decretion disk' becomes warped and eccentric so that the NSs can accrete a large amount of matter (Martin et al., 2014).

2.4 X-ray Binaries

Broadly, there are two main types of X-ray binaries, classified by the mass of the optical companion. If the mass of the companion is below $M_{opt} \lesssim 1\,\mathrm{M}_\odot$ (Chaty, 2022) those system are classified as LMXBs, above $M_{opt} \gtrsim 8\,\mathrm{M}_\odot$ (Chaty, 2022) they are classified as HMXBs. In principle, there is a third type that populates the mass gap between LMXBs and HMXBs which are the intermediate mass X-ray binaries (IMXBs) (Pfahl et al., 2003), a prominent source of this class is Hercules

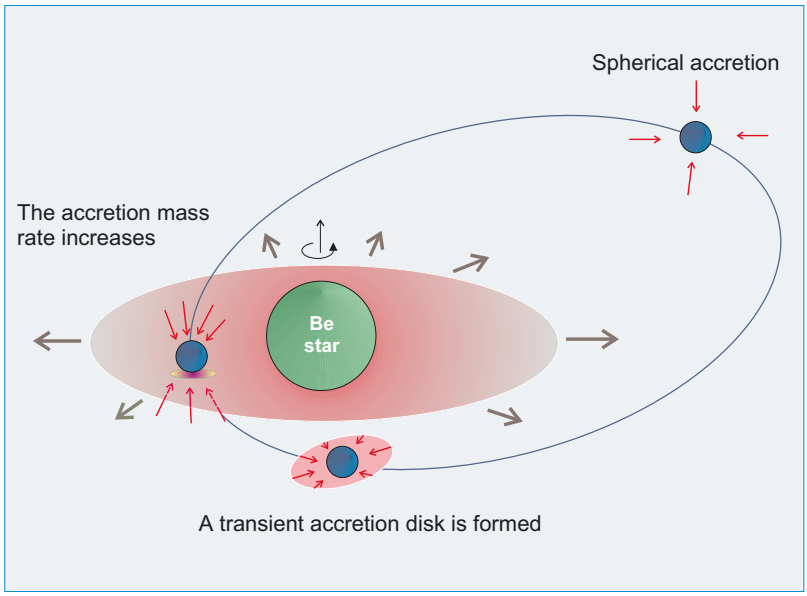

Figure 2.5. – Illustration of a Be/X-ray binary system. A NSs is orbiting a Be Star in an eccentric orbit, passing through the decretion disk close to periastron passage. Cropped from Orellana and Romero (2005).

X-1 (Tananbaum et al., 1972), however, in comparison to the population of LMXBs and HMXBs, the IMXBs population consists of only a few systems.

All X-ray binaries have one thing in common, and this is the compact object that accretes from a donor star. The compact object can be a NSs or BHs. While there are binary systems with WDs, these systems are considered separately as CVs as mentioned in Section 2.1.

Since HMXBs have higher mass accretion rates than LMXBs, they tend to have shorter lifetimes $\sim 10^7\,\mathrm{yr}$ in comparison to $\sim 10^{10}\,\mathrm{yr}$ for LMXBs. Due to their shorter lifespan, they are considered good tracers for regions with high Star Formation Rate (SFR) (Avedisova, 2002; Grimm et al., 2003). While the LMXBs population of a galaxy can help in estimating its mass (Gilfanov, 2004). HMXBs in our galaxy are typically found in the galactic plane, while LMXBs can be also found in the galactic halo, as seen in Figure 2.6.

High Mass X-ray Binaries

Although, XRBs with an massive donor star of $> 8\,\mathrm{M}_\odot$ belong to the class of HMXBs, this classification can be further refined by distinguishing the system according to the properties of the companion and the accretion mechanism. The Supergiant X-ray binaries (SGXBs) are in general persistent HMXBs that accrete via the stellar wind

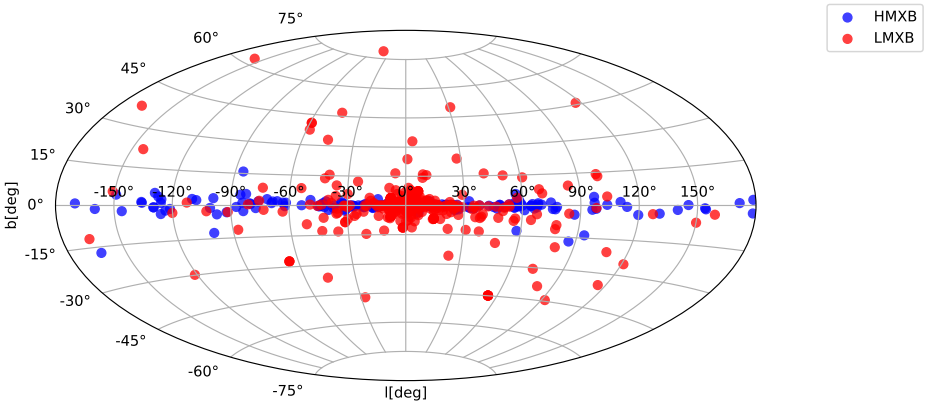

Figure 2.6. – Galactic XRBs population created from the newest version of the XRBcats catalogues (`http://astro.uni-tuebingen.de/~xrbcat/`).

(Kretschmar et al., 2019). A special type of SGXBs was detected by the INTErnational Gamma-Ray Astrophysics Laboratory (INTEGRAL). They exhibit short outbursts (few hours) with bright flares (10^{36}–$10^{37}\,\mathrm{erg\,s^{-1}}$), because of their transient nature those systems are referred to as Supergiant Fast X-ray Transients (SFXTs) (Negueruela et al., 2006). As mentioned earlier, HMXBs can also accrete via Roche-lobe overflow, one of the most prominent binaries is Cen X-3 (Tjemkes et al., 1986), however, in the case of a fully-developed Roche-lobe overflow this would result in a mass accretion rate of about $10^{-3}\,\mathrm{M_\odot\,yr^{-1}}$ which would obscure the X-ray source (Kretschmar et al., 2019). The last sub-class of HMXBs are the Be/X-ray binaries which makes up the greatest part of the known HMXBs population. As mentioned in Section 2.3 these system contain a fast-rotating O- or B-star with a decreation disk in the equatorial region, and a compact object on an eccentric orbit which closely passes by the decreation disk or penetrates it.

Low Mass X-ray Binaries

LMXBs host a late-type main-sequence star (M-K) and a compact object. While HMXBs with BHs are uncommon (six galactic HMXBs, Neumann et al. 2023) it is more common for LMXBs (~ 70 galactic LMXBs, Avakyan et al. 2023). However, NSs-LMXBs are, by a factor of ~ 2 more numerous than BHs- LMXBs (Bahramian and Degenaar, 2023). Around 20% of the NSs-LMXBs are either accreting millisecond X-ray pulsars (AMXPs) or transitional millisecond radio pulsars (tMSRPs) (Bahramian and Degenaar, 2023). In those systems, parts of the accretion disk is funneled by the magnetic field onto the poles of the NSs, which increases the temperature on the surface, giving rise to X-ray pulsations. AMXPs getting their name from the fact

that they show fast X-ray pulsation in the range of $\sim$ 1–10 ms (Campana and Di Salvo, 2018). Ultracompact X-ray binaries (UCXBs) are a subclass of LMXBs, they are characterized by their short orbital period $\lesssim 80\,\mathrm{min}$ (Bahramian and Degenaar, 2023). To accrete in systems with such a short orbital period, the donor star needs to be a white dwarf or a helium burning subdwarf, otherwise these orbital periods cannot be reached and still fill the Roche lobe (Paczynski and Sienkiewicz, 1981; Rappaport et al., 1982; Savonije et al., 1986). So far the above mentioned subclasses accrete through RLO, however, there are LMXBs which accrete through wind accretion. Such LMXBs are called symbiotic X-ray binaries (SyXBs), and they consist of a BHs or NSs and a low-mass late-type giant (Bahramian and Degenaar, 2023). LMXBs containing BHs are usually transient systems and are called Soft X-ray transients (SXTs), (Chaty, 2022). They can remain undetected for months or decades with luminosities below $10^{32}\,\mathrm{erg\,s^{-1}}$ (Chaty, 2022). During their active phase, they can reach X-ray luminosities of $\sim 10^{38}\,\mathrm{erg\,s^{-1}}$, while their optical activity increases by up to 10 magnitudes, this active phase can last for weeks or months (Chaty, 2022).

Galactic XRBs population

The galactic population of XRBs consists of 169 HMXBs (Neumann et al., 2023) and 349 LMXBs (Avakyan et al., 2023) as of 2023, however, new XRBs candidates are discovered regularly (for example 1eRASS J061330.8+160440 and 1eRASS J161201.9-464622 (Avakyan et al., 2025)) with the help of new instruments like the extended ROentgen Survey with an Imaging Telescope Array (eROSITA) (Predehl et al., 2021). With over 200 systems the majority of the galactic LMXBs population are considered X-ray transients, followed by around 120 systems which show behaviors of X-ray Burster and around 100 sources in which the compact source is a radio pulsar (Avakyan et al., 2023). As for HMXBs the majority of the sources are Be/X-ray binaries (72) while 42 systems have an identified supergiant companion (Neumann et al., 2023). The number of NSs-XRBs exceed the number of BHs-XRBs significantly. Out of the 349 LMXBs there are around ~ 75 systems that contain a BHs-candidate and out of the 169 HMXBs only 6 systems have a BHs-candidate. Meanwhile, the remaining XRBs-population consists of NSs-XRBs.

3 Instrument Catalogues

To facilitate the creation of the LMXBs- and HMXBs-catalogues, we used infrared, optical, and X-ray catalogues for positions and flux estimations across multi energy bands. Table 3.1 shows an overview of the used catalogues while the following chapter explains the catalogues in a bit more detail.

Catalogue	Reference
Near Infrared	
2MASS	Skrutskie et al. (2006)
CatWISE	Marocco et al. (2021)
Optical	
Gaia	Gaia Collaboration et al. (2023)
StarHorse	Anders et al. (2022)
Bailer-Jones	Bailer-Jones et al. (2021)
Soft X-ray	
XMM-Newton	Webb et al. (2023)
Chandra	Evans et al. (2024)
Swift/XRT	Evans et al. (2020)
Hard X-ray	
INTEGRAL	Krivonos et al. (2012)
Swift/BAT	Oh et al. (2018)

Table 3.1. – Instrument catalogues which were used to create the XRBcats catalogues.

3.1 Near Infrared

2MASS

In the near-infrared the Two Micron All Sky Survey (2MASS) provides positional accuracy of around $0.5\,\mathrm{arcsec}$ (Skrutskie et al., 2006). The data which was taken between June 1997 and February 2001 covers almost the entire sky (99.998%, Skrutskie et al. 2006). With its high positional accuracy, it was used as an alternative for sources without a Gaia position. In addition to the source location, the 2MASS-catalogue was used to extract information in the J- ($1.25\,\mu\mathrm{m}$), H- ($1.65\,\mu\mathrm{m}$) and K-band ($1.65\,\mu\mathrm{m}$).

CatWISE

In the Near Infrared, CatWISE (Marocco et al., 2021) was used in addition to the catalogue of 2MASS. CatWISE used data from the WISE and NEOWISE survey in the $3.4\,\mu\mathrm{m}$ and $4.6\,\mu\mathrm{m}$ band. It covers the entire sky and contains information about 1.9 billion sources which were observed between January 2010 and December 2018. The only piece of information that was extracted from the CatWISE-catalogue is the magnitudes in the W1-band ($3.35\,\mu\mathrm{m}$) and the W2-band ($4.6\,\mu\mathrm{m}$) and their corresponding uncertainties.

3.2 Optical

Gaia

The catalogue with the highest positional accuracy comes from the Gaia mission (Gaia Collaboration et al., 2016), especially the third data release (Gaia Collaboration et al., 2023) (Gaia-DR3). Gaia-DR3 contains observation from the first 34 months of the mission, which resulted in optical data from over 1.8 billion objects. With its $\mu - \mathrm{arcsec}$ accuracy, Gaia-DR3 was the main source for accurate object positions. In addition to that, it provided a large variety of photometric and astrometric data. Other catalogues utilize the Gaia data, which are described in the following parts.

StarHorse

StarHorse (Anders et al., 2022) is one of the catalogues that used the data from the Gaia satellite. It provides information on the parameters like stellar mass and distance. To infer those parameters StarHorse uses other photometric catalogues besides Gaia, that includes the catalogues of Pan-STARRS, SkyMapper, 2MASS and AllWISE. In their code, they compare the spectroscopically measured parameters (like effective temperature T_{eff} and surface gravity $log\ g$), parallax and photometric magnitudes, with predictions from stellar evolutionary models (Queiroz et al., 2018). Anders et al. (2022) provide these parameters for around 360 million objects. For the stellar effective temperature as well as for the distance estimation, StarHorse was one of the prime sources of information.

Bailer-Jones

Similar to StarHorse, Bailer-Jones (Bailer-Jones et al., 2021) also provides information on the distance of a source. To estimate the distance, they use Bayesian inference. Instead of using the stellar evolutionary models, they developed a direction dependent prior which is constructed from a three-dimensional model of our galaxy. From this catalogue, distance estimations (both, geometric and photogeometric) are used, as well as their uncertainties on the estimation. Bailer-Jones et al. (2021) provides the geometric distances for 1.47 billion sources and the photogeometric distance estimation for 1.35 billion sources.

3.3 Soft X-rays

Chandra

Information from the Chandra X-ray Observatory (CXO) is retrieved from the second release of the Chandra Source Catalogue (CSC) (Evans et al., 2024). It was released in 2019 and contains information of ~ 300000 distinct X-ray sources from observations publicly available before the end of 2014 (Evans et al., 2024). The observations that are used to create the CSC 2.0 cover $\sim 517\,\mathrm{deg}^2$ (Evans et al., 2024) of the sky. In addition to the source position, the CSC 2.0 contains a large quantity of source-specific parameters, for example, the hardness ratio or temporal variability (Evans et al., 2024). The most important values for the XRBcats are the source position, positional uncertainty, and the source flux.

XMM-Newton

To make use of the XMM-Newton observations this catalogue also made use of the fourth XMM-Newton Serendipitous Source Catalog in its thirteenth data release (4XMM-DR13). The 4XMM-DR13 catalogue provides information of about ~ 660000 objects (Webb et al., 2023). The general content is described in Webb et al. (2020). This catalogue used a total of 13243 observations which were done between February 2000 and December 2022 with a total sky coverage of $\sim 1328\,\mathrm{deg}^2$ (3.2%). Similar to the CSC, the 4XMM-DR13 catalogue provides the flux estimation of different instruments in different energy bands to cover the full energy-range of the instruments. Like in the case of CSC the important parameters extracted from 4XMM-DR3

were the source locations together with their uncertainties as well as the source flux in the energy range of 0.2–12keV.

Swift/XRT

The Second Swift XRT Point Source Catalogue (2SXPS, Evans et al. 2020) is the last of the three soft X-ray catalogues. The 127519 observations which were taken between January 2005 and August 2018 revealed a grand total of 206335 unique X-ray sources. With a sky coverage of $\sim 3800\,\mathrm{deg}^2$ (9.2%), the 2SXPS-catalogue has the highest coverage of all three soft X-ray catalogues. In addition to the source location and its uncertainty, the 2SXPS-catalogue also includes a variety of flux estimations using different spectral models. One of the stand-out features of the 2SXPS-catalogue in comparison to the other two soft X-ray catalogues is the inclusion of the hydrogen column density for individual sources.

3.4 Hard X-rays

INTEGRAL

For INTEGRAL the nine-year galactic hard X-ray survey from INTEGRAL/IBIS (Krivonos et al., 2012) was used. It contains flux-information of about 402 sources which are lying in a galactic latitude of $|b| < 17.5°$, of which 82 are HMXBs and 108 are LMXBs (Krivonos et al., 2012). The information was extracted from publicly available INTEGRAL data, which was obtained between December 2002 and January 2011 (Krivonos et al., 2012). For XRBcats the flux in the 17–$60\,\mathrm{keV}$ was used.

Swift/BAT

The second instrument which was used in the hard X-rays was the Swift Burst Alert Telescope (Swift/BAT) instrument. The 105-Month *Swift*-BAT All-sky Hard X-ray Survey catalogue (Oh et al., 2018) was used to create XRBcats. It uses data from observation which were done between December 2004 and August 2013. The catalogue contains a total of 1632 sources, of which 108 are HMXBs and 109 are LMXBs (Oh et al., 2018), where the particular interest was the flux in the 14–$195\,\mathrm{keV}$ energy band.

4 XRBcats - High Mass X-ray Binaries

As described in Section 2.4, XRBs can be in general seperated into two distinct classes, HMXBs ($M_{opt} \gtrsim 8\,\mathrm{M}_{\odot}$) and LMXBs ($M_{opt} \lesssim 1\,\mathrm{M}_{\odot}$). The following paper, describes the work which was undertaken to create an up-to-date catalogue of HMXBs in our galaxy. The main inspiration of this work comes from Liu et al. (2006), which was the most up-to-date catalogue of galactic HMXBs when the work on this paper began. I developed the code for finding new HMXBs as well as updating information on already identified HMXBs. In addition to extracting data, finding charts in different wavelengths were created. I contributed the majority of the code for the creation of the finding charts. While the idea of a website for the catalogue was developed together with all the coauthors. I led the development of the website and was in charge of updating, and maintaining it.

Astronomy & Astrophysics manuscript no. HMXBcat
September 25, 2023

XRBcats: Galactic High Mass X-ray Binary Catalogue ⋆ ⋆⋆

M. Neumann ⋆⋆⋆, A. Avakyan, V. Doroshenko and A. Santangelo

Universität Tübingen, Institut für Astronomie und Astrophysik Tübingen, Sand 1, Tübingen, Germany

Received 19 December 2022; accepted Accepted 3 July 2023

ABSTRACT

Context. We present a new catalogue of high mass X-ray binaries (HMXBs) in the Galaxy that we call the Galactic High Mass X-ray Binary Catalogue (XRBcats), which improves upon the most recent of such catalogues. We include new HMXBs discovered since previous publications and revise the classification for several objects previously considered HMXBs or HMXB candidates. The catalogue includes basic information (e.g. source names, coordinates, types), other data (e.g. distance and X-ray flux estimates, binary system parameters), and other characteristic properties of the 169 HMXBs catalogued. We also present finding charts in several bands from the infrared to hard X-rays for each object.

Aims. The aim of this catalogue is to provide a list of all currently known Galactic HMXBs, including basic information on both compact objects and non-degenerate counterpart properties (where available). We also include objects tentatively classified as HXMBs in the literature and give a brief motivation for the classification in each case.

Methods. The catalogue is compiled based on a search of known HMXBs and candidates in all publicly available databases and literature published before May 2023. The relevant properties in various wavelength bands were collected for all objects, either from the literature or using data provided by large-scale surveys. For the latter case, the counterparts in each individual survey were found by cross-correlating positions of identified HMXBs with relevant databases.

Results. An up-to-date catalogue of Galactic HMXBs is presented to facilitate research in this field. Our goal was to collect a larger set of relevant HMXB properties in a more uniform way compared to previously published works.

Key words. catalogues – binaries: close – stars: early-type – X-rays: binaries

1. Introduction

X-ray binaries (XRBs) are still the focus of observational X-ray astronomy almost 60 years after their discovery. These systems consist of a compact object, which can be a neutron star (NS), a black hole (BH), or a white dwarf (WD), and a non-degenerate companion providing matter for the accretion powering the X-ray emission. Depending on the mass of the optical companion, XRBs can subdivided into two categories. Systems with low mass optical companions ($M_{\rm opt}$) $\lesssim 1 M_\odot$ are classified as low mass X-ray binaries (LMXBs Chaty 2022), whereas those with higher mass optical companions ($M_{\rm opt} \gtrsim 8 M_\odot$) are classified as high mass X-ray binaries (HMXBs, Chaty 2022). In the cases where the compact object is either a NS or a BH, accretion is usually assumed. However, systems in which the compact object is a WD are commonly considered separately from the first two cases, and are most often referred to as cataclysmic variables (CVs) rather than XRBs due to both physical and historical reasons. The mass gap between LMXBs and HMXBs is populated by a handful of sources (e.g. Her X-1 with an optical companion with a mass of $M_{\rm opt} \sim 2 M_\odot$ (Tananbaum et al. 1972), often referred to as intermediate-mass X-ray binaries (IMXBs, Pfahl et al. 2003). Despite the mass of the optical companion, all of these binaries host a compact object, and thus represent endpoints of stellar evolution. Understanding the properties of this population is key to understanding the evolution of the Galaxy as a whole. Due to their short characteristic lifetimes of $\sim 2 \times 10^7$years, HMXBs can be considered young systems when compared to LMXBs ($\sim 10^{10}$years), and are thus good tracers for star forming activity (Grimm et al. 2003). Within the Milky Way such systems are concentrated around the Galactic plane and are often localised within the spiral arms. Similarly to other astrophysical sources, there are still large uncertainties in the spatial distributions, luminosity distributions, numbers, physics, and evolutionary cycles for XRBs. This issue is exaggerated by the fact that we only observe a fraction of the overall population of these systems. However, the number of known objects is ever increasing. It is therefore essential to keep the census of known XRBs and their properties up to date, especially in the era of new large-scale surveys such as eRosita and *Gaia* that provide a wealth of new observational information across the entire sky. The goal of this paper is therefore to provide such an update for HMXBs. In parallel, similar efforts for LMXBs and IMXBs have been undertaken independently (Avakyan et al. 2023).

As already mentioned, HMXBs constitute a relatively broad class of objects defined based on the mass of the companion star. Depending on the properties of the companion, and the accretion mechanism, they can be divided into several sub-classes. Systems accreting via stellar winds of their optical companion with mass-loss rates of up to $\dot{M} \sim 10^{-6..-5} \mathrm{M}_\odot\ \mathrm{yr}^{-1}$ (Kudritzki & Puls 2000) are usually persistent sources of X-rays and are referred to as supergiant X-ray binaries (SGXBs, Corbet 1986). Within the category of SGXBs are also the highly variable supergiant fast X-ray transients (SFXTs, Negueruela et al. 2006), which are non-accreting most of the time, but show occasional bright flares on timescales of minutes to days with peak fluxes comparable

⋆ The catalogue is available at CDS via anonymous ftp to cdsarc.u-strasbg.fr (130.79.128.5) or via `http://cdsarc.u-strasbg.fr/viz-bin/cat/J/A+A/677/A134`

⋆⋆ A web version is publicly accessible at `http://astro.uni-tuebingen.de/~xrbcat/`

⋆⋆⋆ E-mail: marvin.neumann@astro.uni-tuebingen.de

to other SGXBs. Depending on the mass ratio, accretion can be quasi-symmetric, or focused by gravity via the L1 point, as is the case of Vela X-1 (Kretschmar et al. 2021). In some cases Roche-lobe overflow (RLO) can also occur; the Galactic micro-quasar SS 433 and the first X-ray pulsar ever discovered, Cen X-3, are examples where this mechanism dominates. With mass-loss rates of $\dot{M} \sim 10^{-3} M_\odot\ yr^{-1}$ (for a fully developed RLO) these systems have rather short lifetimes (of the order of the thermal timescale of the optical companion), and are thus rare. However, Savonije (1978) showed that an atmospheric RLO is feasible and could be sustained for thousands of years with mass-loss rates below $\dot{M} \sim 10^{-8} M_\odot\ yr^{-1}$, and indeed more HMXBs of this type are known to exist outside of our own Galaxy. However, the known HMXB population is dominated by Be X-ray binaries (BeXBs, Reig 2011). In these systems the optical companion is either an early-type B star (earlier than B3) or a late-type O star (later than O8), with an equatorial decretion disc. This disc is formed by the material released at the equator of the optical companion due to its high rotation velocity (Balona & Ozuyar 2020). Decretion disc size is known to be variable and can be traced by the characteristic emission lines in the optical spectra of Be star. Passage of the compact object (in the vast majority of cases a NS) through the disc leads to enhanced accretion, especially if the disc is in an expanding state. From an observational point of view, this leads to the appearance of two different kinds of outbursts that are characteristic of BeXB systems. Type I outbursts are periodically occurring events with a typical peak luminosity below $10^{37} erg\ s^{-1}$, normally coinciding with the periastron passage of the compact object. Type II outbursts are more irregular, less frequent events, and are apparently associated with the expansion of the circumbinary disc. Peak luminosity can reach up to $10^{39} erg\ s^{-1}$ (Doroshenko et al. 2020), thereby exceeding the Eddington luminosity of the neutron star. Outbursts of this type are usually referred to as giant outbursts and do not show any preferred orbital phase, and usually last longer than their type I counterparts. Importantly, all BeXBs are transients with relatively low duty cycles and are mostly observable only during their outbursts. They continue, therefore, to be discovered at a steady rate, and contribute to the increase in the number of known HMXBs.

Prior to the recent catalogue Fortin et al. (2023), the most commonly used catalogue of HMXBs, and the starting point of this work, was Liu et al. (2006), which was published ∼16 years ago. Since then many new HXMBs have been discovered, and some previously categorised objects have lost their HMXB status. What is perhaps even more important, is that a wealth of additional observational data were collected with new facilities such as the X-ray Multi-Mirror Mission (*XMM-Newton*) (Jansen et al. 2001), the International Gamma-Ray Astrophysics Laboratory (*INTEGRAL*) (Winkler et al. 2003) or *Gaia* (Gaia Collaboration et al. 2016), to name but a few. In this work we present an updated catalogue of Galactic HMXBs including multi-wavelength information as well as the new sources discovered since the publication by Liu et al. (2006). The current catalogue only includes Galactic HMXBs and does not include objects from the Small or Large Magellanic Clouds; candidates within these regions often have poorly identified or characterised optical counterparts. For Galactic HMXBs, a concerted effort has been made within the field to collect all relevant and current multi-wavelength information including distances, optical magnitudes, variability information in soft and hard X-rays, and information on detection in radio band, amongst others. Such information ensures that the catalogue can aid in the identification of new HMXBs in the ongoing and future X-ray surveys, population studies, and other investigations.

2. Definition of the sample and data sources

As a first step, we compiled a sample of 169 HMXBs (123 confirmed and 46 candidates) by searching the *SIMBAD*[1] and *VizieR*[2] archives hosted by the Centre de Données astronomiques de Strasbourg (CDS) databases and the literature. The largest fraction of this sample (105 objects) originates from Liu et al. (2006), the catalogue this work is based on. We also systematically searched the literature (including Astronomoner's Telegrams[3]) for reports of new HMXB discoveries. A large fraction of new HMXBs reported in the literature were discovered between 2006 and 2020 by both the *INTEGRAL* mission and the Neil Gehrels Swift Observatory (*Swift*) (Gehrels et al. 2004) (29 objects), as summarised in Kretschmar et al. (2019), which can therefore also be considered one of the main sources used in this work. As the next step, we considered all objects classified as HXMB or candidates in the *SIMBAD* and *VizieR* databases. Considering that the majority of objects not present in these databases or the literature are extragalactic, and the fact that HMXBs are strongly clustered towards the Galactic plane Grimm et al. (2002), we restricted our search to the Galactic latitude between ±15° in the latter case. As an aside, the recent HXMB catalogue Fortin et al. (2023) was published during the review process of this paper. We therefore utilised this catalogue as an additional source list, and cross-checked our own catalogue against this, which resulted in an additional five HMXBs. We note that although considerable effort was put into finding all possible HXMBs and candidates, it is still possible that some sources have been omitted, we therefore urge the reader to report such omissions to the corresponding author. We also note that some of the objects considered by Liu et al. (2006) as HMXBs or candidates are no longer accepted as such. In Section 3.2 we discuss these cases separately.

2.1. HMXB sample and classification

To reflect the variety among the properties of HMXBs, we include information on the origin of the donor star or compact object, system variability, and other relevant properties. These properties are then used to define a set of flags designed to represent the range of properties present in this catalogue. In general, the criteria for these flags are based on the classifications introduced in Liu et al. (2006). However, we have supplemented them with additional flags based on the information provided within Kretschmar et al. (2019), Staubert et al. (2019), and van den Eijnden et al. (2021, 2022). As a result, we converged on the set of flags listed below. The frequency of individual flags is provided in brackets and is also presented graphically in Fig. 1 to give a broad overview of the sample of known HMXBs. We note that the flags below are not meant as a basis for classification of HXMBs, but rather illustrate the range of different systems within the population considered in this catalogue, meaning a system may have multiple flags:

1. BH: black hole candidate (6);
2. EB: eclipsing or partially eclipsing binary system (9);
3. MQ: micro-quasar (4);
4. RS: radio emitting HMXB(13);

[1] http://simbad.u-strasbg.fr/simbad/
[2] https://vizier.cds.unistra.fr/viz-bin/VizieR
[3] https://astronomerstelegram.org/

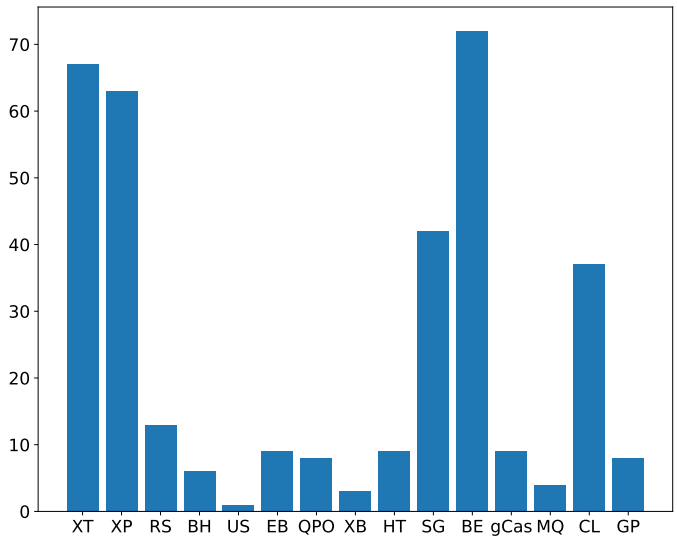

Fig. 1. HMXBs population of each type in the Galaxy.

5. XB: X-ray burst source (3);
6. XP: X-ray pulsar (63);
7. XT: transient X-ray source (67);
8. US: ultra-soft X-ray spectrum (1);
9. HT: hard transient (9);
10. Gcas: Gamma Cassiopeiae-like source (9);
11. QPO: quasi-periodic oscillation (8);
12. SG: supergiant optical companion (42);
13. BE: Be star companion (72);
14. CL: cyclotron resonance scattering feature in X-ray spectrum (37);
15. GP: high mass gamma-ray binary (8).

2.2. X-ray properties

Considering that the prime feature of XRBs is their X-ray emission, we attempted to compile the relevant X-ray properties of the HMXBs in the catalogue. This includes fluxes in the soft X-ray band as observed by *XMM-Newton*, the Chandra X-Ray Observatory (*Chandra*; Weisskopf et al. 2000), and the Swift X-Ray Telescope (*Swift*/XRT; Burrows et al. 2005), and in the hard X-ray bands as observed by *INTEGRAL* and the Swift Burst Alert Telescope (*Swift*/BAT; Barthelmy et al. 2005). We also compiled X-ray positions, in order to assess the reliability of optical counterpart identification or identify plausible counterparts, as described below. In the case of *XMM-Newton* we report flux in the 0.2-12 keV energy band (corresponding to EPIC_8 band in the *XMM-Newton* catalogues[4] Webb et al. 2020). For *Chandra*[5] (Evans et al. 2010) we preferentially used the broad ACIS band (0.5 – 7.0 keV) or the wide HRC band (0.1 – 10.0keV) depending on the availability. In the case of *Swift*/XRT we used data that is available in the Swift X-ray telescope point source catalogue[6] (2SXPS) (Evans et al. 2020), where for the flux we utilised the energy range 0.3 – 10.0keV, calculated from an assumed power-law spectrum (Evans et al. 2020). In the hard X-ray regime we used an energy range of 14 – 145 keV for *Swift*/BAT[7] (Oh et al. 2018) data and an energy range of 17 – 60 keV for *INTEGRAL* data[8] (Krivonos et al. 2012).

2.3. Optical position and astrometry

Most of the HMXBs in the sample have identified optical counterparts (an almost essential pre-requisite for HXMB classification). However, the optical positions reported in Liu et al. (2006) are often limited by the techniques of the time, and thus show discrepancies with modern observations. An effort was made to update these data with the updated astrometry provided by the *Gaia* mission. To achieve this, we first confirmed whether the *SIMBAD* database already contained identified *Gaia* DR3[9] (Gaia Collaboration et al. 2023) or Two Micron All Sky Survey[10] (2MASS; Cutri et al. 2003) counterparts. If this was not the case, we matched the literature positions, which included V-band magnitudes, to *Gaia* DR3 using a large search radius of 10″. *Gaia* counterparts that matched the literature positions and magnitudes within the uncertainties were then selected. In most cases this corresponded to an object closest to the literature position with V-band magnitude within 2 mag of the G-magnitude reported by *Gaia*. We note that most of the HMXBs are, to some extent, variable in the optical band so an exact comparison would be unfeasible. This meant that the threshold of two magnitudes was determined empirically by inspecting the observed difference between the literature and *Gaia* magnitudes for sources where the *Gaia* counterpart was already unambiguously identified.

For all HMXBs with a *Gaia* counterpart, we provide distance information from Gaia Collaboration et al. (2023), Bailer-Jones et al. (2021),[11] and Anders et al. (2022).[12] In addition, for objects without an identified *Gaia* counterpart, but with available distance estimates in the literature, we give those estimates and their corresponding references. If multiple distance estimates were available, the mean distance was calculated by using the arithmetic mean on all available distance estimations linked to the given source. The range of possible distances, calculated by taking the lowest and highest estimations of all distance estimates for a given system (from the literature or from *Gaia*) is also reported.

2.4. Additional information

We also attempted to include some extra information related to the properties of the optical counterparts and the compact objects. For instance, in addition to the G-band magnitudes of *Gaia* published in Gaia Collaboration et al. (2023), magnitudes in the J-, H-, and K-bands provided by Cutri et al. (2003) as well as magnitudes in the W1- and W2-bands of the Wide-field Infrared Survey Explorer mission (Wright et al. 2010) in CatWISE2020[13] (Marocco et al. 2021) and available V-band magnitudes were

[4] https://heasarc.gsfc.nasa.gov/W3Browse/xmm-newton/xmmssc.html
[5] https://vizier.cds.unistra.fr/viz-bin/VizieR-3?-source=IX/57/csc2master
[6] https://vizier.cds.unistra.fr/viz-bin/VizieR-3?-source=IX/58/2sxps
[7] https://heasarc.gsfc.nasa.gov/W3Browse/swift/swbat105m.html
[8] https://vizier.cds.unistra.fr/viz-bin/VizieR-3?-source=J/A%2bA/545/A27
[9] https://vizier.cds.unistra.fr/viz-bin/VizieR-3?-source=I/355
[10] https://vizier.cds.unistra.fr/viz-bin/VizieR?-source=II/246
[11] https://vizier.cds.unistra.fr/viz-bin/VizieR-3?-source=I/352
[12] https://vizier.cds.unistra.fr/viz-bin/VizieR-3?-source=I/354/starhorse2021
[13] https://vizier.cds.unistra.fr/viz-bin/VizieR?-source=II/365

included. Any luminosity estimates of the optical companions from Gaia Collaboration et al. (2023) were also added. Since the spectral type of the counterpart is also pertinent information, we attempted to include this information by using the following sources: Kretschmar et al. (2019), Staubert et al. (2019), Liu et al. (2006), Mauro Orlandini's website,[14] and *SIMBAD*. Due to the close connection between spectral type and effective stellar temperature, estimations of the temperatures provided by Anders et al. (2022) and Gaia Collaboration et al. (2023) were included. The catalogue includes only the mean stellar effective temperature. One of the key properties of NS systems is the magnetic field strength of the compact object. This can be measured using observed energies of the cyclotron resonance scattering features (CRSFs, or cyclotron lines). We therefore included the literature values of the observed CRSF energies where such features were claimed to be detected. This includes the fundamental line as well as harmonics. The line energies and corresponding references were sourced from the recent review by Staubert et al. (2019) and the X-ray pulsar properties database by Mauro Orlandini, which appears to cover all X-ray pulsars where a detection of a CRSF was claimed in the literature.

3. Catalogue content and quality assurance

3.1. Description of the fields

The Galactic High Mass X-ray Binary catalogue (XRBcats) we present here contains a total of 169 HMXBs and candidates, sorted according to increasing right ascension (second column). The table consists of 66 columns, listing the various parameters and references for a given HMXB. The first column contains the source name, as decided by the most common name in the literature (number of mentions in NASA ADS system). The following seven columns are dedicated to the coordinates of the system, the second and third columns displaying the right ascension (RA) and declination (DEC) in degrees, followed by statistical uncertainties of the coordinates in arcseconds. The Coord_Ref column provides the reference of the catalogue or paper, which was used to extract the coordinates and uncertainties (e.g. Gaia Collaboration et al. (2023) for *Gaia* DR3), given as a NASA ADS bibcode. The sixth column indicates whether the optical counterpart is solidly identified in the literature (0), if it is a tentative optical counterpart identified as such in the literature (1) or if it is not yet identified (2). In the seventh and eighth columns the galactic longitude (GLON) and galactic latitude (GLAT) in degrees can be found. The following column displays the different X-ray flags related to HMXB classification, which were discussed in Sect. 2. Columns 10 and 11 provide the orbital period of the compact object in days and the spin period of the pulsar (where appropriate) in seconds, respectively. For NS HMXBs with CRSFs reported in the literature, line energies are listed in column 12 in units of keV regardless of if it is reporting on the fundamental line or any harmonics. In the Alt_name column, the second most-used identifier in the literature was selected as an alternative name for the HMXB. Column 14 displays the spectral type of the optical companion. If it was possible to identify the *Gaia* counterpart, the *Gaia*-DR3-ID is listed in column 15. Column 16 and 17 show the magnitude in the G-band as well as its uncertainty followed by the V-band magnitude in Column 18 and its uncertainty in Column 19. In Columns 20-29, the JHK-magnitudes as well as the W1- and W2-magnitudes with their respective uncertainties are shown. The neutral hydrogen column density in units of $10^{21}\mathrm{cm}^{-2}$ is shown in column 30, which is available in Evans et al. (2020). In this reference hardness ratios were first taken and utilised to produce a power-law spectrum through interpolation; from this interpolated spectrum, the neutral hydrogen column density best fitting that spectrum was derived. The following 11 columns contain information on the X-ray flux. Columns 31 and 32 are the minimum and maximum flux values of the source in the XMM-Newton catalogue. Columns 33 and 34 are the flux values of the source in Chandra, due to the use of both Chandra HRC and ACIS; column 35 indicates which of these two instruments was used for the flux values. Columns 36 and 37 respectively display the minimum and maximum flux values of *Swift*/XRT of the source, columns 38 and 39 for *Swift*/BAT, and Columns 40 and 41 for INTEGRAL. In cases where only one observation was taken the same value was adopted for minimum and maximum flux values. Columns 42-44 contain mass estimates of the compact object, in particular mean mass, as well as the upper and lower mass limits reported in the literature (in $\mathrm{M}_\odot$). Columns 45-47 contain distance estimates (in parsec) to a given source, including the mean distance and the upper and lower limits given in the literature. The stellar effective temperature and the luminosity of the optical counterpart can be found in columns 48 and 49, where T_{eff} is in Kelvin and the luminosity of the companion is in $L_\odot$. All *SIMBAD* identifiers associated with HMXBs are quoted in column 50. The next seven columns are dedicated to the references of CRSF, pulsation period, orbital parameter, spectral type, distance-estimation (if literature values were used), mass estimation, and miscellaneous references. Column 58 is dedicated to comments (e.g. if the source is considered an HMXB candidate or similar). The final eight columns contain the source name given in the following catalogues: 2MASS All-Sky Catalogue of Point Sources, CatWISE2020 catalogue, Second *ROSAT* all-sky survey (2RXS) source catalogue, *XMM-Newton* Serendipitous Source Catalogue, Chandra Source Catalogue (CSC) Release 2.0, 2SXPS Swift X-ray telescope point source catalogue, *Swift*/BAT 105-Month All-Sky Hard X-Ray Survey catalogue, and *INTEGRAL/IBIS* 9-year Galactic Hard X-Ray Survey catalogue.

3.2. Finding charts and problematic cases

As part of the catalogue we provide finding charts, which consist of up to six different images ranging from near-infrared (NIR) to hard X-rays for all sources. For the majority of the finding charts, we used the Hierarchical Progressive Surveys (HiPS, Fernique et al. 2015); only in the case of *Swift*/XRT did we use the SkyView Query. Both HiPS and SkyView offer the possibility to query data automatically with Python. To access HiPS, and SkyView we used the astroquery.hips2fits[15] package and the astroquery.skyview[16] package, respectively. In the following we give details of the surveys used and provide their corresponding links as footnotes. The finding charts consist of up to six different surveys, which are mentioned below, along with their corresponding links as footnotes. In the top row we include the image taken from the Visible and Infrared Survey Telescope for Astronomy (VISTA) from their Variables in the the Via Lactea (VVV[17]) DR4 catalogue (Minniti et al. 2010). Alternatively, for the top row image, where

[14] http://www.iasfbo.inaf.it/~mauro/pulsar_list.html

[15] https://alasky.u-strasbg.fr/hips-image-services/hips2fits

[16] https://astroquery.readthedocs.io/en/latest/skyview/skyview.html

[17] http://alasky.cds.unistra.fr/VISTA/VVV_DR4/VISTA-VVV-DR4-J/

VVV was not available we utilised 2MASS.[18] The central image is taken from *unWISE*[19] (Schlafly et al. 2019) and for the right-hand RGB image we utilised *Chandra*,[20] *XMM-Newton*,[21] or the Roentgensatellit (*ROSAT*;[22] Truemper 1982; Boller et al. 2016; Voges et al. 1999) (listed here in order of preference). In the left-hand corner of the bottom row we provide a soft X-ray image of *Swift*/XRT (SwiftXRTInt in astroquery.skyview). For hard X-rays we take images from *Swift*/BAT[23] (middle section of bottom row); and *INTEGRAL*[24] (right hand section of bottom row). A 1 arcmin field of view was used for the creation of the VVV, 2MASS, *unWISE*, *XMM-Newton*, and *Chandra* images. In the case of *Swift*/XRT and *ROSAT*, we used a field of view size of 5 arcmin and 15 arcmin, respectively. The field of view for *Swift*/BAT and *INTEGRAL* was chosen to be 10°. In each case, the size of the region was chosen considering the field of view and angular resolution of a given instrument. Every panel also shows the coordinates and uncertainties of all detected sources within their respective regions (position uncertainties are represented by error circles). A red cross indicates the position given by *SIMBAD* for the source, and a dodger-blue diamond for the coordinates described in the literature. The position of the source used by this catalogue is indicated with an orange star. In the case of the soft X-ray instruments, the position of the observations is indicated by the error circles to prevent overcrowding, a golden circle indicates the *Chandra* position, a red circle *XMM-Newton*, a green circle *Swift*/XRT, and a navy blue circle *ROSAT*. *Swift*/BAT and *INTEGRAL* are denoted by a deep pink pentagon and a lime green triangle, respectively. In the optical band we indicate *CatWISE* with an orange X, 2MASS with a cyan plus sign, and *Gaia* DR3 data with purple square. As an example, Figure 2 shows the finding chart of GRO J1008−57.

Based on visual inspection of the finding charts and literature research, several problematic cases were identified. We list these cases in their respective categories, in ascending order of their right ascension coordinates. Several sources initially assumed to be HMXBs were removed from the sample.

1E 1048.1-5937: 1E 1048.1-5937 is listed as an HMXB in *SIMBAD*; however, Dib et al. (2009) concluded that the source is actually a magnetar. The source is also listed as a magnetar in the McGill magnetar database[25] Olausen & Kaspi (2014).

IGR J18151-1052: IGR J18151-1052 was suggested to be an HMXB (Burenin et al. 2009); however, this was shown not to be the case by Lutovinov et al. (2012). The object might be associated with the magnetar candidate PSR J1845-0258 or be a CV, but in any case its identification as an HMXB is unlikely, so we decided not to include this source.

1E 2259+58.6: Another magnetar 1E 2259+58.6 (Gavriil & Kaspi 2002) was excluded using the same logic as for 1E 1048.1-5937.

Several objects have tentative or known optical counterparts in the literature, but they could not be found automatically through the procedure outlined above. For these objects, the literature was searched manually and the known counterparts and their coordinates were added to the catalogue.

RX J0148.9+6121: Not much is known about RX J0148.9+6121 which was only referred to once by Wang et al. (2014) as having HMXB status. We therefore consider it to be a candidate rather than a confirmed HMXB.

PSR J0635+0533: Fortin et al. (2022b) compiled a list of galactic HMXBs that contain a NS as their compact object, and made an effort to identify optical counterparts for the systems in Gaia DR3. The study only lists objects with unambiguously identified counterparts both in *Gaia* DR3 and 2MASS catalogues that are within 0.5" of each other. In the case of PSR J0635+0533, they identified *Gaia* DR3 3131755947406031104 as the counterpart.

1H 0749-600: For 1H 0749-600, Torrejón & Orr (2001) posited that the proposed optical counterpart HD 65663 is not the real counterpart, but rather a single Be star spatially coincident with an X-ray transient. Torrejón & Orr (2001) also considered the possibility that the system is not an X-ray binary at all. We therefore classify this association as tentative.

1FGL J1018.6-5856: For 1FGL J1018.6-5856 the same procedure was performed as in the case of PSR J0635+0533. Here Fortin et al. (2022b) identified *Gaia* DR3 5255509901121774976 as the *Gaia* counterpart for 1FGL J1018.6-5856.

1ES 1210-64.6: Based on the coordinates of the soft X-ray counterpart of 1ES 1210-64.6 (Revnivtsev et al. 2007), Masetti et al. (2009) identified the optical counterpart (*Gaia* DR3 6053076566300433920) This conclusion was confirmed by follow-up optical spectroscopy.

IGR J12341-6143: A soft X-ray counterpart for IGR J12341-6143 was discovered quite recently by Sidoli et al. (2020) with *Swift*/XRT, which also led to the identification of a tentative optical counterpart (*Gaia* DR2 6054778507172454912).

1A 1238-59: We suggest classifying 1A 1238-59 as an HMXB candidate, due to an error radius of 30" (Dower et al. 1978) and because there is no detected optical counterpart.

IGR J14059-6116: We decided to classify IGR J14059-6116 as an HMXB candidate, due to a missing optical counterpart. Corbet et al. (2019) suggested that IGR J14059-6116 has a possible association with the HMXB 4FGL J1405.1-6119, and therefore we note that IGR J14059-6116 is likely to be the same source as 4FGL J1405.1-6119.

MAXI J1409-619: Kennea et al. (2010) located an uncatalogued X-ray source inside the MAXI error circle of MAXI J1409-619 using *Swift*/XRT. Inside the *Swift*/XRT error circle of this source,

[18] http://alasky.cds.unistra.fr/2MASS/J/
[19] http://alasky.cds.unistra.fr/unWISE/W1/
[20] https://cdaftp.cfa.harvard.edu/cxc-hips/
[21] http://skies.esac.esa.int/XMM-Newton/EPIC-RGB/
[22] http://alasky.cds.unistra.fr/RASS/
[23] http://cade.irap.omp.eu/documents/Ancillary/4Aladin/BAT_14_20/
[24] http://cade.irap.omp.eu/documents/Ancillary/4Aladin/INTEGRAL_17_60/
[25] https://www.physics.mcgill.ca/~pulsar/magnetar/main.html

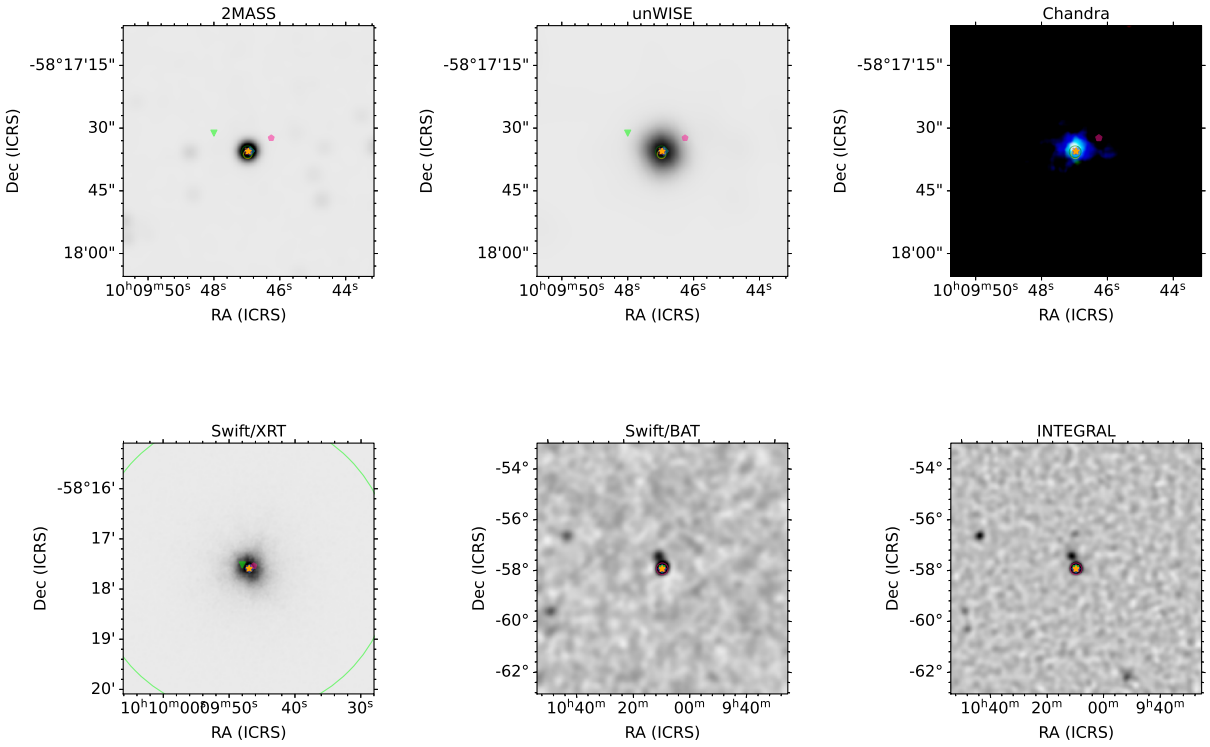

Fig. 2. Finding charts of GRO J1008−57. The finding charts are overlaid with symbols and error circles to indicate observations of different instruments. See text in Sect. 3.2 for an explanation of the finding charts and the symbols.

a catalogued IR source (2MASS J14080271-6159020) was also found which is considered a tentative optical counterpart.

IGR J14331-6112: *Gaia* DR3 5878377736381364608 is mentioned as the unambiguous optical counterpart of IGR J14331-6112 by Fortin et al. (2022b).

Cir X−1: Since its discovery, Cir X−1 has been referred to as an LMXB, until Heinz et al. (2013) determined the age of the system to be about 4500 yr. In addition, according to Jonker et al. (2007) this system contains an A0- to B5-type supergiant companion. However, Cir X-1 has also shown type I X-ray bursts (Tennant et al. 1986), which indicates that source is an LMXB. The possible LMXB origin is also supported by the fact that the companion star itself in Cir X-1 still cannot be unambiguously detected at optical wavelengths. Johnston et al. (2016) concluded that the donor could either be a low mass star that has not had time to evolve or a giant star still recovering from the impact of a supernova blast that happened less than 5000 yr ago. Taking into account all this obscurity around Cir X-1's nature we decided to add it to both LMXB and HMXB catalogues.

XTE J1543-568: In March 2012 *Swift*/BAT detected an increased flux from XTE J1543-568, which led to a more accurate determination of the source position. This allowed Krimm et al. (2012) to identify a tentative counterpart (2MASS J15440515-5645425) within the error box provided by *Swift*/XRT.

2S 1553-542: With the help of *Swift*/XRT and *Chandra* observations, Lutovinov et al. (2016) were capable of identifying a likely infrared counterpart for 2S 1553-542 at RA(J2000)=15h 57m 48.28s DEC(J2000)=-54°24' 53.5".

IGR J16374-5043: Inside the error circle around the *Swift*/XRT position of IGR J16374-5043, Sguera et al. (2020) found only one infrared source. This source is not listed in the 2MASS catalogue but is in the catalogue of *Gaia* (*Gaia* DR3 5940285090075838848) and is likely to be the optical counterpart of IGR J16374-5043.

XTE J1716-389: Ratti et al. (2010) used *Chandra* for localisation of Galactic X-ray sources and did follow-up observations in the optical and NIR bands. One of the observed sources was XTE J1716-389. The refined *Chandra* position allowed Ratti et al. (2010) to identify the only possible optical counterpart, an

infrared source 2MASS J17155645-3851537, that is thus considered to be XTE J1716-389's counterpart.

IGR J17375-3022: IGR J17375-3022 was a poorly studied source until Sguera et al. (2020) investigated it in the hard and soft X-ray bands, and in the infrared band. With an enhanced source position from *Swift*/XRT, the study found only one NIR object within the *Swift*/XRT error circle in the VVV survey. Therefore, Sguera et al. (2020) proposed that VVV J173733.74-302314.5 is the best counterpart candidate for IGR J17375-3022.

RX J1739.4-2942: RX J1739.4-2942, originally identified as an LMXB, could potentially be a Be/HMXB Bahramian et al. (2016). Therefore, we included RX J1739.4-2942 in the catalogue as an HMXB candidate (Number 67 in Liu et al. 2006).

IGR J18029-2016: Walter et al. (2006) proposed two possible NIR counterparts for IGR J18029-2016; they were 2MASS J18024194-2017172 and 2MASS J180242.0-201720.2, which were found in the 2MASS catalogue and the Second Guide Star Catalogue, respectively. The first candidate, 2MASS J18024194-2017172, was later confirmed to be the counterpart of the HMXB by Masetti et al. (2008).

IGR J18179-1621: With the refined position of IGR J18179-1621 reported by Li et al. (2012), Nowak et al. (2012) were able to observe the object with *Chandra* and identify a possible optical counterpart. 2MASS J18175218-1621316 was identified as a possible companion, due to it being the only NIR source in the 2MASS catalogue within a 1" radius of the *Chandra* position.

IGR J18219-1347: Quite recently O'Connor et al. (2022) identified a bright IR counterpart for IGR J18219-1347 close to the *Chandra* localisation, at RA(J2000)=18h 21m 54.821s DEC(J2000)=-13°47' 26.703", which appeared to be the combination of two point sources (Star A and Star B). They concluded that Star A is the Counterpart of IGR J18219-1347, because it is consistent with the SED of a Be star, and therefore the system was classified as a BeXRB.

AX J1841.0-0536: Fortin et al. (2022a) queried the confirmed HMXBs of their previous work (Fortin et al. 2022b) in *Gaia* DR3. For AX J1841.0-0536 the source *Gaia* DR3 4256500538116700160 was therefore identified as an optical counterpart.

Ginga 1839-04: For *Ginga* 1839-04 no optical counterpart has yet been identified. Liu et al. (2006) included this source in their catalogue due to a tentative pulsation detection of ∼ 81s (Koyama et al. 1990) by *Ginga* during an outburst in 1989. Since then no further X-ray detections have been reported (Sguera et al. 2009). Therefore, *Ginga* 1839-04 is classified as a candidate HMXB in this catalogue.

IGR J18482+0049: Bodaghee et al. (2012) observed five *INTEGRAL* sources towards the Scutum Arm, one of which was IGR J18482+0049. With the refined position, they found only one object in the 2MASS catalogue that was consistent with the *XMM-Newton* position. Based on this observation, IGR J18482+0049 has a possible association with 2MASS J18481540+0047332.

Ginga 1855-02: Within *Ginga* 1855-02, the positional error is 10′ (Koyama et al. 1990). Like *Ginga* 1839-04, *Ginga* 1855-02 is a poorly studied source that does not have an identified optical counterpart, and therefore it is also classified as a candidate HMXB based on its transient behaviour.

XTE J1859+083: After an outburst of XTE J1859+083 detected by MAXI (Negoro et al. 2015), follow-up *Swift*/XRT observations by Li & Kong (2015) allowed the improvement of the position of the HMXB. No UVOT counterpart was detected, but with the enhanced position Li & Kong (2015) were able to find a possible counterpart in the USNO-B1.0 (USNO-B1.0 0982-0467424) and 2MASS catalogues (2MASS J18590163+0814444).

1E 1912.5+1031: Bozzo et al. (2011) identified 2MASS J19145680+1036387 as the most likely counterpart of 1E 1912.5+1031, based on the position inside the error circle of their estimated *Swift*/XRT position for 1E 1912.5+1031.

AX J1949.8+2534: For AX J1949.8+2534 the source 2MASS J19495543+2533599 was proposed to be the optical counterpart (Sguera et al. 2017) . This was later confirmed to be the case by Hare et al. (2019).

W63 X-1: W63 X-1 is an X-ray binary within the supernova remnant W63, with a pulsation period of 36 sec (Rho et al. 2004). Based on the pulsation period and spectrum, Rho et al. (2004) concluded that the companion is likely an isolated neutron star, HMXB, or LMXB. They found an optical counterpart with $H\alpha$-excess emission typical for a Be companion, and thus classified the source as an HMXB.

Several objects present in Liu et al. (2006) were removed from the current catalogue as they are no longer classified as HMXBs:

1WGA J0648.0-4419: 1WGA J0648.0-4419, previously listed as source 18 in Liu et al. (2006), was removed because the optical star in the system has since been classified as a hot sub-dwarf (Jaschek & Jaschek 1963).

IGR J12349-6434: IGR J12349-6434 (source 35 in Liu et al. (2006)] was initially classified as a new source. However, it is thought to be associated with RT Cru (Tueller et al. 2005), a symbiotic star containing a WD (Luna & Sokoloski 2007). It was therefore excluded from the catalogue.

1A 1246-588: 1A 1246-588, which was source 38 in Liu et al. (2006), is an LMXB Bassa et al. (2006).

SAX J1452.8-5949: With the de-reddened magnitudes of their observations in the JHK-bands and the assumption of a blackbody model, Kaur et al. (2009) made estimations of the distance of SAX J1452.8-5949 (source 46 in Liu et al. 2006). This ruled out the possibility of the object being an HMXB, due to the fact that the system would be an extragalactic source. They concluded

that the binary system must have a low mass companion, and therefore is either an LMXB or an intermediate polar (IP, accreting magnetised white dwarf).

IGR J16358-4726: Chaty et al. (2008) classified IGR J16358-4726 (source 55 in Liu et al. 2006) as an HMXB; however, this classification was revoked by Nespoli et al. (2010) and the source is now considered to be a symbiotic X-ray binary.

AX J1700.1-4157: Based on NIR observations, Kaur et al. (2010) estimated that the companions of AX J1700.1-4157[26] (source 63 in Liu et al. 2006) should be a low mass star. In combination with a detected Fe emission line, Kaur et al. (2010) concluded that AX J1700.1-4157 is most likely an IP, and therefore AX J1700.1-4157 was removed from this catalogue.

IGR J17091-3624: IGR J17091-3624 (source 64 in Liu et al. 2006) is also now classified as an LMXB (Grinberg et al. 2016).

AX J1740.1-2847: AX J1740.1-2847 (source 68 in Liu et al. 2006) is a similar case to AX J1700.1-4157. Kaur et al. (2010) also estimated that the companion should be a low mass star, and due to a detected Fe emission line they concluded that AX J1740.1-2847 is most likely an IP as well, and hence it was removed from the catalogue.

4U 1807-10: 4U 1807-10 (source 75 in Liu et al. 2006) was detected by *UHURU* (Forman et al. 1978) within a large error of 1.3°. To date, it is not certain if 4U 1807-10 is an HMXB or an LMXB. However, it is more likely that 4U 1807-10 is an LMXB as the system shows type I X-ray bursts (Chelovekov et al. 2017). Therefore, we excluded it from this catalogue.

SAX J1819.3-2525: MacDonald et al. (2014) determined a mass of 2.9 $M_{\odot}$ for the optical companion of SAX J1819.3-2525[26] (source 77 in Liu et al. 2006), which classifies this system as an IMXB, and therefore it was excluded from the catalogue.

AX J1838.0-0655: AX J1838.0-0655[26] (source 82 in Liu et al. 2006) is currently classified as a supernova remnant. Malizia et al. (2005) does not exclude the possibility of AX J1838.0-0655 being an X-ray binary, but mentions that this scenario is unlikely due to the lack of strong X-ray and γ-ray variability, as well as the extension of the source to up to TeV energies. Therefore, AX J1838.0-0655 was removed from the catalogue.

XTE J1901+014: Karasev et al. (2008) proposed that XTE J1901+014 (source 94 in Liu et al. 2006) could be the first low mass fast X-ray transient. To date, the nature of this system is not completely clear (Sato et al. 2019); we therefore decided to exclude this source from the current version of this catalogue.

XTE J1906+09: XTE J1906+09 (source 96 in Liu et al. 2006) was not excluded, but the name was changed to XTE J1906+090 to match that commonly used in the literature.

A handful of sources that are included in the recently published catalogue of high mass X-ray binaries by Fortin et al. (2023) have been omitted from our catalogue. These sources have already been mentioned and are AX J1700.1-4157, SAX J1819.3-2525, AX J1838.0-0655, and GRS 1758-258. In the case of GRS 1758-258, there is a possibility that the system is an intermediate-mass X-ray binary, as proposed by Martí et al. (2016), and hence this source can be found in Avakyan et al. (2023) instead of this catalogue.

4. Conclusion

The Major changes with respect to Liu et al. (2006), in addition to the problematic cases, are described here.

- We homogenised the energy ranges of the reported X-ray fluxes. Liu et al. (2006) used an energy range of 2 − 10 keV for most sources, but in some cases the nominal energy range was different, and identifying these cases was not trivial. We now quote the soft and hard X-ray fluxes in well-defined energy ranges separately.
- Liu et al. (2006) only reported the maximum value of X-ray flux in units of Jy in most cases. In this work we report flux ranges in the two energy bands in the more commonly used cgs units, which are more accessible for X-ray sources.
- We increased the number of flags used to characterise source properties from 6 in Liu et al. (2006) to a total of 15 to better reflect the various features reported in the literature.
- While Liu et al. (2006) flags sources where a cyclotron line was detected, no information regarding the energy is available in most cases. We report both the observed energies and corresponding references. The number of objects where a line was detected also increased substantially due to the availability of new observations and publications.
- Effective stellar temperature and estimated optical luminosity, as well as the hydrogen column density are three completely new fields introduced in this version of the catalogue.
- Finally, we include up to six finding charts as part of the catalogue (from NIR images to hard X-ray bands) instead of referencing the existing finding charts.

Differences with respect to Fortin et al. (2023) are as follows:

- Fortin et al. (2023) utilised a flag to indicate the type of the optical companion. We used similar flags for the optical companion, but introduced additional flags for the compact object (e.g. CRSF to indicate if a neutron star has a detected cyclotron line).
- For sources with known cyclotron line energies we included both fundamental and harmonic energies.
- In addition to the cyclotron line energy, we also reported X-ray fluxes in different energy ranges for the compact object. This can be used to gauge the variability of the source and to make an estimation of the expected flux, although this cannot replace an in-depth analysis of individual sources.
- For the optical companions, we reported magnitudes in the optical and in the NIR bands. Some additional information regarding the properties of optical counterparts can be found in Fortin et al. (2023).

[26] It can be found in the recently published catalogue of high mass X-ray binaries in the Galaxy by Fortin et al. (2023).

Together with the catalogues of Fortin et al. (2023) and Avakyan et al. (2023), this catalogue provides a useful tool for further studies of XRBs. With ongoing surveys like eROSITA, the number of known XRBs is expected to increase substantially (Doroshenko et al. 2014); therefore, we plan to keep the web version of our catalogue[27] up-to-date to the best of our ability.

Acknowledgements. This research has made use of the SIMBAD database and VizieR catalogue access tool operated at CDS, Strasbourg, France, and NASA's Astrophysics Data System (ADS). This research made use of hips2fits[15], a service provided by CDS. AA thanks Deutsche Forschungsgemeinschaft (DFG) within the eROSTEP research unit under DFG project number 414059771 for support (DO 2307/2-1). This work has made use of data from the European Space Agency (ESA) mission *Gaia* (`https://www.cosmos.esa.int/gaia`), processed by the *Gaia* Data Processing and Analysis Consortium (DPAC, `https://www.cosmos.esa.int/web/gaia/dpac/consortium`). Funding for the DPAC has been provided by national institutions, in particular the institutions participating in the *Gaia* Multilateral Agreement. We acknowledge the public data from *XMM-Newton*, *Chandra*, *Swift* and *INTEGRAL*.

References

Anders, F., Khalatyan, A., Queiroz, A. B. A., et al. 2022, A&A, 658, A91
Avakyan, A., Neumann, M., Zainab, A., et al. 2023, A&A, 675, A199
Bahramian, A., Heinke, C. O., Sivakoff, G. R., et al. 2016, The Astronomer's Telegram, 8704, 1
Bailer-Jones, C. A. L., Rybizki, J., Fouesneau, M., Demleitner, M., & Andrae, R. 2021, AJ, 161, 147
Balona, L. A. & Ozuyar, D. 2020, MNRAS, 493, 2528
Barthelmy, S. D., Barbier, L. M., Cummings, J. R., et al. 2005, Space Sci. Rev., 120, 143
Bassa, C. G., Jonker, P. G., in't Zand, J. J. M., & Verbunt, F. 2006, A&A, 446, L17
Bodaghee, A., Tomsick, J. A., & Rodriguez, J. 2012, ApJ, 753, 3
Boller, T., Freyberg, M. J., Trümper, J., et al. 2016, A&A, 588, A103
Bozzo, E., Ferrigno, C., Pavan, L., Walter, R., & Stella, L. 2011, The Astronomer's Telegram, 3326, 1
Burenin, R., Makarov, D., Uklein, R., Revnivtsev, M., & Lutovinov, A. 2009, The Astronomer's Telegram, 2193, 1
Burrows, D. N., Hill, J. E., Nousek, J. A., et al. 2005, Space Sci. Rev., 120, 165
Chaty, S. 2022, Accreting Binaries; Nature, formation, and evolution (IOP Publishing)
Chaty, S., Rahoui, F., Foellmi, C., et al. 2008, A&A, 484, 783
Chelovekov, I. V., Grebenev, S. A., Mereminskiy, I. A., & Prosvetov, A. V. 2017, Astronomy Letters, 43, 781
Corbet, R. H. D. 1986, MNRAS, 220, 1047
Corbet, R. H. D., Chomiuk, L., Coe, M. J., et al. 2019, ApJ, 884, 93
Cutri, R. M., Skrutskie, M. F., van Dyk, S., et al. 2003, 2MASS All Sky Catalog of point sources.
Dib, R., Kaspi, V. M., & Gavriil, F. P. 2009, ApJ, 702, 614
Doroshenko, V., Ducci, L., Santangelo, A., & Sasaki, M. 2014, A&A, 567, A7
Doroshenko, V., Zhang, S. N., Santangelo, A., et al. 2020, MNRAS, 491, 1857
Dower, R. G., Apparao, K. M. V., Bradt, H. V., et al. 1978, Nature, 273, 364
Evans, I. N., Primini, F. A., Glotfelty, K. J., et al. 2010, ApJS, 189, 37
Evans, P. A., Page, K. L., Osborne, J. P., et al. 2020, ApJS, 247, 54
Fernique, P., Allen, M. G., Boch, T., et al. 2015, A&A, 578, A114
Forman, W., Jones, C., Cominsky, L., et al. 1978, ApJS, 38, 357
Fortin, F., García, F., & Chaty, S. 2022a, A&A, 665, A69
Fortin, F., García, F., Chaty, S., Chassande-Mottin, E., & Simaz Bunzel, A. 2022b, A&A, 665, A31
Fortin, F., García, F., Simaz Bunzel, A., & Chaty, S. 2023, A&A, 671, A149
Gaia Collaboration, Prusti, T., de Bruijne, J. H. J., et al. 2016, A&A, 595, A1
Gaia Collaboration, Vallenari, A., Brown, A. G. A., et al. 2023, A&A, 674, A1
Gavriil, F. P. & Kaspi, V. M. 2002, ApJ, 567, 1067
Gehrels, N., Chincarini, G., Giommi, P., et al. 2004, ApJ, 611, 1005
Grimm, H. J., Gilfanov, M., & Sunyaev, R. 2002, Mem. Soc. Astron. Italiana, 73, 1053
Grimm, H. J., Gilfanov, M., & Sunyaev, R. 2003, MNRAS, 339, 793
Grinberg, V., Fuerst, F., Ballhausen, R., et al. 2016, The Astronomer's Telegram, 8761, 1
Hare, J., Halpern, J. P., Clavel, M., et al. 2019, ApJ, 878, 15
Heinz, S., Sell, P., Fender, R. P., et al. 2013, ApJ, 779, 171
Jansen, F., Lumb, D., Altieri, B., et al. 2001, A&A, 365, L1
Jaschek, M. & Jaschek, C. 1963, PASP, 75, 365
Johnston, H. M., Soria, R., & Gibson, J. 2016, MNRAS, 456, 347
Jonker, P. G., Nelemans, G., & Bassa, C. G. 2007, MNRAS, 374, 999
Karasev, D. I., Lutovinov, A. A., & Burenin, R. A. 2008, Astronomy Letters, 34, 753
Kaur, R., Wijnands, R., Patruno, A., et al. 2009, MNRAS, 394, 1597
Kaur, R., Wijnands, R., Paul, B., Patruno, A., & Degenaar, N. 2010, MNRAS, 402, 2388
Kennea, J. A., Krimm, H., Romano, P., et al. 2010, The Astronomer's Telegram, 2962, 1
Koyama, K., Kawada, M., Kunieda, H., Tawara, Y., & Takeuchi, Y. 1990, Nature, 343, 148
Kretschmar, P., El Mellah, I., Martínez-Núñez, S., et al. 2021, A&A, 652, A95
Kretschmar, P., Fürst, F., Sidoli, L., et al. 2019, New A Rev., 86, 101546
Krimm, H. A., Barthelmy, S. D., Baumgartner, W., et al. 2012, The Astronomer's Telegram, 4008, 1
Krivonos, R., Tsygankov, S., Lutovinov, A., et al. 2012, A&A, 545, A27
Kudritzki, R.-P. & Puls, J. 2000, ARA&A, 38, 613
Li, J., Zhang, S., Torres, D. F., et al. 2012, MNRAS, 426, L16
Li, K. L. & Kong, A. K. H. 2015, The Astronomer's Telegram, 7067, 1
Liu, Q. Z., van Paradijs, J., & van den Heuvel, E. P. J. 2006, A&A, 455, 1165
Luna, G. J. M. & Sokoloski, J. L. 2007, ApJ, 671, 741
Lutovinov, A. A., Buckley, D. A. H., Townsend, L. J., Tsygankov, S. S., & Kennea, J. 2016, MNRAS, 462, 3823
Lutovinov, A. A., Burenin, R. A., Revnivtsev, M. G., & Bikmaev, I. F. 2012, Astronomy Letters, 38, 1
MacDonald, R. K. D., Bailyn, C. D., Buxton, M., et al. 2014, ApJ, 784, 2
Malizia, A., Bassani, L., Stephen, J. B., et al. 2005, ApJ, 630, L157
Marocco, F., Eisenhardt, P. R. M., Fowler, J. W., et al. 2021, ApJS, 253, 8
Martí, J., Luque-Escamilla, P. L., & Muñoz-Arjonilla, Á. J. 2016, A&A, 596, A46
Masetti, N., Mason, E., Morelli, L., et al. 2008, A&A, 482, 113
Masetti, N., Parisi, P., Palazzi, E., et al. 2009, A&A, 495, 121
Minniti, D., Lucas, P. W., Emerson, J. P., et al. 2010, New A, 15, 433
Negoro, H., Suzuki, K., Namba, T., et al. 2015, The Astronomer's Telegram, 7034, 1
Negueruela, I., Smith, D. M., Reig, P., Chaty, S., & Torrejón, J. M. 2006, in ESA Special Publication, Vol. 604, The X-ray Universe 2005, ed. A. Wilson, 165
Nespoli, E., Fabregat, J., & Mennickent, R. E. 2010, A&A, 516, A94
Nowak, M. A., Paizis, A., Rodriguez, J., et al. 2012, ApJ, 757, 143
O'Connor, B., Göğüş, E., Huppenkothen, D., et al. 2022, ApJ, 927, 139
Oh, K., Koss, M., Markwardt, C. B., et al. 2018, ApJS, 235, 4
Olausen, S. A. & Kaspi, V. M. 2014, ApJS, 212, 6
Pfahl, E., Rappaport, S., & Podsiadlowski, P. 2003, ApJ, 597, 1036
Ratti, E. M., Bassa, C. G., Torres, M. A. P., et al. 2010, MNRAS, 408, 1866
Reig, P. 2011, Ap&SS, 332, 1
Revnivtsev, M., Sunyaev, R., Lutovinov, A., & Sazonov, S. 2007, The Astronomer's Telegram, 1253, 1
Rho, J., Moon, D. S., Gotthelf, E., Pannuti, T., & Corbet, R. 2004, in AAS/High Energy Astrophysics Division, Vol. 8, AAS/High Energy Astrophysics Division #8, 17.30
Sato, T., Negoro, H., Iwakiri, W., et al. 2019, The Astronomer's Telegram, 13328, 1
Savonije, G. J. 1978, A&A, 62, 317
Schlafly, E. F., Meisner, A. M., & Green, G. M. 2019, ApJS, 240, 30
Sguera, V., Romero, G. E., Bazzano, A., et al. 2009, ApJ, 697, 1194
Sguera, V., Sidoli, L., Bird, A. J., Paizis, A., & Bazzano, A. 2020, MNRAS, 491, 4543
Sguera, V., Sidoli, L., Paizis, A., et al. 2017, MNRAS, 469, 3901
Sidoli, L., Esposito, P., & Sguera, V. 2020, The Astronomer's Telegram, 14039, 1
Staubert, R., Trümper, J., Kendziorra, E., et al. 2019, A&A, 622, A61
Tananbaum, H., Gursky, H., Kellogg, E. M., et al. 1972, ApJ, 174, L143
Tennant, A. F., Fabian, A. C., & Shafer, R. A. 1986, MNRAS, 221, 27P
Torrejón, J. M. & Orr, A. 2001, A&A, 377, 148
Truemper, J. 1982, Advances in Space Research, 2, 241
Tueller, J., Gehrels, N., Mushotzky, R. F., et al. 2005, The Astronomer's Telegram, 591, 1
van den Eijnden, J., Degenaar, N., Russell, T. D., et al. 2022, MNRAS, 516, 4844
van den Eijnden, J., Degenaar, N., Russell, T. D., et al. 2021, MNRAS, 507, 3899
Voges, W., Aschenbach, B., Boller, T., et al. 1999, A&A, 349, 389
Walter, R., Zurita Heras, J., Bassani, L., et al. 2006, A&A, 453, 133
Wang, W., Tong, H., & Guo, Y.-J. 2014, Research in Astronomy and Astrophysics, 14, 673
Webb, N. A., Coriat, M., Traulsen, I., et al. 2020, A&A, 641, A136
Weisskopf, M. C., Tananbaum, H. D., Van Speybroeck, L. P., & O'Dell, S. L. 2000, in Society of Photo-Optical Instrumentation Engineers (SPIE) Conference Series, Vol. 4012, X-Ray Optics, Instruments, and Missions III, ed. J. E. Truemper & B. Aschenbach, 2–16
Winkler, C., Courvoisier, T. J. L., Di Cocco, G., et al. 2003, A&A, 411, L1
Wright, E. L., Eisenhardt, P. R. M., Mainzer, A. K., et al. 2010, AJ, 140, 1868

[27] `http://astro.uni-tuebingen.de/~xrbcat/`

Appendix A: Catalogue format

Table A.1. Definition of columns in the HMXB catalogue. In total the catalogue contains **66** columns.

№	Column name	Unit	Description
1	'Name'		Object name, which is the most common name in the literature
2	'RAdeg'	deg	Right Ascension in degrees (ICRS).
3	'DEdeg'	deg	Declination in degrees (ICRS).
4	'PosErr'	arcsec	Positional error in arcseconds.
5	'Coord_Ref'		Reference of catalogue or literature, which was used to extract the coordinates and uncertainties
6	'ID_Flag'		Robust identification of the optical counterpart: 0 — solidly identified optical counterpart in the literature 1 — tentative optical counterpart identification in the literature 2 — no identified optical counterpart
7	'GLON'	deg	Galactic longitude in degrees.
8	'GLAT'	deg	Galactic latitude in degrees.
9	'Xray_Type'		List of the X-ray types assigned to the object. For more information see section above § 2.1.
10	'Porb'	day	Orbital period of the binary system in days if determined.
11	'Ppulse'	s	Pulsation period (spin) of the binary (with NS) in seconds if determined.
12	'CRSF'	keV	Cyclotron line energies in keV
13	'Alt_Name'		Second most used name in the literature.
14	'SpType'		Spectral type of the optical counterpart.
15	'Gaia_DR3_ID'		Source Name in the Gaia DR3 catalogue.
16	'Gmag'	mag	Optical magnitude in G-band according to a Gaia's catalogue.
17	'e_Gmag'	mag	Corresponding magnitude's error in G-band according to Gaia's catalogue.
18	'Vmag'	mag	Optical magnitude in V-band according to SIMBAD database.
19	'e_Vmag'	mag	Corresponding magnitude's error in V-band according to SIMBAD database.
20	'Jmag'	mag	IR magnitude in J-band according to 2MASS (Cutri et al. 2003).
21	'e_Jmag'	mag	Corresponding magnitude's error in J-band according to 2MASS (Cutri et al. 2003).
22	'Hmag'	mag	IR magnitude in H-band according to 2MASS (Cutri et al. 2003).
23	'e_Hmag'	mag	Corresponding magnitude's error in H-band according to 2MASS (Cutri et al. 2003).
24	'Kmag'	mag	IR magnitude in K-band according to 2MASS (Cutri et al. 2003).
25	'e_Kmag'	mag	Corresponding magnitude's error in K-band according to 2MASS (Cutri et al. 2003).
26	'W1mag'	mag	IR magnitude in W1 *CatWISE*2020 band (Marocco et al. 2021).
27	'e_W1mag'	mag	Corresponding magnitude's error in W1 *CatWISE*2020 band (Marocco et al. 2021).
28	'W2mag'	mag	IR magnitude in W2 *CatWISE*2020 band (Marocco et al. 2021).
29	'e_W2mag'	mag	Corresponding magnitude's error in W2 *CatWISE*2020 band (Marocco et al. 2021).
30	'N_H'	10^{21} cm^{-2}	Neutral hydrogen column density, assuming a power-law spectrum (Evans et al. 2020).
31	'XMM_min_flux'	10^{-12} erg cm^{-2} s^{-1}	Minimum X-ray flux for XMM-Newton (0.2-12.0 keV).
32	'XMM_max_flux'	10^{-12} erg cm^{-2} s^{-1}	Maximum X-ray flux for XMM-Newton (0.2-12.0 keV).
33	'Chandra_min_flux'	10^{-12} erg cm^{-2} s^{-1}	Minimum X-ray flux for Chandra ACIS (0.5-7.0 keV) or HRC (0.1-10.0 keV).
34	'Chandra_max_flux'	10^{-12} erg cm^{-2} s^{-1}	Maximum X-ray flux for Chandra ACIS (0.5-7.0 keV) or HRC (0.1-10.0 keV).
35	'Chandra_Instrument'		Chandra Instrument used for Chandra flux values.
36	'XRT_min_flux'	10^{-12} erg cm^{-2} s^{-1}	Minimum X-ray flux for Swift/XRT (0.3-10.0 keV).
37	'XRT_max_flux'	10^{-12} erg cm^{-2} s^{-1}	Maximum X-ray flux for Swift/XRT (0.3-10.0 keV).
38	'BAT_min_flux'	10^{-12} erg cm^{-2} s^{-1}	Minimum X-ray flux for Swift/BAT (14-195 keV).
39	'BAT_max_flux'	10^{-12} erg cm^{-2} s^{-1}	Maximum X-ray flux for Swift/BAT (14-195 keV).
40	'INTEGRAL_min_flux'	10^{-12} erg cm^{-2} s^{-1}	Minimum X-ray flux for INTEGRAL (17-60 keV).
41	'INTEGRAL_max_flux'	10^{-12} erg cm^{-2} s^{-1}	Maximum X-ray flux for INTEGRAL (17-60 keV).
42	'Mean_Mass'	$M_\odot$	Mean mass of the compact object.
43	'Low_Mass'	$M_\odot$	Lower limit of the compact object mass.
44	'High_Mass'	$M_\odot$	Upper limit of the compact object mass.
45	'Mean_Dist'	pc	Mean (between the two, minimum and maximum) estimate of the distance to the binary system

Table A.1 – continued

№	Column name	Unit	Description
			according to Gaia Collaboration et al. (2023); Bailer-Jones et al. (2021); Anders et al. (2022) or taken from literature. In every literature case only one source of information was taken.
46	'Low_Dist'	pc	The lowest (minimum) estimate of the distance to the binary system according to Gaia Collaboration et al. (2023); Bailer-Jones et al. (2021); Anders et al. (2022) or taken from literature. In every literature case only one source of information was taken.
47	'High_Dist'	pc	The highest (maximum) estimate of the distance to the binary system according to Gaia Collaboration et al. (2023); Bailer-Jones et al. (2021); Anders et al. (2022) or taken from literature. In every literature case only one source of information was taken.
48	'Teff'	K	Effective stellar temperature provided by Gaia Collaboration et al. (2023); Anders et al. (2022).
49	'Lopt'	$L_\odot$	Luminosity estimate of the optical companion provided by Gaia Collaboration et al. (2023).
50	'IDS'		List of all identifiers, that we found in SIMBAD and in the catalogues and articles.
51	'CRSF_Ref'		References to the articles, which providing the corresponding values for cyclotron line energies.
52	'Spin_Ref'		References to the articles, which providing the corresponding value for Pulsation Periods.
53	'Orb_Ref'		References to the articles, which providing the corresponding value for Orbital parameters.
54	'Spectral_Ref'		References to the articles, which providing the spectral type of the optical star.
55	'Dist_Ref'		Reference to the article, which provides the distance estimation, if literature values were used.
56	'Mass_Ref'		Reference to the article, which provides the mass estimation of the compact object.
57	'misc_Ref'		miscellaneous references regarding the object.
58	'comments'		Comments regarding the object.
59	'_2MASS_ID'		Source name in the 2MASS All-Sky Catalogue of Point Sources
60	'CatWISE_ID'		Source name in the CatWISE2020 catalogue
61	'ROSAT_ID'		Source name in the Second ROSAT all-sky survey (2RXS) source catalogue
62	'XMM_ID		Source name in the XMM-Newton Serendipitous Source Catalogue
63	'Chandra_ID'		Source name in the Chandra Source Catalogue (CSC) Release 2.0
64	'XRT_ID'		Source name in the 2SXPS Swift X-ray telescope point source catalogue
65	'BAT_ID'		Source name in the Swift-BAT 105-Month All-Sky Hard X-Ray Survey catalogue
66	'INTEGRAL_ID		Source name in the INTEGRAL/IBIS 9-year Galactic Hard X-Ray Survey catalogue

5 XRBcats - Low Mass X-ray Binaries

The second category mentioned earlier is the class of Low Mass X-ray Binaries (LMXBs). Similar to the HMXBs-catalogue, the idea of this paper was to provide an up-to-date catalogue of galactic LMXBs because the latest catalogue before this work was by Liu et al. (2007). This work was performed by Artur Avakyan. The code used for the HMXBs-catalogue was repurposed for the LMXBs-catalogue with minor adjustments to update information of known LMXBs, and to add newly discovered sources. The HMXBs code for the finding charts was also reused in this work. Artur Avakyan led the literature research, where I was involved in the discussion of ambiguous sources. I led the development of the website that is used to distribute the LMXBs-catalogue where, I am also in charge of maintaining and updating the website.

Astronomy & Astrophysics manuscript no. lmxbmain
July 28, 2023

XRBcats: Galactic low-mass X-ray binary catalogue ⋆

A. Avakyan[1]⋆⋆, M. Neumann[1], A. Zainab[2], V. Doroshenko[1], J. Wilms[2] and A. Santangelo[1].

[1]Universität Tübingen, Institut für Astronomie und Astrophysik Tübingen, Sand 1, 72076 Tübingen, Germany
[2]Dr. Karl-Remeis Sternwarte and Erlangen Centre for Astroparticle Physics, Friedrich-Alexander Universität Erlangen-Nürnberg, Sternwartstr. 7, 96049 Bamberg, Germany

Received 28 March 2023 / Accepted 26 May 2023

ABSTRACT

We present a new catalogue of low-mass X-ray binaries (LMXBs) in the Galaxy. The catalogue contains source names, coordinates, source types, fluxes, distances, system parameters, and other characteristic properties of 349 LMXBs, including systems that have been newly discovered or reclassified since the most recently reported LMXB catalogues. The aim of this catalogue is to provide a list of all currently known Galactic objects identified as LMXBs with some basic information on each system (including X-ray and optical/IR properties where possible). Literature published before May 2023 has been taken into account where possible when compiling this information. References for all reported properties as well as object-finding charts in several energy bands are provided as part of the catalogue. We plan to update the catalogue regularly, in particular to reflect new objects discovered in the ongoing large-scale surveys such as *Gaia* and eROSITA.

Key words. catalogs – X-rays: binaries – stars: low-mass – stars: late-type – binaries: general – X-rays: bursts

1. Introduction

X-ray binaries (XRBs) are among the brightest objects in the sky in the X-rays. They represent the endpoints of the stellar evolution of massive stars. Understanding the physical processes defining the observational appearance of individual objects and the properties of the XRB population as a whole is therefore essential for understanding massive star evolution and the evolution of the Galaxy in general. To this end, it is important to maintain an up-to-date census of known XRBs and their properties, especially in the era of the current generation of large-scale surveys such as the extended ROentgen Survey Imaging Telescope Array (eROSITA, Merloni et al. 2012; Predehl et al. 2021) on board SRG, *Gaia* (Gaia Collaboration et al. 2016, 2023) and the Wide-field Infrared Survey Explorer (WISE, Wright et al. 2010; Cutri et al. 2021), which are able to unveil ever fainter objects.

However, the identification of XRBs among millions of other objects requires up-to-date knowledge of the properties and locations of already known sources, and the large-scale surveys mentioned above are providing vast amounts of new observational data for these objects. The compilation of such an updated database is the primary goal of this work, although many other uses can of course also be envisaged.

The main source of high-energy radiation in XRBs is the accretion of matter onto either a neutron star (NS) or a black hole (BH) from a companion star. The observed properties of XRBs are largely defined by the mass-transfer mechanism powering the accretion, which can occur either directly from the wind of a secondary or via Roche lobe overflow (RLOF), which primarily depends on the mass ratio between the compact object and the optical counterpart (M_x/M_{opt}). Based on this ratio, XRBs are subdivided into two large groups: high- and low-mass X-ray binaries (HMXBs and LMXBs, respectively). For objects with $M_x > M_{opt}; M_{opt} \lesssim 1M_\odot$, the mass is usually transferred to the compact object via RLOF. Such objects are classified as LMXBs. Those with $M_x < M_{opt}; M_{opt} \gtrsim 5M_\odot$ typically accrete directly from the stellar wind and are classified as HMXBs. The rather dramatic differences in the observed properties of LMXBs and HMXBs warrant the treatment of each subclass separately. Here, we focus on the properties of LMXBs. In turn, updated catalogues of HMXBs are presented by Neumann et al. 2023 and Fortin et al. (2023)[1,2].

As follows from the definition of an LMXB, the donor is (in most cases) a late-spectral-type star filling its Roche lobe. However, A-type stars, F-G-type subgiants, or even white dwarfs (WDs) can also act as donors in LMXBs. The optical properties of LMXBs can also be affected by emission from the accretion disc around the compact object, where the disc can be heated by itself or illuminated by X-ray emission from the compact object. Nevertheless, LMXBs are generally intrinsically faint objects in the optical and IR bands. The main way to analyse features of known LMXBs in detail or to detect new ones is to observe them during outbursts (Lasota 2016). New sources continue to be discovered in this way, and the population of known LMXBs is ever growing.

The latest catalogue of Galactic LMXBs, which was published by Liu et al. (2007), is now nearly 16 years old. Since that time, many new transient and persistent objects have been discovered. Some LMXB candidates have been reclassified, while other sources have gained LMXB status. Moreover, missions such as the X-ray Multi-Mirror Mission (*XMM-Newton*, Jansen

⋆ The catalogue is available at the CDS via anonymous ftp to cdsarc.cds.unistra.fr (130.79.128.5) or via https://cdsarc.cds.unistra.fr/viz-bin/cat/J/A+A/675/A199, and the catalogue table, along with the corresponding finding charts and other useful information is also publicly accessible at http://astro.uni-tuebingen.de/~xrbcat.

⋆⋆ E-mail: artur.avakyan@astro.uni-tuebingen.de

[1] https://vizier.cds.unistra.fr/viz-bin/VizieR?-source=J/A+A/671/A149

[2] https://binary-revolution.github.io/HMXBwebcat

et al. 2001), the INTErnational Gamma-Ray Astrophysics Laboratory (INTEGRAL, Winkler et al. 1993), and *Gaia* have resulted in a quantitative and qualitative improvement in our knowledge of XRB properties. In this context, we have compiled a revised catalogue of the Galactic LMXBs that incorporates multi-wavelength information and encompasses the inclusion of new sources identified since the publications of Liu et al. (2007) and Ritter & Kolb 2003 (Liu07 and RK03 hereinafter). Our final catalogue contains 349 LMXBs and candidates, of which 204 were contained in the two catalogues mentioned above (the content of Liu07 and RK03 overlaps but neither includes the other completely). That is, the new catalogue presented here represents a more than 71% increase in volume with respect to the two most extensive catalogues of the past. We aim to compile a comprehensive and up-to-date database containing information such as optical/IR magnitudes, X-ray fluxes, distances, and so on, for the current catalogue, which will hopefully help to facilitate the identification of new LMXBs in current and future X-ray surveys, as well as population studies.

The structure of the paper is as follows: in Sect. 2, we describe how the LMXB sample was compiled and list data sources used to provide extra information on known objects. In the same section, we list relevant X-ray and optical properties, and characterise methods used for identification of known and candidate optical/IR counterparts in large-scale surveys. In Sect. 3, a description of the table fields and finding charts is provided, as well as a comparison of our catalogue with works of RK03 and Liu07. Finally, we summarise our results in Sect. 4. One can also find a list of identified archive optical/IR counterparts for some LMXBs based on the literature in Appendix A. A description of the columns of the catalogue table is presented in Appendix B.

2. Definition of the sample and data sources

The bulk of the objects in the catalogue consists of LMXBs reported by the catalogues of RK03 and Liu07, and so we started our compilation of the sample by merging these two catalogues. During this process, a number of duplicate objects both within and across the two catalogues were identified and removed from the sample. In addition, several sources in RK03 and Liu07 were found to be extragalactic (in some cases, this possibility was already indicated in the original catalogues and sometimes reported in the literature afterwards). Such objects were also excluded from our final list. The same applies to the satellite galaxies of the Milky Way. To this end, the two LMXBs known to be located in the Large Magellanic Cloud (LMC), namely, LMC X−2 and RX J0532.7−6926 (which were included in both RK03 and Liu07) are not listed in our catalogue. All objects that were removed, as well as other problematic cases, are listed and described in detail in Sect. 3.2.

In addition to Liu07 and RK03, we also considered all Galactic objects classified as possible LMXBs in the SIMBAD[3] and VizieR[4] databases hosted by the Centre de Données astronomiques de Strasbourg (CDS) databases. We include these objects in the catalogue, giving appropriate references for classification. We conducted a thorough literature search (including Astronomer's Telegrams[5]) to identify any newly discovered LMXBs. Most of the new LMXBs reported in the literature between 2006 and 2020 were discovered by the INTEGRAL (Winkler et al. 2003), the Monitor of All-sky X-ray Image (MAXI, Matsuoka et al. 2009), *Swift* (Gehrels et al. 2004), or *Gaia* (Gaia Collaboration et al. 2016) missions, as summarised by Bahramian & Degenaar (2023). The latter publication can therefore also be considered as another major data source used in this work. In addition, the catalogue of Galactic LMXBs detected by INTEGRAL (Sazonov et al. 2020) also proved to be a valuable resource for expanding our list of LMXBs. Finally, we used the recently published catalogue of ultracompact X-ray binaries (UCXBs) made by Armas Padilla et al. 2023[6] to cross-check the completeness of our sample in the context of UCXBs (no missing sources were found). It should be noted that although efforts have been made to find all LMXBs identified to date, it is possible that some may have been missed. Therefore, we kindly ask readers to report any omissions found, so that those can be included in updated versions of the catalogue.

We note that systems in which a WD acts as an accretor are not generally considered as XRBs for historical reasons (despite the fact that they also emit in the X-ray band), and so those systems (namely cataclysmic variables or CVs) are not included in the current catalogue. We also do not include rotation-powered pulsars, even if they are members of binary systems and emit in X-rays, unless the observed emission is accretion powered; that is, 'spider'-type pulsars including Black Widows (BWs) and Redbacks (RBs; see e.g. Chen et al. 2013; Roberts 2013) are omitted unless they are also classified as transitional millisecond pulsars (tMSP; see e.g. Archibald et al. 2009; Papitto et al. 2013; Knight et al. 2023). All tMSPs and their candidates included in the catalogue are listed in Table 1 in Sect. 3.2.

The mass ranges quoted in Sect. 1 for XRBs are of course approximate, and there are some boundary cases, such as Her X−1, where accretion to a NS occurs via the RLOF of a B3 type $\sim 2.2 M_{\odot}$ donor (Tananbaum et al. 1972; Middleditch & Nelson 1976). This system is most often classified in the literature as an intermediate mass X-ray binary (IMXB) rather than as an LMXB because the NS appears as an X-ray pulsar and is therefore strongly magnetised, which is not typical for NS LMXBs. As the total number of IMXBs is relatively small, and despite the additional fact that they 'bridge' the HMXB and LMXB classes, they are evolutionarily closer to LMXBs as binary systems, and so we opt to include them as a part of the current LMXB catalogue. This decision is also clearly communicated in the publication describing the HMXB catalogue released in parallel to the current work (Neumann et al. 2023) in order to avoid any confusion or source duplication, except for one specific case (Cir X−1), which is described in Sect. 3.2.

2.1. Main properties and features

In order to reflect the huge variety of LMXB properties, we incorporate all accessible and relevant information concerning the donor star and compact object, including data on their properties, variability, and other pertinent details. Besides the quantitative properties (such as positions, fluxes in various bands, orbital or spin periods, and so on), some of these properties or features can be incorporated as a set of flags defined to characterise several LMXB subclasses, as was already done by Liu07 and RK03. Here, we extend the classification adopted by these authors to account for extra features added to the current catalogue. In order to provide a broad overview of the Galactic LMXB properties, we also show the frequency of the occurrence of the individual type flags in graphical format in Fig. 1. It is important to note

[3] http://simbad.cds.unistra.fr/simbad
[4] https://vizier.cds.unistra.fr/viz-bin/VizieR
[5] https://astronomerstelegram.org
[6] https://research.iac.es/proyecto/compactos/UltraCompCAT

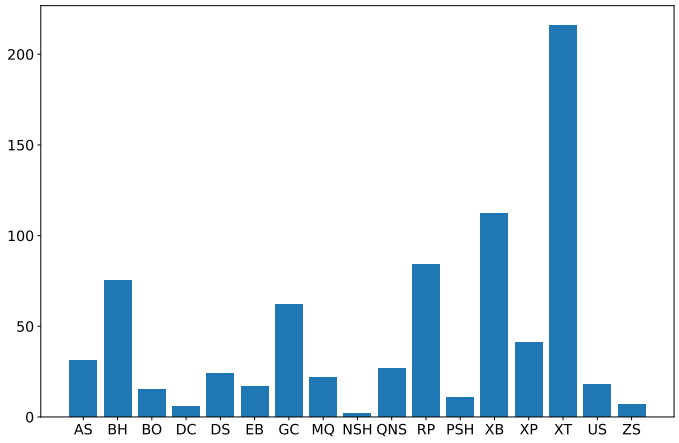

Fig. 1. Population of LMXBs of each type in the Galaxy.

that these flags are not intended to serve as a basis for systematic classification, but rather to reflect the characteristics of individual systems to ease the selection of objects exhibiting specific observational features. Each source in the catalogue may therefore have one or more of the following flags, which are listed alphabetically:

1. AS: Atoll X-ray binary hosting a weakly magnetised NS as a main component. The spectrum is soft and no significant pulsations are present. The majority of the points on the colour–colour diagrams ('hard' versus 'soft') from atoll sources usually form a band at constant hard colour.
2. BH: System contains a black hole candidate.
3. BO: X-ray burster (see XB definition below) with coherent burst oscillations at the NS spin period.
4. DC: System with an accretion disc corona.
5. DS: 'Dipping' source. System shows periodic but irregular dips in the X-ray intensity, which are generally connected with the partial obscuration of the NS by a thickened region of the accretion disc.
6. EB: Eclipsing or partially eclipsing binary system.
7. GC: Source within a globular cluster.
8. MQ: Microquasar, a source with reported evidence for relativistic jets.
9. NSH: Negative (nodal) superhumps are present in the system. These negative superhumps are periodic optical signals, the periods of which are smaller than the orbital period of the binary.
10. QNS: Quiescent NS.
11. RP: Compact object acts as a radio pulsar.
12. PSH: Positive superhumps (permanent or transient) present in the system. The same as the NSH type (see above), but the time period of the signal is larger than the orbital one.
13. XB: X-ray burst source. This type collects X-ray binary systems with a NS, which exhibit thermonuclear (type-I) X-ray bursts.
14. XP: Compact object in the binary acts as an X-ray pulsar.
15. XT: Transient X-ray source. System shows dramatic changes in luminosity (mostly in the X-ray band). Energy is produced by means of a non-stationary accretion process.
16. US: Ultrasoft X-ray spectrum. In some catalogues, this type is denoted 'super soft'. These binaries also include some 'extreme ultrasoft' (EUS) sources.
17. ZS: Z-type source. This type of X-ray binary is similar to the atoll type (also contains weakly magnetised NS), but the plot on the colour–colour diagram is different (Z-letter shape).

We note that the 'XB' (X-ray burster) flag — originally introduced by RK03 — in our catalogue specifically refers to thermonuclear (type-I) bursts only. Type-II X-ray bursts likely caused by instabilities in the accretion flow are relatively rare, and to the best of our knowledge have only been detected from two LMXBs: MXB 1730−335 ('rapid burster'; Bagnoli et al. 2015) and GRO J1744−28 ('bursting pulsar'; Court et al. 2018), and one HMXB: SMC X−1 (Rai et al. 2018), and are therefore not flagged separately. The MXB 1730−335 is known to exhibit bursts of both types, and is therefore still flagged. On the other hand, type-I bursts have been suggested to be present but have never been unambiguously detected from the bursting pulsar (Giles et al. 1996; Lamb et al. 1996; Doroshenko et al. 2015), and so this source is not flagged.

2.2. X-ray properties

Considering that X-ray emission dominates the bolometric luminosity of XRBs, one of their main characteristics is their X-ray flux and spectrum. In our catalogue, we therefore tried to compile information on X-ray fluxes in soft and hard X-ray bands for all LMXBs in a uniform way. For the soft X-ray band, we report fluxes observed by *XMM-Newton*[7] (Schartel et al. 2022; Webb et al. 2020), the *Chandra* X-ray Observatory[8] (CXO, Weisskopf et al. 2000; Evans et al. 2010), and *Swift*/XRT[9] (Burrows et al. 2005; Evans et al. 2020) throughout their lifetime. In particular, we report the 0.2–12 keV energy band flux (equivalent to the EPIC_8 band used in *XMM-Newton* catalogues) and/or the X-ray flux in similar energy bands of CXO and *Swift*/XRT, that is, the 0.3–10 keV observed flux for *Swift*/XRT, and either the broad ACIS band (0.5–7.0 keV) or the wide HRC band (0.1–10.0 keV) for CXO. We note that although the difference in energy bands for various instruments might result in a factor of ∼1.5 difference for a given source, here we only report the range of fluxes detected over a long period. This range is therefore dominated by intrinsic variability and differences in source spectra, and so the difference in energy range between the various instruments is not really relevant to our purposes. In the hard X-ray band, fluxes from INTEGRAL[10] (Krivonos et al. 2012) and *Swift*/BAT[11] (Oh et al. 2018; Barthelmy 2004) are reported. Here, we report fluxes in the energy range of 14-145 keV for *Swift*/BAT and in the energy range of 17–60 keV for INTEGRAL. We note that these bands are largely equivalent as the flux above 60 keV is comparatively small for most sources, and the variability argument still applies.

Another key property provided by X-ray observations is the localisation that is essential to identify or assess the reliability of the identified optical counterparts. We therefore also include information on the most accurate X-ray position available either from the literature or directly from soft (*Chandra*, *XMM-Newton* or *Swift*/XRT) and hard (INTEGRAL, *Swift*/BAT) catalogues as described in the following section.

[7] https://heasarc.gsfc.nasa.gov/W3Browse/xmm-newton/xmmssc.html
[8] https://vizier.cds.unistra.fr/viz-bin/VizieR-3?-source=IX/57/csc2master
[9] https://vizier.cds.unistra.fr/viz-bin/VizieR-3?-source=IX/58/2sxps
[10] https://vizier.cds.unistra.fr/viz-bin/VizieR-3?-source=J/A%2bA/545/A27
[11] https://heasarc.gsfc.nasa.gov/W3Browse/swift/swbat105m.html

2.3. Astrometry and identification of the optical counterparts

Considering that the properties of XRBs are largely defined by the properties of the donor star, the identification of the optical counterparts and the characterisation of their multi-wavelength properties are essential. Some of the LMXBs in the sample already have robustly identified optical counterparts; however, the optical positions (as well as other optical data) reported in Liu07 and RK03 are in many cases outdated, and lack accuracy by current standards. We therefore attempted to improve position accuracy using the latest astrometry data from *Gaia* DR2[12], eDR3[13], DR3[14] (Gaia Collaboration et al. 2018, 2021, 2023), Two Micron All Sky Survey[15] (2MASS, Skrutskie et al. 2006; Cutri et al. 2003b,a) and the mid-IR CatWISE2020 catalogue[16] (Marocco et al. 2021).

We started the process of identifying counterparts in these catalogues by verifying whether the SIMBAD database already had any pre-existing matches with *Gaia* DR3 (eDR3, DR2), 2MASS, and/or WISE and checking their correctness manually. It should be noted that in some cases, the associations provided by SIMBAD were indeed incorrect, and we list such cases in Sect. 3.2. In cases where no SIMBAD optical/IR identifiers were provided, we attempted to find counterparts reported in the literature. In some cases where precise optical, IR, or radio coordinates were available, these coordinates were used to find the corresponding counterparts in *Gaia* DR3, 2MASS, and CatWISE2020. All solid cross-matches and relevant data were added to the catalogue. In particular, identifications by Arnason et al. (2021) proved to be useful, and so these are considered as the main references for the cases marked in Table A.1 in Appendix A. This table lists all sources for which optical/IR counterparts are available, except those correctly listed in SIMBAD.

As mentioned above, some LMXBs have been classified as such only based on their X-ray properties, and have no uniquely identified optical counterparts in the literature. In most cases, these are relatively poorly studied sources (sometimes only detected once with X-ray monitors during an outburst). However, in some cases, accurate X-ray positions obtained at a later time are available. For those objects, we used CXO, *XMM-Newton*, or *Swift*/XRT positions (in order of preference). The search radius was set to match the full positional uncertainty (i.e. statistical plus systematic) reported in the respective X-ray catalogue. The final identification of plausible optical counterparts was done manually by inspection of the finding charts also released as part of the current catalogues and by searching for tentative counterparts in the literature based on their properties. In all cases where it was possible to identify a plausible counterpart, we list it as such; however, the optical position is only assigned as primary if a unique counterpart is identified.

2.4. Additional information

For all optical counterparts identified as described above, we include information on IR and/or optical magnitudes wherever possible. In particular, we include *Gaia* G-band or V-band magnitudes in the optical band, near-IR photometry either from 2MASS or Visible and Infrared Survey Telescope for Astronomy (VISTA, Emerson et al. 2006; Dalton et al. 2006) Variables in the Via Lactea (VVV) DR4 catalogue (VVV[17], Minniti et al. 2010) surveys, or from the literature. Finally, we also include magnitudes in the W1 and W2 bands reported in the CatWISE2020, AllWISE, or WISE (in that order of preference) catalogues (Marocco et al. 2021; Cutri et al. 2021; Wright et al. 2010). In all cases, we provide the references to the sources where the V-band, G-band, JHK, and WISE magnitudes were taken from and show them in 'Vmag_Ref', 'Gmag_Ref', 'JHK_Ref', and 'WISE_Ref' columns, respectively. It should be noted that we mainly tried to include the optical/IR magnitudes during the quiescent state of the corresponding binary (to represent the LMXB population in the state in which it is found most of the time). However, in some cases, 'quiescent' magnitudes were not available, and so we list magnitudes during the outburst, if any.

Besides more accurate positions and photometry, we also include some additional information unavailable at the time of publication of Liu07 and RK03. For all LMXBs for which a *Gaia* counterpart was ultimately identified, we provide distance estimates from *Gaia* DR3, those based on *Gaia* eDR3[18] (Bailer-Jones et al. 2021) or *Gaia* DR2[19] (Bailer-Jones et al. 2018), and estimations from StarHorse1[20]/2[21](Anders et al. 2019, 2022). In addition, we manually searched the literature for any distance estimations, especially in cases where *Gaia*/StarHorse data were unavailable.

We were also interested in the spectral type of the optical counterpart, and we therefore attempted to include this information based on either *Gaia* DR3, SIMBAD, or the literature search. We note that the list of X-ray pulsars maintained by Mauro Orlandini[22] was found to be a useful resource in this regard (and also for reported spin and orbital periods) and we would like to acknowledge it here. For sources where the reported spectral type and corresponding reference were published before 2007, the spectral information in RK03 or Liu07 was used.

Finally, for convenience, we also provide the X-ray absorption neutral hydrogen column density ($N_{\rm H}$) estimates, which might be relevant to estimate some additional LXMB properties such as X-ray to optical luminosity ratios in order to facilitate searches for new LMXBs with similar properties. We report values based either on *Swift*/XRT data (Evans et al. 2020) or on results reported in the literature (all references are listed). In cases where one of the two ($N_{\rm H}$ or $A_{\rm G}$) was unknown, we calculated the other one through the $N_{\rm H}(A_{\rm G})$ relation reported by Foight et al. (2016).

[12] https://vizier.cds.unistra.fr/viz-bin/VizieR?-source=I/345
[13] https://vizier.cds.unistra.fr/viz-bin/VizieR-3?-source=I/350/gaiaedr3
[14] https://vizier.cds.unistra.fr/viz-bin/VizieR-3?-source=I/355
[15] https://vizier.cds.unistra.fr/viz-bin/VizieR?-source=II/246
[16] https://vizier.cds.unistra.fr/viz-bin/VizieR?-source=II/365
[17] http://vvvsurvey.org
[18] https://vizier.cds.unistra.fr/viz-bin/VizieR-3?-source=I/352
[19] https://vizier.cds.unistra.fr/viz-bin/VizieR-3?-source=I/347
[20] https://vizier.cds.unistra.fr/viz-bin/VizieR-3?-source=I/349/starhorse
[21] https://vizier.cds.unistra.fr/viz-bin/VizieR-3?-source=I/354/starhorse2021
[22] http://www.iasfbo.inaf.it/~mauro/pulsar_list.html

3. Catalogue content and quality assurance

3.1. Description of the fields

There are 349 entries in the catalogue, each of which corresponds to a single Galactic source. The objects are sorted by right ascension (the second column) in increasing order. There are a total of 62 columns listing various parameters and corresponding references. The content and format of individual columns is described in detail in Table B.1 in Appendix B.

3.2. Finding charts and problematic cases

We provide finding charts for all sources in our catalogue, which includes up to six different images, covering bands from mid-IR to hard X-rays. Corresponding charts can be found on a dedicated website[23] or obtained via CDS system[24]. The top row of each finding chart includes images from the VVV DR4 catalogue[25] (Minniti et al. 2010) or 2MASS[26] (left, in order of preference), an image of unWISE[27] (Schlafly et al. 2019) (middle), and an RGB-image of either *Chandra*[28], *XMM-Newton*[29], or the Roentgensatellit (ROSAT[30], Truemper 1982; Boller et al. 2016; Voges et al. 1999) (right, in order of preference).

The bottom row includes the soft X-ray image of *Swift*/XRT (SwiftXRTInt in astroquery.skyview) in the left corner, and hard X-ray images from *Swift*/BAT[31] and INTEGRAL[32] in the middle and right corners, respectively. The field of view for VVV, 2MASS, unWISE, *XMM-Newton*, and *Chandra* images was set at 1 arcmin, while for *Swift*/XRT and ROSAT it was set at 5 arcmin and 15 arcmin, respectively. The field of view for *Swift*/BAT and INTEGRAL was chosen to be 10°, with the size of the region chosen based on the field of view and angular resolution of the given instrument.

Each panel of the finding chart includes the coordinates and uncertainties of all detected sources within the respective regions, with position uncertainties represented by error circles. A red cross indicates the position listed in SIMBAD for the source, while a dark-blue diamond represents the coordinates described in the literature (Liu07 or RK03). The position used for this catalogue is indicated with an orange star. In the case of soft X-ray instruments, observation positions are indicated by error circles to prevent overcrowding. A golden circle indicates the *Chandra* position, a red circle indicates the *XMM-Newton* position, a green circle indicates the *Swift*/XRT position, and a navy-blue circle indicates the ROSAT position. *Swift*/BAT and INTEGRAL are indicated as a deep-pink pentagon and a lime-green triangle, respectively. In the optical band, we indicate CatWISE2020 with an orange 'X', 2MASS with a cyan '+', and *Gaia* DR3 data with a purple square. From a technical perspective, we used the Hierarchical Progressive Surveys (HiPS) data from Fernique et al. 2015, using SkyView Query only for *Swift*/XRT to obtain images. Both services were queried using `astroquery.hips2fits`[33], and `astroquery.skyview`[34] modules.

As an example, the finding chart of GRO J1744−28 can be seen in Fig. 2. We also note that imaging in more bands with a catalogue overlay is available via the Aladin lite interface (Baumann et al. 2022) on the website hosting the catalogue[35].

Based on the literature search and inspection of the finding charts described above, we identified several problematic cases:

- The X-ray source SAX J0840.7+2248, which is classified as a LMXB in Liu07, is excluded from our catalogue. This transient is more likely to be the X-ray-rich gamma-ray burst GRB980429 rather than an XRB (Sidoli et al. 2007).
- SWIFT J0732.6−1330, which is listed as a LMXB in SIMBAD, is also not presented in our catalogue due to the fact that the source is an intermediate polar (accreting magnetised white dwarf, IP) (Butters et al. 2007).
- Peng & Shen (2021) find the LMXB candidate OGLE BLG511.6 25872 to be of the same polar nature. We therefore do not include it in our catalogue.
- The X-ray transient Swift J061223.0+701243(.9), listed as LMXB in Liu07, could also be an IP (Butters et al. 2011). In this case, the authors suggest that an LMXB nature cannot be ruled out, and so the source can still be found in our catalogue; however, we urge caution when considering the classification of this source.
- 2E 1613.5−5053 (listed as 1E 161348−5055.1 in Liu07 LMXB catalogue) is an X-ray source located close to the centre of the supernova remnant RCW 103. Based on XMM observations, it was discovered that the source has a 6.67 h periodicity, which may originate from either an orbital period of a LMXB or a spin period of an isolated neutron star (INS) (De Luca et al. 2006). After some time of searching for an optical/IR counterpart to confirm or refute a binary nature origin, Tendulkar et al. (2017) finally reported the detection of an IR counterpart, the properties of which clearly indicate that the IR emission was coming from an INS, ruling out an LMXB origin scenario.
- V* V934 Cen, another SIMBAD LMXB, seems to possess no XRB characteristics (the corresponding link in SIMBAD for the suggested LMXB type does not provide any data regarding the source), and so it is excluded from our catalogue as well.
- The same also goes for the binary TWA 22 (TWA 22AB), which is considered to be a LMXB in the SIMBAD database. SIMBAD refers to Bonnefoy et al. (2009) as the source of the corresponding classification. However, these authors estimated the total mass of the binary to be about a $220 M_{\rm Jup}$, which is far too low for the XRB. Although the system emits X-rays via coronal activity (Stelzer et al. 2022), it cannot be classified as an XRB.
- 4U 1745−203 (H 1745−203) is a transient that was considered to be a separate LMXB, but the source appears to simply be a counterpart of SAX J1748.9−2021 (NGC 6440 CX1), which has already been noted in Liu07.
- The same goes for bursting source MXB 1742−29. Following Martí et al. (2007), we consider it to be the counterpart of LMXB 1A 1742−294.

[23] http://astro.uni-tuebingen.de/~xrbcat
[24] https://cdsarc.cds.unistra.fr/viz-bin/cat/J/A+A/675/A199
[25] http://alasky.cds.unistra.fr/VISTA/VVV_DR4/VISTA-VVV-DR4-J
[26] http://alasky.cds.unistra.fr/2MASS/J
[27] http://alasky.cds.unistra.fr/unWISE/W1
[28] https://cdaftp.cfa.harvard.edu/cxc-hips
[29] http://skies.esac.esa.int/XMM-Newton/EPIC-RGB
[30] http://alasky.cds.unistra.fr/RASS
[31] http://cade.irap.omp.eu/documents/Ancillary/4Aladin/BAT_14_20
[32] http://cade.irap.omp.eu/documents/Ancillary/4Aladin/INTEGRAL_17_60
[33] https://astroquery.readthedocs.io/en/latest/hips2fits/hips2fits.html
[34] https://astroquery.readthedocs.io/en/latest/skyview/skyview.html
[35] http://astro.uni-tuebingen.de/~xrbcat

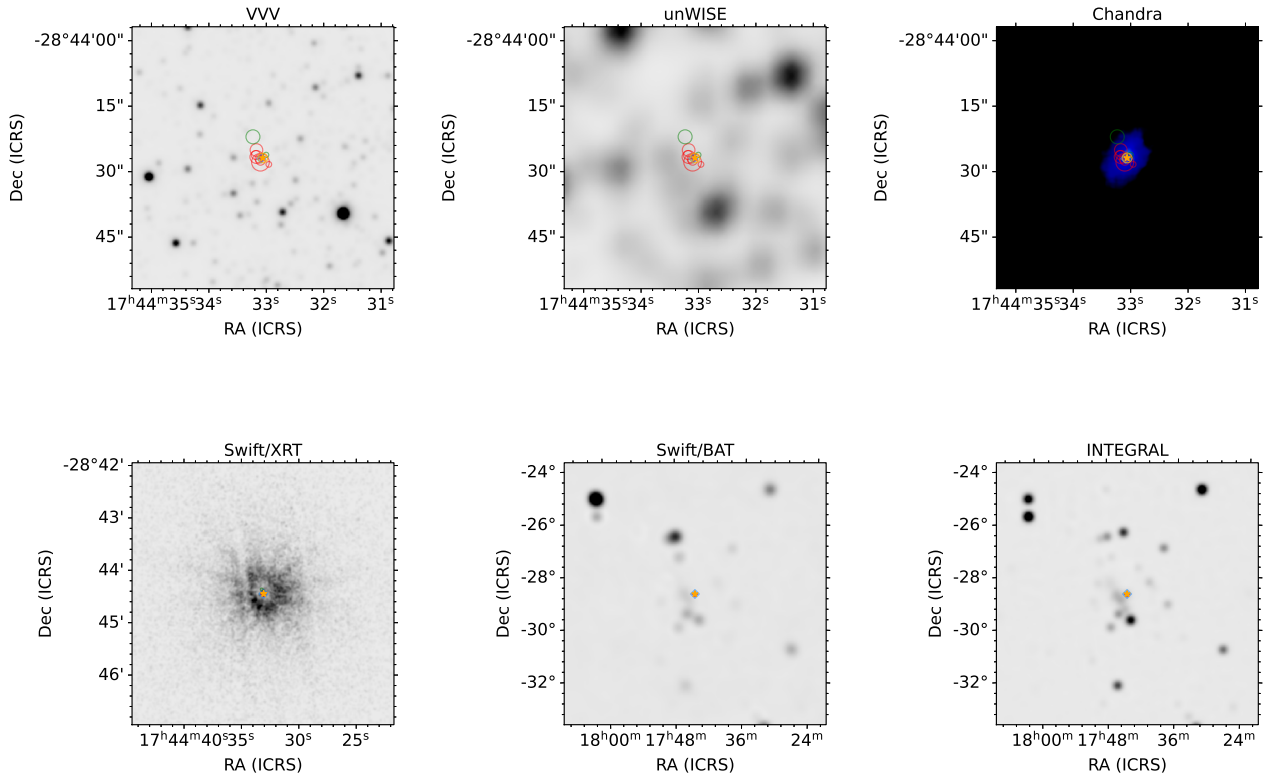

Fig. 2. Finding chart of GRO J1744−28. The finding charts display markers and error circles representing observations made by different instruments. The error circles are used for soft X-ray observations to prevent overcrowding, with a yellow circle indicating *Chandra* and a green circle representing *Swift*/XRT. The red cross and the blue diamond indicate the positions reported by SIMBAD and that found in the literature (Liu07 or RK03), respectively. An orange star denotes the position of the LMXB used in this catalogue.

- AX J1620.1−5002 is also an X-ray transient, which for a long time was considered to be a separate XRB, but it is now strongly associated with the bursting transient LMXB MAXI J1621−501 (Chenevez et al. 2018; Gorgone et al. 2018).
- 4U 0614+09 (4U 0614+091) is an UCXB with an uncertain orbital period, which is only constrained to be greater that 1 h (Baglio et al. 2014). However, following Liu07 and RK03 in the catalogue, we provide a value of 51.3 min based on Shahbaz et al. (2008).
- The nature of IGR J17404−3655 is not well constrained, because it is unclear whether the source is a LMXB or a HMXB, and is potentially a BeXRB (Coleiro et al. 2013). However, Fortin et al. (2018) used K-band spectroscopy for the source, and revealed that the object is more likely to be a CV with a K3–5V donor star. Consequently, we made the decision to not include it.
- CXOGBS J174623.5−310550 is an accreting binary, and is presented in our catalogue. However, its exact classification, that is, as either LMXB or CV, is still unknown (Torres et al. 2019).
- 1RXS J180431.1−273932 was at first considered a symbiotic LMXB system (Nucita et al. 2007) hosting a NS with a M5 III donor star. However, based on optical observations, Masetti et al. (2012) excluded a possible symbiotic LMXB nature and identified the source as a magnetic CV. Therefore, despite the fact that 1RXS J180431.1−273932 is listed as a symbiotic X-ray binary in Kuranov & Postnov (2015), we do not include it.
- Based on IR observations of 4U 1556−60 made by Revnivtsev et al. (2013), we associated an optical counterpart to this source, namely *Gaia* DR3 5833042299288099O7 (see Table A.1), which lies well inside the position error circle of 0.″3. However, according to the provided parallax, the distance to this source should not exceed 1kpc (Bailer-Jones et al. 2021), which is 3–4 times less than the distance estimations to 4U 1556−60 (Christian & Swank 1997; Grimm et al. 2002). We decided to leave this association with the *Gaia* DR3 source, but this discrepancy should be borne in mind.
- For the source IGR J17597−2201, Walter et al. (2006) proposed 2MASS J17594556−2201435 as a potential counterpart. However, based on Very Large Telescope (VLT) observations conducted by Fortin et al. (2018), we can exclude this possibility.
- The persistent X-ray-bright LMXB 4U 1624−49 seems to have incorrect coordinates and optical/IR associations in the SIMBAD database. The source was localised by *Chandra* with 0.″6 uncertainty at the position $\alpha_{J2000.0}$ = $16^{h}28^{m}02\overset{s}{.}825$, $\delta_{J2000.0}$ = −49°11′54.″61 (Wachter et al. 2005), which corresponds to the known XMM source 2XMM J162802.8−491154, which is located ≈ 53″ away from the position of 4U 1624−49 in SIMBAD. In our table, we provide the *Chandra* coordinates and uncertainty, as well as the K-band data obtained by Wachter et al. (2005). In the corresponding *Chandra* error circle, there are no *Gaia*, 2MASS, or CatWISE2020 sources. We also label 2XMM J162802.8−491154 as an alternative name for 4U 1624−49 due to the fact that this name is not listed as an identifier for this source in any other databases to the best of our knowledge.
- There is also an incorrect SIMBAD association with optical/IR archives for the LMXB GX 5−1 (4U 1758−25). At the

position provided by SIMBAD, there is a bright star located ≈ 200 pc away (Gaia Collaboration et al. 2023), a distance which is totally inconsistent with distance estimations for GX 5−1 (4.2–5.6 kpc, according to Clark 2018). Jonker et al. (2000) found an IR counterpart of the X-ray source at the position $\alpha_{J2000.0} = 18^h01^m08\overset{s}{.}222$, $\delta_{J2000.0} = -25°04'42\overset{''}{.}46$ with $0\overset{''}{.}35$ uncertainty, leading to it being located ≈ 20″ away from the position of GX 5−1 in SIMBAD. As in the case of 4U 1624−49, there are no *Gaia*, 2MASS, or CatWISE2020 counterparts. However, in the error circle, we find a VVV source, for which the JHK magnitudes are provided in the table.

– We also decided to add the object named AX J1659.0−4208 as a LMXB in our catalogue. The source was detected during the Advanced Satellite for Cosmology and Astrophysics (ASCA) Galactic plane survey (Sugizaki et al. 2001). At the time, the X-ray flux of the source was at the level of 6×10^{-12} erg/s/cm^2 (0.7 − 10 keV), but its coordinates were not well constrained. Its accurate position was then derived by Chandra, which led to identification of a near-IR counterpart by Revnivtsev et al. (2013). These latter authors suggested that the source is likely to be a symbiotic LMXB or a CV. However, based on high extinction towards this area, and distance estimations of about 5-10 kpc (Revnivtsev et al. 2013), unabsorbed X-ray luminosity can be estimated to be 10^{34} erg s^{-1} at the very least (most likely even 10^{35}erg s^{-1}), which is significantly greater than expected for a typical CV. We therefore suggest that the source is very likely to be a LMXB and it is added to our catalogue table.
– We add an X-ray source IGR J19308+0530, which seems to be an IMXB hosting an NS and s F4V-type donor star (Fortin et al. 2018). At first it was not clear whether the object is a CV or a L/IMXB (Ratti et al. 2013), and even the SIMBAD database presents the source as a CV. However, based on the spectral analysis (Ratti et al. 2010) and K-band spectroscopy (Fortin et al. 2018), we suggest that IGR J19308+0530 is most likely not a CV but an IMXB. It should also be noted that the star TYC 486−295−1 is a counterpart of IGR J19308+0530 (Rodriguez et al. 2008; Ratti et al. 2010), but it is considered to be a separate source (also a CV type instead of XRB) by SIMBAD, ≈ 88″ away from the INTEGRAL position for IGR J19308+0530 listed in SIMBAD.
– The source LMXB 4U 1728−34 was given an orbital period of ∼ 11 min (Galloway et al. 2010), and this value is also given for the binary in RK03. However, in an analysis of other X-ray observations, no further evidence was found for a periodic signal at 11 min. Subsequently, based on an analysis of its type-I X-ray burst, Vincentelli et al. (2020) stated that the orbital period should be much higher, probably ∼ 66 min or even ≳ 2 hr. In our catalogue, the value of 66 min is quoted, but readers should be aware of the lack of robust confirmation.
– The X-ray source J2039−5617 (listed as [SMD2015] 3 in SIMBAD) is presented in the RK03 catalogue as a LMXB. However, due to a likely association with the known RB source 1FGL J2039.4−5621 (Salvetti et al. 2015), it is excluded from our catalogue.
– XB 1832−330 is a globular cluster LMXB (in NGC 6652) that was tentatively assigned a 43.6 min orbital period (Deutsch et al. 2000). However, Engel et al. (2012) argue that the 43.6 min candidate period is probably spurious and suggest a longer period (by a factor 3) of about 2.15 hr (this value is quoted in our catalogue).

Table 1. tMSP candidates presented in our catalogue.

Source Name	References
1FGL J1417.7−4407 (J1417−4402 in RK03)	[1]
CXOGlb J183544.5−325939 (NGC 6652B)	[2]
4FGL J0427.8−6704	[3], [4]
4FGL J0407.7−5702	[5]
CXOGlb J174804.5−244641 (Terzan 5 CX1)	[6]
CXOU J110926.4−650224	[7], [8]
3FGL J1544.6−1125	[9], [10], [11]
4FGL J0540.0−7552	[12]
RX J1739.4−2942 (GRS 1736−297)	[13]

Notes. Along with the candidates, all three confirmed tMSPs: XSS J12270−4859, IGR J18245−2452 and PSR J1023+0038 are also included in the catalogue.
References. [1] Swihart et al. (2018), [2] Paduano et al. (2021), [3] Kennedy et al. (2020), [4] Li et al. (2020), [5] Miller et al. (2020), [6] Bahramian et al. (2018), [7] Coti Zelati et al. (2019), [8] Coti Zelati et al. (2021), [9] Bogdanov & Halpern (2015), [10] Britt et al. (2017), [11] Jaodand et al. (2021), [12] Strader et al. (2021), [13] Tetarenko et al. (2016).

– There is uncertainty over the orbital period of the tMSP candidate 4FGL J0540.0−7552. Strader et al. (2021) identified a consistent periodic signal at 2.7 h in their photometry. However, this signal could represent either the orbital period, half the orbital period (if due to ellipsoidal variations), or could even be spurious. We decided to keep the 2.7 h orbital period value in our catalogue table for this source, but other possibilities may be worth consideration.

As mentioned in Sect. 1, we decided to add all three known tMSP: XSS J12270−4859, IGR J18245−2452, and PSR J1023+0038 (all three are also listed in RK03 by the names J1227−4853, J1824−2452, and AY Sex, respectively). In addition, we include some tMSP candidates identified as such in the literature, which can be found in Table 1 with references. In the catalogue table itself, one can find a corresponding flag column named 'tMSP_Flag' (see Table B.1).

Several objects originally listed in the HMXB catalogue of Liu et al. (2006) are now moved to the current LMXB catalogue as their preferred classification changed:

– According to Karasev et al. (2008), XTE J1901+014 was suggested to be the first low-mass fast X-ray transient. However, the exact nature of this source remains unclear. Nevertheless, according to Sato et al. (2019), it appears to be more similar to a LMXB, hence its inclusion in our catalogue.
– IGR J16358−4726 was initially identified as an HMXB by Chaty et al. (2008). However, Nespoli et al. (2010) later invalidated this identification, and now the source is classified as a symbiotic X-ray binary, which we consider to be a LMXB subclass based on the typical donor mass.
– The situation is similar for IGR J17407−2808. This source was first classified as part of a supergiant fast X-ray transients (SFXT, Sguera et al. 2006), which are all HMXBs. However, subsequent works (Heinke et al. 2009; Greiss et al. 2011) ruled out the presence of a supergiant companion, and showed that this source is more likely to be a LMXB with an F-type dwarf. Kaur et al. (2011) also found that a few days after the outburst, the IR counterpart was 1 mag brighter.

Such behaviour is more expected during the LMXB outburst due to the exposure of the optical component to the X-rays emitted by the compact object.
- After analysing the X-ray spectra and near-IR observations of SAX J1452.8−5949, Kaur et al. (2009) were able to estimate the distance to SAX J1452.8−5949 ($\lesssim$ 10 kpc). This estimation eliminated the possibility of the system being a HMXB, as it would have to be an extragalactic source in that case. Consequently, the authors suggested that the binary has a low-mass companion and could either be a LMXB or an IP. Therefore, we classify SAX J1452.8−5949 as a LMXB candidate.
- It has been unclear for some time whether 4U 1807−10 is a HMXB or a LMXB. However, based on the ratio of spin and orbital periods (Blay et al. 2008), as well as the fact that the system shows type-I X-ray bursts (Chelovekov et al. 2017), we conclude that an LMXB origin is more likely for this source, despite the fact that 4U 1807−10 is marked as a HMXB candidate in Blay et al. (2008), and therefore we add 4U 1807−10 to our LMXB catalogue.

In addition, there is one source that is present in both of our catalogues, in this one, and in the one dedicated to HMXBs (Neumann et al. 2023). This is due to the presence of conflicting results and the absence of any final decision on the true nature of the source:

- Cir X−1 was originally classified as a LMXB after its discovery. However, Heinz et al. (2013) were able to determine that the system is only about 4500 years old, which led to a revision of its classification. Additionally, Jonker et al. (2007) reported that Cir X−1 contains a supergiant companion of A0 to B5 type. However, Cir X−1 has also exhibited type-I X-ray bursts (Tennant et al. 1986), which are characteristic of LMXBs. Furthermore, the fact that the companion star in Cir X−1 has yet to be decisively detected at optical wavelengths supports a possible LMXB nature for the system. Johnston et al. (2016) concluded that the optical counterpart in Cir X−1 could either be an unevolved low-mass star or a giant star that is still in the process of recovering from the supernova explosion that occurred less than 5000 years ago. Due to the ambiguity surrounding the nature of Cir X−1, the source has been included in both our LMXB and HMXB catalogues.

As mentioned previously, several objects included in RK03 and Liu07 have been removed from our catalogue. Sometimes this was necessary because objects reported as independent in RK03 and Liu07 represented the same source (in either of the catalogues). This was mainly due to large positional uncertainties at the time of the catalogue compilation, or in some cases because the objects are extragalactic. In the case of the former, we include only the element from the pair in our LMXB list with the most used name, omitting the other, and summing up all known data. In the extragalactic origin scenario, the corresponding source is removed as we only consider Galactic LMXBs. Our initial source list was therefore modified as follows:

- The relatively bright source 2A 0521−720, which is more commonly referred to as LMC X−2, is located in the LMC (as the name suggests). As we consider only Galactic objects, we exclude it from our catalogue.
- The same is true for RX J0532.7−6926 (located in LMC), and so it is also not included in the current catalogue.
- Two sources AX J1745.6−2901 and 1A 1742−289 listed in Liu07 actually correspond to the same LMXB, and as the name 'AX J1745.6−2901' is more commonly used, we combine information regarding the two from Liu07 under this name.
- The second case of identical sources is 1E 1743.1−2852 and SAX J1747.0−2853, and so again we gave the most popular name to the object, SAX J1747.0−2853.

3.3. Summary of other differences with respect to the Liu07 and RK03 catalogues

In addition to the problematic cases described above, and the overall expansion of the sample, several other changes have been made compared to Liu07 and RK03:

- To standardise the reported X-ray fluxes, we revised the energy ranges used in the Liu07 study. Instead of using a single range of 2–10 keV, we now present 'soft' and 'hard' X-ray fluxes separately, each in well-defined energy ranges.
- In addition, X-ray fluxes (absorbed) in our table are represented in cgs units (erg s^{-1} cm^{-2}, instead of Jy reported in Liu07), which are more commonly used and meaningful for X-ray sources. We also now report both maximum and minimum flux values for each of the two energy bands instead of only reporting the maximum, as done in Liu07.
- To better reflect various phenomenological features reported in the literature, we increased the number of flags used to describe the properties of the sources. In comparison to Liu07, where 11 flags were used, we use 17.
- Our new version of the LMXB catalogue has additional (in comparison with Liu07) columns for hydrogen column density, near- and mid-IR data (from 2MASS, VVV, WISE, literature, etc.), BP-RP colour, optical *Gaia*/StarHorse/literature data, and distances.
- In addition, we include up to six finding charts (from mid-IR images to hard X-ray bands) for each object, instead of just a reference to a finding chart.
- Finally, our catalogue now includes 349 objects, which is a 71% increase from the 204 objects listed in Liu07 and RK03 combined.

4. Summary and conclusions

In this paper, we present a new LMXB catalogue, which provides an up-to-date census of known LMXBs in the Galaxy with a variety of corresponding multi-wavelength information extracted from current optical/IR surveys. In total, the catalogue contains 349 sources and has 62 columns. Descriptions of the columns are presented in Table B.1. The full version of the catalogue can be obtained through the VizieR database[36], and can also be found on a dedicated website[37]. We ask authors who use our catalogue in their research to refer to us by citing this article, as well as by referring to the website link in either the acknowledgements or a footnote.

We would like to emphasise here that the origin of some of the sources listed in the catalogue is not yet certain; some sources have only been tentatively classified as LMXBs due to the similarity of their X-ray properties to those of the systems identified, with no counterparts found in other bands. Along with this

[36] https://cdsarc.cds.unistra.fr/viz-bin/cat/J/A+A/675/A199
[37] http://astro.uni-tuebingen.de/~xrbcat

article, a new similar catalogue of HMXBs is being published Neumann et al. (2023). We hope that both catalogues will be useful tools for future studies, which includes (but is not limited to) population studies of various types of X-ray-emitting objects (especially XRBs), searches for new XRBs in ongoing and upcoming surveys, classification of unidentified X-ray sources, and as training data-sets for machine learning classification algorithms (Yang et al. 2021, 2022). In particular, our catalogue be relevant in the context of the ongoing analysis of eROSITA survey data, which is expected to substantially increase the number of known XRBs (Doroshenko et al. 2014). We therefore plan to update our catalogues to the best of our ability to keep the ever-increasing census of the Galactic LMXBs up to date and accessible to the community.

Acknowledgements. This research has made use of the SIMBAD data base and VizieR catalogue access tool operated at CDS, Strasbourg, France, and NASA's Astrophysics Data System (ADS). This research has made use of "Aladin sky atlas" developed at CDS, Strasbourg Observatory, France. This work has made use of data from the European Space Agency (ESA) mission *Gaia* (`https://www.cosmos.esa.int/gaia`), processed by the *Gaia* Data Processing and Analysis Consortium (DPAC, `https://www.cosmos.esa.int/web/gaia/dpac/consortium`). Funding for the DPAC has been provided by national institutions, in particular the institutions participating in the *Gaia* Multilateral Agreement. We acknowledge the public data from *XMM-Newton*, CXO, ROSAT, *Swift*, INTEGRAL, WISE, 2MASS and VISTA. AA thanks Deutsche Forschungsgemeinschaft (DFG) for support through the eRO-STEP research unit project 414059771 (DO 2307/2-1 and WI 1860/19-1).

References

Anders, F., Khalatyan, A., Chiappini, C., et al. 2019, A&A, 628, A94
Anders, F., Khalatyan, A., Queiroz, A. B. A., et al. 2022, A&A, 658, A91
Archibald, A. M., Stairs, I. H., Ransom, S. M., et al. 2009, Science, 324, 1411
Armas Padilla, M., Corral-Santana, J. M., Borghese, A., et al. 2023, arXiv e-prints, arXiv:2305.07691
Arnason, R. M., Papei, H., Barmby, P., Bahramian, A., & Gorski, M. D. 2021, MNRAS, 502, 5455
Baglio, M. C., Mainetti, D., D'Avanzo, P., et al. 2014, A&A, 572, A99
Bagnoli, T., in't Zand, J. J. M., D'Angelo, C. R., & Galloway, D. K. 2015, MNRAS, 449, 268
Bahramian, A. & Degenaar, N. 2023, in Handbook of X-ray and Gamma-ray Astrophysics. Edited by Cosimo Bambi and Andrea Santangelo (Springer Nature Singapore), 120
Bahramian, A., Strader, J., Chomiuk, L., et al. 2018, ApJ, 864, 28
Bailer-Jones, C. A. L., Rybizki, J., Fouesneau, M., Demleitner, M., & Andrae, R. 2021, AJ, 161, 147
Bailer-Jones, C. A. L., Rybizki, J., Fouesneau, M., Mantelet, G., & Andrae, R. 2018, AJ, 156, 58
Barthelmy, S. D. 2004, in Society of Photo-Optical Instrumentation Engineers (SPIE) Conference Series, Vol. 5165, X-Ray and Gamma-Ray Instrumentation for Astronomy XIII, ed. K. A. Flanagan & O. H. W. Siegmund, 175–189
Baumann, M., Boch, T., Pineau, F.-X., et al. 2022, in Astronomical Society of the Pacific Conference Series, Vol. 532, Astronomical Society of the Pacific Conference Series, ed. J. E. Ruiz, F. Pierfedereci, & P. Teuben, 7
Blay, P., Camero, A., Connell, P., et al. 2008, in The 7th INTEGRAL Workshop, 78
Bogdanov, S. & Halpern, J. P. 2015, ApJ, 803, L27
Boller, T., Freyberg, M. J., Trümper, J., et al. 2016, A&A, 588, A103
Bonnefoy, M., Chauvin, G., Dumas, C., et al. 2009, A&A, 506, 799
Britt, C. T., Strader, J., Chomiuk, L., et al. 2017, ApJ, 849, 21
Burrows, D. N., Hill, J. E., Nousek, J. A., et al. 2005, Space Sci. Rev., 120, 165
Butters, O. W., Barlow, E. J., Norton, A. J., & Mukai, K. 2007, A&A, 475, L29
Butters, O. W., Norton, A. J., Mukai, K., & Tomsick, J. A. 2011, A&A, 526, A77
Chaty, S., Rahoui, F., Foellmi, C., et al. 2008, A&A, 484, 783
Chelovekov, I. V., Grebenev, S. A., Mereminskiy, I. A., & Prosvetov, A. V. 2017, Astronomy Letters, 43, 781
Chen, H.-L., Chen, X., Tauris, T. M., & Han, Z. 2013, ApJ, 775, 27
Chenevez, J., Alizai, K., Lepingwell, V. A., et al. 2018, The Astronomer's Telegram, 11272, 1
Christian, D. J. & Swank, J. H. 1997, ApJS, 109, 177
Clark, G. W. 2018, ApJ, 852, 121
Coleiro, A., Chaty, S., Zurita Heras, J. A., Rahoui, F., & Tomsick, J. A. 2013, A&A, 560, A108
Coti Zelati, F., Hugo, B., Torres, D. F., et al. 2021, A&A, 655, A52
Coti Zelati, F., Papitto, A., de Martino, D., et al. 2019, A&A, 622, A211
Court, J. M. C., Altamirano, D., Albayati, A. C., et al. 2018, MNRAS, 481, 2273
Cutri, R. M., Skrutskie, M. F., van Dyk, S., et al. 2003a, 2MASS All Sky Catalog of point sources. (2MASS)
Cutri, R. M., Skrutskie, M. F., van Dyk, S., et al. 2003b, VizieR Online Data Catalog, II/246
Cutri, R. M., Wright, E. L., Conrow, T., et al. 2021, VizieR Online Data Catalog, II/328
Dalton, G. B., Caldwell, M., Ward, A. K., et al. 2006, in Society of Photo-Optical Instrumentation Engineers (SPIE) Conference Series, Vol. 6269, Society of Photo-Optical Instrumentation Engineers (SPIE) Conference Series, ed. I. S. McLean & M. Iye, 62690X
De Luca, A., Caraveo, P. A., Mereghetti, S., Tiengo, A., & Bignami, G. F. 2006, Science, 313, 814
Deutsch, E. W., Margon, B., & Anderson, S. F. 2000, ApJ, 530, L21
Doroshenko, R., Santangelo, A., Doroshenko, V., Suleimanov, V., & Piraino, S. 2015, MNRAS, 452, 2490
Doroshenko, V., Ducci, L., Santangelo, A., & Sasaki, M. 2014, A&A, 567, A7
Emerson, J., McPherson, A., & Sutherland, W. 2006, The Messenger, 126, 41
Engel, M. C., Heinke, C. O., Sivakoff, G. R., Elshamouty, K. G., & Edmonds, P. D. 2012, ApJ, 747, 119
Evans, I. N., Primini, F. A., Glotfelty, K. J., et al. 2010, ApJS, 189, 37
Evans, P. A., Page, K. L., Osborne, J. P., et al. 2020, ApJS, 247, 54
Fernique, P., Allen, M. G., Boch, T., et al. 2015, A&A, 578, A114
Foight, D. R., Güver, T., Özel, F., & Slane, P. O. 2016, ApJ, 826, 66
Fortin, F., Chaty, S., Coleiro, A., Tomsick, J. A., & Nitschelm, C. H. R. 2018, A&A, 618, A150
Fortin, F., García, F., Simaz Bunzel, A., & Chaty, S. 2023, A&A, 671, A149
Gaia Collaboration, Brown, A. G. A., Vallenari, A., et al. 2018, A&A, 616, A1
Gaia Collaboration, Brown, A. G. A., Vallenari, A., et al. 2021, A&A, 649, A1
Gaia Collaboration, Prusti, T., de Bruijne, J. H. J., et al. 2016, A&A, 595, A1
Gaia Collaboration, Vallenari, A., Brown, A. G. A., et al. 2023, A&A, 674, A1
Galloway, D. K., Yao, Y., Marshall, H., Misanovic, Z., & Weinberg, N. 2010, ApJ, 724, 417
Gehrels, N., Chincarini, G., Giommi, P., et al. 2004, ApJ, 611, 1005
Giles, A. B., Swank, J. H., Jahoda, K., et al. 1996, ApJ, 469, L25
Gorgone, N., Kouveliotou, C., Younes, G., & Kennea, J. 2018, The Astronomer's Telegram, 11317, 1
Greiss, S., Steeghs, D., Maccarone, T., et al. 2011, The Astronomer's Telegram, 3688, 1
Grimm, H. J., Gilfanov, M., & Sunyaev, R. 2002, A&A, 391, 923
Heinke, C. O., Tomsick, J. A., Yusef-Zadeh, F., & Grindlay, J. E. 2009, ApJ, 701, 1627
Heinz, S., Sell, P., Fender, R. P., et al. 2013, ApJ, 779, 171
Jansen, F., Lumb, D., Altieri, B., et al. 2001, A&A, 365, L1
Jaodand, A. D., Deller, A. T., Gusinskaia, N., et al. 2021, ApJ, 923, 3
Johnston, H. M., Soria, R., & Gibson, J. 2016, MNRAS, 456, 347
Jonker, P. G., Fender, R. P., Hambly, N. C., & van der Klis, M. 2000, MNRAS, 315, L57
Jonker, P. G., Nelemans, G., & Bassa, C. G. 2007, MNRAS, 374, 999
Karasev, D. I., Lutovinov, A. A., & Burenin, R. A. 2008, Astronomy Letters, 34, 753
Kaur, R., Heinke, C., Kotulla, R., et al. 2011, The Astronomer's Telegram, 3695, 1
Kaur, R., Wijnands, R., Patruno, A., et al. 2009, MNRAS, 394, 1597
Kennedy, M. R., Breton, R. P., Clark, C. J., et al. 2020, MNRAS, 494, 3912
Knight, A. H., Ingram, A., van den Eijnden, J., et al. 2023, MNRAS, 520, 3416
Krivonos, R., Tsygankov, S., Lutovinov, A., et al. 2012, A&A, 545, A27
Kuranov, A. G. & Postnov, K. A. 2015, Astronomy Letters, 41, 114
Lamb, D. Q., Miller, M. C., & Taam, R. E. 1996, arXiv e-prints, astro
Lasota, J.-P. 2016, Black Hole Accretion Discs, Vol. 440 (Springer), 1
Li, K.-L., Strader, J., Miller-Jones, J. C. A., Heinke, C. O., & Chomiuk, L. 2020, ApJ, 895, 89
Liu, Q. Z., van Paradijs, J., & van den Heuvel, E. P. J. 2006, A&A, 455, 1165
Liu, Q. Z., van Paradijs, J., & van den Heuvel, E. P. J. 2007, A&A, 469, 807
Marocco, F., Eisenhardt, P. R. M., Fowler, J. W., et al. 2021, ApJS, 253, 8
Martí, J., Combi, J. A., Pérez-Ramírez, D., et al. 2007, A&A, 462, 1065
Masetti, N., Nucita, A. A., & Parisi, P. 2012, A&A, 544, A114
Matsuoka, M., Kawasaki, K., Ueno, S., et al. 2009, PASJ, 61, 999
Merloni, A., Predehl, P., Becker, W., et al. 2012, arXiv e-prints, arXiv:1209.3114
Middleditch, J. & Nelson, J. 1976, ApJ, 208, 567
Miller, J. M., Swihart, S. J., Strader, J., et al. 2020, ApJ, 904, 49
Minniti, D., Lucas, P. W., Emerson, J. P., et al. 2010, New A, 15, 433
Nespoli, E., Fabregat, J., & Mennickent, R. E. 2010, A&A, 516, A94
Neumann, M., Avakyan, A., Doroshenko, V., & Santangelo, A. 2023, arXiv e-prints, arXiv:2303.16137
Nucita, A. A., Carpano, S., & Guainazzi, M. 2007, A&A, 474, L1
Oh, K., Koss, M., Markwardt, C. B., et al. 2018, ApJS, 235, 4

Paduano, A., Bahramian, A., Miller-Jones, J. C. A., et al. 2021, MNRAS, 506, 4107
Papitto, A., Ferrigno, C., Bozzo, E., et al. 2013, Nature, 501, 517
Peng, S. & Shen, R.-F. 2021, ApJ, 916, 80
Predehl, P., Andritschke, R., Arefiev, V., et al. 2021, A&A, 647, A1
Rai, B., Pradhan, P., & Paul, B. C. 2018, Research in Astronomy and Astrophysics, 18, 148
Ratti, E. M., Bassa, C. G., Torres, M. A. P., et al. 2010, MNRAS, 408, 1866
Ratti, E. M., van Grunsven, T. F. J., Torres, M. A. P., et al. 2013, MNRAS, 431, L10
Revnivtsev, M. G., Kniazev, A., Karasev, D. I., Berdnikov, L., & Barway, S. 2013, Astronomy Letters, 39, 523
Ritter, H. & Kolb, U. 2003, A&A, 404, 301
Roberts, M. S. E. 2013, in Neutron Stars and Pulsars: Challenges and Opportunities after 80 years, ed. J. van Leeuwen, Vol. 291, 127–132
Rodriguez, J., Tomsick, J. A., & Chaty, S. 2008, A&A, 482, 731
Salvetti, D., Mignani, R. P., De Luca, A., et al. 2015, ApJ, 814, 88
Sato, T., Negoro, H., Iwakiri, W., et al. 2019, The Astronomer's Telegram, 13328, 1
Sazonov, S., Paizis, A., Bazzano, A., et al. 2020, New A Rev., 88, 101536
Schartel, N., González-Riestra, R., Kretschmar, P., et al. 2022, in Handbook of X-ray and Gamma-ray Astrophysics. Edited by Cosimo Bambi and Andrea Santangelo (Springer Nature Singapore), 114
Schlafly, E. F., Meisner, A. M., & Green, G. M. 2019, ApJS, 240, 30
Sguera, V., Bazzano, A., Bird, A. J., et al. 2006, ApJ, 646, 452
Shahbaz, T., Watson, C. A., Zurita, C., Villaver, E., & Hernandez-Peralta, H. 2008, PASP, 120, 848
Sidoli, L., Romano, P., Cucchiara, A., et al. 2007, The Astronomer's Telegram, 1089, 1
Skrutskie, M. F., Cutri, R. M., Stiening, R., et al. 2006, AJ, 131, 1163
Stelzer, B., Klutsch, A., Coffaro, M., Magaudda, E., & Salvato, M. 2022, A&A, 661, A44
Strader, J., Swihart, S. J., Urquhart, R., et al. 2021, ApJ, 917, 69
Sugizaki, M., Mitsuda, K., Kaneda, H., et al. 2001, ApJS, 134, 77
Swihart, S. J., Strader, J., Shishkovsky, L., et al. 2018, ApJ, 866, 83
Tananbaum, H., Gursky, H., Kellogg, E. M., et al. 1972, ApJ, 174, L143
Tendulkar, S. P., Kaspi, V. M., Archibald, R. F., & Scholz, P. 2017, ApJ, 841, 11
Tennant, A. F., Fabian, A. C., & Shafer, R. A. 1986, MNRAS, 221, 27P
Tetarenko, A., Sivakoff, G. R., Bahramian, A., et al. 2016, The Astronomer's Telegram, 8744, 1
Torres, M. A. P., Repetto, S., Wevers, T., et al. 2019, MNRAS, 487, 2296
Truemper, J. 1982, Advances in Space Research, 2, 241
Vincentelli, F. M., Cavecchi, Y., Casella, P., et al. 2020, MNRAS, 495, L37
Voges, W., Aschenbach, B., Boller, T., et al. 1999, A&A, 349, 389
Wachter, S., Wellhouse, J. W., Patel, S. K., et al. 2005, ApJ, 621, 393
Walter, R., Zurita Heras, J., Bassani, L., et al. 2006, A&A, 453, 133
Webb, N. A., Coriat, M., Traulsen, I., et al. 2020, A&A, 641, A136
Weisskopf, M. C., Tananbaum, H. D., Van Speybroeck, L. P., & O'Dell, S. L. 2000, in Society of Photo-Optical Instrumentation Engineers (SPIE) Conference Series, Vol. 4012, X-Ray Optics, Instruments, and Missions III, ed. J. E. Truemper & B. Aschenbach, 2–16
Winkler, C., Courvoisier, T. J. L., Di Cocco, G., et al. 2003, A&A, 411, L1
Winkler, C., Pace, O., & Volonté, S. 1993, ESA Journal, 17, 207
Wright, E. L., Eisenhardt, P. R. M., Mainzer, A. K., et al. 2010, AJ, 140, 1868
Yang, H., Hare, J., Kargaltsev, O., et al. 2022, ApJ, 941, 104
Yang, H., Hare, J., Volkov, I., & Kargaltsev, O. 2021, Research Notes of the American Astronomical Society, 5, 102

Appendix A: Optical/IR counterparts

Table A.1. Identified archive optical/IR counterparts of LMXBs.

Source name	*Gaia* DR3	2MASS	CatWISE2020
	Based on optical/IR/radio follow-ups:		
MAXI J0556−332	2890346074897001216		
4FGL J0427.8−6704	4656677385699742208	J04274958−6704350	J042749.64−670435.0
IGR J17494−3030	4056028099172996352		
1FGL J1417.7-4407	6096705840454620800	J14173057−4402574	J141730.57−440257.5
XTE J1637−498	5940421734427982336	J16370267−4951401	
MAXI J1807+132	4497207964419829632		
3A 1837+049	4283919201304278912	J18395759+0502113	J183957.57+050210.5
MAXI J1828−249	4076998775244833280		
1RXS J180408.9−342058	4042163562572848384		
IGR J17091-3624	5976921951382731520		J170907.75−362425.0
IGR J17585−3057	4044163406621956992		J175829.80−305702.3
4U 1543−624	5826501373348972288		
Swift J1858.6−0814	4203799300867262720		
MAXI J1305−704	5843823766718594560		J130655.74−702704.2
IGR J17329−2731	4061336747511224704	J17325067−2730015	J173250.54−273003.4
IGR J16358−4726		J16355369−4725398	J163553.75−472541.0
XMMU J174445.5−295044		J17444541−2950446	J174445.43−295044.5
IGR J17454−2919		J17452768−2919534	
4U 1705−250	4112450294268643456		
4FGL J0540.0−7552	4648562676357022208		J054001.80−755419.7
3FGL J1544.6−1125	6268529198286308224		J154439.38−112804.5
CXOU J110926.4−650224	5240167590731178624		J110926.21−650227.1
4FGL J0407.7−5702	4682464743003293312		J040731.65−570025.1
1RXH J173523.7−354013	5974787971132982144		
IGR J16287−5021	5934583950467938304		
4U 1556−60	5833042299288099072		
EXO 1846−031	4258794192383316864	J18491710−0303559	J184917.08−030355.3
AX J1735.8−3207	4055019091071763712	J17354627−3207099	
IGR J16293−4603	5942210433690960640	J16291285−4602506	J162912.85−460250.4
4U 1626−67	5809528276749789312		
SAX J1810.8−2609	4064636102946481408		
XTE J1709−267	4108865783346597760		
XTE J1710−281	4108449755564592256		
IGR J19308+0530	4294249387962232576	J19305075+0530582	J193050.75+053058.0
Swift J2037.2+4151		J20370560+4150051	J203705.60+415005.2
GS 1826−238	4077372536242802944		
SRGA J181414.6−225604	4066460746608630912	J18141475−2256195	J181414.78−225619.4
	Based on Arnason et al. (2021):		
GRO J1655−40	5969790961312131456	J16540014−3950447	J165400.13−395044.7
SWIFT J061223.0+701243	1107229825742589696		J061222.63+701243.1
1A 1246−588	6059778089610749440		J124939.17−590516.3
MXB 1659−29	6029391608332996224		

Table A.1. continued

Source name	*Gaia* DR3	2MASS	CatWISE2020
SAX J1711.6−3808	5973177495780065664	J17113714−3807073	J171137.14−380707.4
4U 1724−307	4058208396397618688	J17273315−3048076	J172733.28−304809.0
EXO 1747−214	4118590585673834624		
4U 1755−33	4042473487415175168		
HETE J1900.1−2455	4074363039644919936		
4U 1915−05	4211396994895217152		
XTE J1901+014	4268294763113217152		

Appendix B: Catalogue format

Table B.1. Description of columns in the LMXB catalogue table.

№	Column name	Unit	Description
1	'Name'		Object name, which is the most common name in the literature.
2	'RAdeg'	deg	Right Ascension in degrees (ICRS).
3	'DEdeg'	deg	Declination in degrees (ICRS).
4	'PosErr'	arcsec	Positional error in arcseconds.
5	'Coord_Ref'		The source from which the position of the object is taken.
6	'GLON'	deg	Galactic longitude in degrees.
7	'GLAT'	deg	Galactic latitude in degrees.
8	'Xray_Type'		List of the X-ray types assigned to the object. For more information see Sect. 2.1.
9	'Porb'	day	Orbital period of the binary system in days.
10	'Ppulse'	s	Pulsation period (spin) of a NS in seconds.
11	'Alt_Name'		Most frequently used alternative name.
12	'SpType'		Spectral type of the optical counterpart.
13	'Vmag'	mag	Optical magnitude in V-band according to SIMBAD database and literature.
14	'e_Vmag'	mag	Corresponding magnitude error in V-band.
15	'Gaia_DR3_ID'		Name in Gaia DR3(eDR3) catalogue.
16	'Gmag'	mag	Optical magnitude in G-band according to a Gaia catalogue or the literature.
17	'e_Gmag'	mag	Corresponding magnitude error in G-band.
18	'BP-RP'	mag	BP-RP colour.
19	'2MASS_ID'		Name in 2MASS catalogue.
20	'Jmag'	mag	IR magnitude in J-band according to 2MASS or the literature.
21	'e_Jmag'	mag	Corresponding magnitude error in J-band according to 2MASS or the literature.
22	'Hmag'	mag	IR magnitude in H-band according to 2MASS or the literature.
23	'e_Hmag'	mag	Corresponding magnitude error in H-band according to 2MASS or the literature.
24	'Kmag'	mag	IR magnitude in K-band according to 2MASS or literature.
25	'e_Kmag'	mag	Corresponding magnitude error in K-band according to 2MASS or the literature.
26	'WISE_ID'		Name in CatWISE, AllWISE, or WISE catalogue.
27	'W1mag'	mag	IR magnitude in W1 WISE band.
28	'e_W1mag'	mag	Corresponding magnitude error in W1 WISE band.
29	'W2mag'	mag	IR magnitude in W2 WISE band.
30	'e_W2mag'	mag	Corresponding magnitude error in W2 WISE band.
31	'N_H'	10^{22}cm^{-2}	Neutral hydrogen column density.
32	'MinSoftFlux'	10^{-12}erg/s/cm^2	Minimum flux (absorbed) from a source in soft X-ray.
33	'MaxSoftFlux'	10^{-12}erg/s/cm^2	Maximum flux (absorbed) from a source in soft X-ray.
34	'Soft_Xray_Var		Ratio of maximal soft X-ray flux and minimal soft X-ray flux.
35	'Soft_Xray_Range'	keV	Soft X-ray flux energy range used.
36	'MinHardFlux'	10^{-12}erg/s/cm^2	Minimum flux (absorbed) from a source in hard X-ray.
37	'MaxHardFlux'	10^{-12}erg/s/cm^2	Maximum flux (absorbed) from a source in hard X-ray.
38	'Hard_Xray_Var'		Ratio of maximal hard X-ray flux and minimal hard X-ray flux.
39	'Hard_Xray_Range'	keV	Hard X-ray flux energy range used.
40	'AG'	mag	G-band absorption A_G.
41	'Mean_Dist'	pc	Mean estimate of the distance to the binary system.
42	'Low_Dist'	pc	The lowest (minimum) estimate of the distance to the binary system.
43	'High_Dist'	pc	The highest (maximum) estimate of the distance to the binary system.
44	'Incl'	deg	Binary system inclination.
45	'Mx'	$M_\odot$	Mass of the compact object.
46	'Mopt'	$M_\odot$	Mass of the optical counterpart.
47	'B-V'	mag	B-V colour index.
48	'E(B-V)'	mag	E(B-V) colour excess.

Table B.1. continued

№	Column name	Unit	Description
49	'tMSP_Flag'		tMSP flag, which can take one of the two values, indicating that the source is: 1 — one of the three solidly considered tMSPs. 2 — a tMSP candidate.
50	'Liu07_IDX'		Ordinal number of the source in the table of Liu07 LMXB catalogue.
51	'RK03_IDX'		Ordinal number of the source in the table of RK03 LMXB catalogue.
52	'Orb_Ref'		Orbital period origin reference.
53	'Pulse_Ref'		Spin (pulsation) period of the NS origin reference.
54	'Spect_Ref'		Reference to the origin of the optical spectral type of the star.
55	'Vmag_Ref'		Reference to the origin of the V-band magnitude.
56	'Gmag_Ref'		Reference to the origin of the G-band magnitude.
57	'JHK_Ref'		Reference to the origin of the JHK information.
58	'WISE_Ref'		Reference to the WISE IR catalogue used (CatWISE, AllWISE or WISE).
59	'N_H_Ref'		$N_{\rm H}$ value origin reference.
60	'AG_Ref'		Reference to the origin of the G-band absorption $A_{\rm G}$.
61	'Dist_Ref'		Reference to the origin of the distance estimations.
62	'Mass_Ref'		Reference to the origin of the mass estimations.

6 Website

In addition to the catalogues accessible on VizieR[1][2] a website was created with the purpose to regularly update its content. This website contains the HMXBs catalogue of Neumann et al. (2023) and the LMXBs catalogue of Avakyan et al. (2023).

On the home page of the website, users have the overview of the spatial distribution of HMXBs and LMXBs. The default image layer is an all-sky image of eROSITA, but can be switched to other surveys ranging from infrared (allWISE) over soft X-rays (XMM-Newton) to hard X-rays (INTEGRAL). In this interactive map the LMXBs are represented as red circles and the HMXBs as blue squares. The user can click on one of those symbols to open a popup with more information about this source, this includes the source name and coordinates but also other information like the magnitude in different energy bands. It is possible to click on the source name in the popup, if the user wants to see the available information in a more organized way. The link which is stored as the source name, redirects the user to a new webpage which contains the information of this object. In the following, the general structure of the webpage is described for the case of HMXBs. The differences between the webpages for HMXBs and LMXBs are described at the end of this section. The general information is separated into four main parts, plus an additional part for miscellaneous information and finding charts at the end of the webpage.

The first part contains the coordinates, this includes right ascension (RA) and declination (DEC) in sexagesimal units in the ICRS J2000 reference system. If the positional uncertainty is available, this value is also given in the third row in arcsec. Also available are the galactic coordinates which were calculated from RA and DEC. The last row in this part then contains the reference paper for the coordinates, in case it is available. The user can use the coordinate-reference link that redirects them to the Astrophysics Data System (ADS) operated by NASA. The redirection to the NASA ADS website basically applies to all following references.

The second part contains general information about the binary system, starting with an alternative name for the source; this alternative name was selected as the second most common name used for the binary system. The alternative name is the object

[1] https://vizier.cds.unistra.fr/viz-bin/VizieR?-source=J/A+A/677/A134
[2] https://vizier.cds.unistra.fr/viz-bin/VizieR?-source=J/A+A/675/A199

identifier, which is the second most common identifier used in the abstract of paper about the specific object. In the next row, a summary of X-ray types is given to which the binary belongs, those X-ray types are described in Neumann et al. (2023) as well as how they were compiled. The mean distance as well as the distance range is given in kiloparsecs (kpc). If a reference is given in form of a superscript number, a different paper was used than the Gaia Collaboration et al. (2023), Bailer-Jones et al. (2021), or Anders et al. (2022) as described in Neumann et al. (2023). Swift/XRT nH-column density values in $10^{-21}\,\mathrm{cm}^2$ are the last information in this part.

The third part contains essential information of the compact object in the binary system. If mass estimations of the compact object are available, the mean mass as well as a mass range can be found in this part similar to the distance estimations described earlier. The mass estimation of the compact object is given in solar masses $\mathrm{M}_\odot$. The user can also find the orbital period and in case of NSs also the pulsation period and their corresponding references in this part. The orbital period is given in days and the pulsation period in seconds. For NSs systems with known cyclotron resonant scattering feature (CRSF), the line-energy of this feature is given in this part in keV. In general, if only one energy is given, this would be the energy of the fundamental line, in the case where more energies are provided also higher harmonics are included. In this part the user can find fluxes for the different X-ray instruments, this includes XMM-Newton, Chandra, Swift/XRT, Swift/BAT and INTEGRAL. If multiple observations with the same instrument are available, the maximal and the minimal flux values are given as a flux range. For all five instruments the values are provided in units of $10^{-12}\,\mathrm{erg\,cm^{-2}s^{-1}}$, the energy-range of the instrument is given in brackets at the end of the line.

The last big block of this page contains the information on the optical companion. Starting with the Gaia identifier, if a Gaia counterpart is identified, the name of the source in the most recent Gaia catalogue (Gaia DR3) is given here. In addition to that, the following line should visualize if the identification of the optical companion is solid, tentative or if no optical companion is detected so far. If the spectral type of the optical companion is known, the next line contains the spectral type with a corresponding reference. The following six lines list the magnitudes in different wavelength bands. The included bands are G-band (330–1050 nm) from Gaia, the J-band (centered at $1.235\,\mu\mathrm{m}$) from 2MASS, as well as H-band (centered at $1.662\,\mu\mathrm{m}$) and $\mathrm{K_S}$-band (centered at $2.159\,\mu\mathrm{m}$), and for WISE the W1-band (centered at $3.4\,\mu\mathrm{m}$) and the W2-band (centered at $4.6\,\mu\mathrm{m}$). If there is a value for the effective temperature of the optical companion reported, either by Gaia Collaboration et al. (2023) or Anders et al. (2022) this estimation can be also found in this section.

Luminosity values of the optical companion reported by Gaia Collaboration et al. (2023), were also added in this part.

Any additional information which could be useful can be found in the comments section, this includes but is not restricted to the informations like super orbital periods for the X-ray binary system or if the system is only a XRB candidate. Another small section contains other references which were collected during the creation of the catalogue but could be allocated to one of the values above. At the very bottom of the website finding charts are provided for the user, ranging from near infrared with VVV to hard X-rays with INTEGRAL, the creation as well as the explanations of the markers are described in Neumann et al. (2023).

In general, the webpages for the LMXBs are structured in the same way as the ones for the HMXBs with some adjustments. In addition to the G-band magnitude, a value for the extinction in the G-band is provided. Another difference is that instead of reporting the flux ranges for every single instrument, the fluxes for the soft X-ray instruments (Chandra, XMM-Newton, and Swift/XRT) are combined to one single flux range, the same was done for the hard X-ray instruments (Swift/BAT and INTEGRAL). Due to the fact that the instruments are combined, an additional field was added, which informs the reader about the energy range for which the flux is reported. In the cases where, a flux range is reported instead of a singular value, the variability is calculated. For the optical companion the only additional field is the mass of the star and the respective reference.

The 'HMXB Cat' and 'LMXB Cat' buttons at the top of the webpages allows the user to navigate to a different webpage which includes all objects in a tabular format. In this table the user has a possibility to search for a specific source by using the source name in the search bar or sort the systems for example, by increasing or decreasing spin period. Additionally, at the bottom of the table there are the FITS-file, VOT-file, and csv-file of the current version of the catalogues, as downloadable files.

Last but not least, the 'Updates' webpage provides the user not only with the newest version of the catalogues as a FITS-, VOT-, or csv-file but also the older versions. In addition to that, this page provides the user with information about what changes were done to the catalogue, e.g added sources, or the updated parameters of systems.

7 Updating the Catalogue

Adding New Sources

The following chapter describes how to update and maintain the website, using the HMXBs-catalogue as an example. In general, updating the LMXBs-catalogue is done similarly. However, as I only modified the scripts for the HMXBs-catalogue for easier use, I cannot comment on the steps which need to be undertaken to update the LMXBs-catalogue, for this please consult Artur Avakyan[1].

Prerequisites

A few prerequisites need to be fulfilled, for the pipeline to work as intended. The overall folder structure can be seen in the Directory Tree in Figure 7.1.

First and foremost, the most recent iteration of the catalogue needs to be in the 'XRBcats_HMXB'-folder, typically it is called 'XRBcats_HMXB.fits'. Also the most recent 'IDs_cat.pickle' file should be in the root-folder of this project. This file contains the most popular names for the sources in the catalogue. In general, this file should automatically update if new sources are added to the catalogue. The script for the most popular ids is depending on the api-token from NASA-ADS which has a daily limit of requests. Upon reaching the limit, a new account needs to be created to generate a new api-token or one needs to wait 24 hours.

All already created Finding Charts should be in the 'HMXB_Charts'-folder, from there they will be copied into the right folder as soon as the script starts. Lastly, the 'HMXBTemplate.html' file should be stored in the 'HMXBTemplate'-folder.

[1] `https://arturavakyan.github.io/`

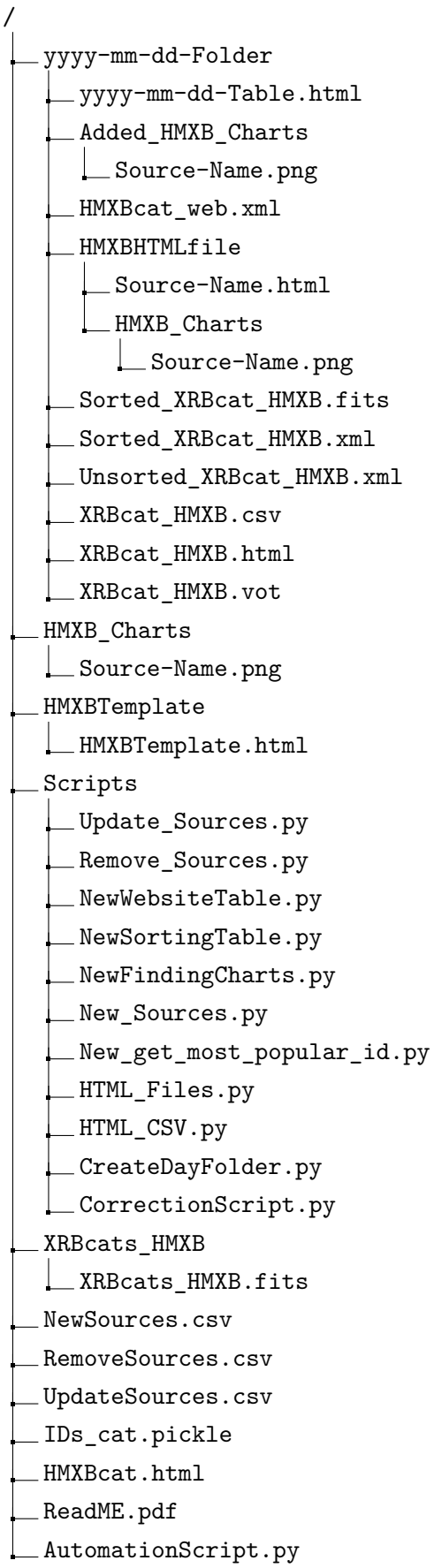

Figure 7.1. – Project structure for updating the HMXBs catalogue.

New Sources

To add new sources to the catalogue, the user needs to fill in information about the source into the 'NewSources.csv' file. In general, all information can be added in this file, however, the source name as well as the coordinates are necessary fields that needs to be filled. In principle, it is sufficient to only provide the coordinates; however, it is recommended to add a source name which is resolvable by SIMBAD, else issues could arise in the other parts of the script that depends on the source name.

Update Sources

To update a specific source, the user needs to add the source to the 'Update-Sources.csv' file, in general any identifier which is listed in the catalog can be used in the 'Name'-column; however, it is recommended to use the identifier which is already used as the name in the catalogue. Any new information regarding the source should be filled in the corresponding field of the file. The most common fields are already added in the 'UpdateSources.csv' file, nevertheless missing fields can be added. In the case that a field is added to the file and the script is not working anymore, it needs to be adjusted accordingly.

Removing Sources

If a source is no longer classified as a HMXBs, it can be removed from the catalogue. In order to do this, one of the source identifier needs to be added in the 'RemoveSources.csv' file. Similar to the other cases every source identifier can be used, but it is strongly suggested to use the source name.

For all three cases (New Sources, Update Soures and Remove Sources), it is in general not necessary to remove older entries from former updates, but removing them should also not influence the outcome of the later updates.

Run Script

Once all prerequisites have been met and all changes were added to the respective files, the 'AutomationScript.py' can be run. This script executes the others in quick succession. Starting with 'CreateDayFolder.py', this script creates a folder with the name (yyyy-mm-dd) indicating the current date, when the script was executed. It

also creates two additional folders into this, first is the 'Added_HMXB_Charts'-folder and the other is the 'HMXBHTMLfile'-folder. As the name indicates, the newly created finding charts will be copied into the 'Added_HMXB_Charts'-folder. Similar to the 'Added_HMXB_Charts'-folder, the html-files of the single sources are copied into the 'HMXBHTMLfile'-folder. 'CreateDayFolder.py' also copies the already existing finding charts into the 'HMXB_Charts'-subfolder inside the 'HMXBHTMLfile'-folder. Finally, the 'HMXBTemplate.html' file is also copied into the yyyy-mm-dd-folder and renamed yyyy-mm-dd-Table.html which is later used to create the html-table[2] on the website. The following three scripts (Update, Remove and New_Sources_Scripts) are changing the .fits-file accordingly to the changes in their respective .csv-file. The changes to the catalogue are saved in the 'Updated_XRBcats_HMXB.fits'-file. In cases of new sources added to the catalogue, those are saved in the 'Unsorted_XRBcat_HMXB.xml'-file. For now the new sources are only appended at the end of the list, to solve this 'Sort_func.py' is sorting the list in ascending order of the RA-coordinate. The now sorted table is saved as 'Sorted_XRBcat_HMXB.fits' and 'Sorted_XRBcat_HMXB.xml'. 'HTML_CSV_Script.py' is creating a .csv-file for the updated catalogue, saving it as 'XRBcat_ HMXB.csv'. In addition to the .csv-file it also creates a .vot- and .fits-file with the same syntax. Furthermore, a html-version ('XRBcata_HMXB.html) of the catalogue is created by 'HTML_CSV_Script.py' however, in this file the source names are replaced with an hyperlink, which redirects the user of the website to the corresponding html-file of the source. 'HTML_Files.py' is creating a single html-webpage for every source and saves it with the source name in the 'HMXBHTMLfile'-folder. The last script is the 'WebsiteTabel_Script.py' which also changes the source name in the .xml-file to a hyperlink which later can be used on the website in the Aladin-skymap to access the single source html-file. This new xml-file is saved as 'HMXBcat_web.xml'.

To-Do

Before uploading the files to the website, a couple of minor changes need to be done manually in some files. In the future this could be done automatically, but currently it needs to be done manually. First of all, the finding charts of the new sources need to be copied from the 'Added_HMXB_Charts'-folder to the 'HMXB_Charts'-folder inside the 'HMXBHTMLfile'-folder. After that, it is necessary to replace inside the 'XRBcat_HMXB.html' file all occurrence of '<' with '<' and all '>' with '>'. Next, the user needs to copy everything inside the yyyy-mm-dd-Table.html file between the <html> and </thead> -tags (including <html> and </thead>) into the

[2] http://astro.uni-tuebingen.de/ xrbcat/HMXBcat.html

'XRBcat_HMXB.html' file in the same position. In a similar fashion, everything between the </table> and </html>-tags (including </table> and </html>) is copied from the yyyy-mm-dd-Table.html file to the end of the 'XRBcat_HMXB.html' file. As a last change, one needs to replace the datatype 'long' for the 'Gaia_DR3_ID'-column inside the 'HMXBcat_ web.xml' to 'double', otherwise the catalogue-overlay in the Aladin-window on the website does not show the entries.

Updating the Website

After creating all the necessary files, it is time to update the website. To do so, the user needs to connect through ssh and change the necessary files in the 'public_html'-folder of the 'xrbcat'-user. Before uploading the files, one should create an additional subfolder in the 'HMXBcat'-folder, typically the folder name is choosen to be 'MonthYear' (e.g. 'March2025'). Inside the 'HMXBcat'-folder there is the 'Current_Version' folder, this is not the current version but an artifact from the initial release of the website (i.e. the oldest version of the catalogue). Inside the 'MonthYear'-folder one needs to copy the .csv-, .fits- and .vot-files of the updated catalogue. The naming convention can be found in the Table 7.1.

File Name	Website Name
HMXBcat_web.xml	HMXBcat_web.xml
XRBcat_HMXB.csv	HMXBcat.csv
XRBcat_HMXB.vot	HMXBcat.vot
XRBcat_HMXB.fits	HMXBcat.fits
XRBcat_HMXB.html	HMXBcat.html

Table 7.1. – File names which are created by the script and how they need to change for the website.

The single source html-files should be copied into the 'HMXBHTMLfile'-folder and their corresponding finding charts into 'HMXB_Charts'-subfolder. This can be also done by uploading the whole 'HMXBHTMLfile'-folder from the local machine into the 'public_html'-folder. 'HMXBcat_web.xml' and 'XRBcat_HMXB.html' can be uploaded into the 'public_html'-folder and renamed accordingly to Table 7.1. In addition to that, the directory-path as shown in Figure 7.2 at the end of the 'HMXBcat.html'-file needs to be updated.

Changes in the catalogue should be also explained on the 'Updates' webpage. For that one needs to add the changed information in the 'Updates.html'-file. An example of such a change can be seen in Figure 7.3.

```
<div class="">
  Current Version:
        <a href="./HMXBcat/September2023/HMXBcat.fits" download="HMXB_cat.fits"> HMXB_cat.fits</a>,
        <a href="./HMXBcat/September2023/HMXBcat.vot" download="HMXB_cat.vot"> HMXB_cat.vot</a>,
        <a href="./HMXBcat/September2023/HMXBcat.csv" download="HMXB_cat.csv"> HMXB_cat.csv</a><br><br>
  Previous versions of the catalog can be found under <a target="_self" href="./Updates.html">Updates</a>.<br><br>
```

Figure 7.2. – Lines which need to be changed in the 'HMXBcat.html'-file (e.g. September2023 → March2025).

```
<div class="row" style="margin-top: 50px;">
    <div class="cell-6">
        <h3>HMXB</h3>
    <h4>13. March 2025:</h4>
    <a href="./HMXBcat/March2025/HMXBcat.fits" download="HMXB_cat.fits"> HMXB_cat.fits</a>,
        <a href="./HMXBcat/March2025/HMXBcat.vot" download="HMXB_cat.vot"> HMXB_cat.vot</a>,
        <a href="./HMXBcat/March2025/HMXBcat.csv" download="HMXB_cat.csv"> HMXB_cat.csv</a><br>
    <h6> Added HMXB:</h6>
    <a target="_blank" href="./HMXBHTMLfile/4XMM J181330.1-17511.html">4XMM J181330.1-17511</a><br>
    <h4>15. August 2024:</h4>
    <a href="./HMXBcat/August2024/HMXBcat.fits" download="HMXB_cat.fits"> HMXB_cat.fits</a>,
        <a href="./HMXBcat/August2024/HMXBcat.vot" download="HMXB_cat.vot"> HMXB_cat.vot</a>,
        <a href="./HMXBcat/August2024/HMXBcat.csv" download="HMXB_cat.csv"> HMXB_cat.csv</a><br>
    <h6> Added HMXB:</h6>
    <a target="_blank" href="./HMXBHTMLfile/CXOU J182531.4-144036.html">CXOU J182531.4-144036</a><br>
    <a target="_blank" href="./HMXBHTMLfile/Swift J1845.7-0037.html">Swift J1845.7-0037</a><br>
    <h6> Removed HMXB:</h6>
    IGR J16327-4940 : most likely a <a href="https://ui.adsabs.harvard.edu/abs/2023MNRAS.526.2560S">LMXB</a><br>
    IGR J17586-2129 : probably a <a href="https://ui.adsabs.harvard.edu/abs/2018A%26A...618A.150F"> CV </a> or  <a href="https://ui.adsabs.harvard.edu/abs/2022sf2a.conf...39D">
    SyXB</a><br>
    <h6> Updated Field: </h6>
     <a href="./HMXBHTMLfile/2MASS J08504008-4211514.html">2MASS J08504008-4211514</a>: Mean Distance changed to 12.0 kpc (<a href=https://ui.adsabs.harvard.edu/abs/
     2024MNRAS.528L..38D>De et al. 2024</a>)<br>
```

Figure 7.3. – Example html-code for updates.

Part II

Probabilistic Background Removal for XMM-Newton Data

8 Introduction

Noise is an intrinsic property in all imaging fields. While this is not a problem in everyday applications (e.g. taking pictures on your vacation in Sicily), this poses a problem in imaging fields where the amount of photons are low. How to deal with noise is an ever developing field, while there are multiple methods they have their own advantages and disadvantages. One of the approaches involves modeling the background however, it often requires the modeling of the X-ray source first. This is not always a feasible option specially in the case of a newly detected source. An alternative method is the subtraction of an offset value however, for a very faint source, it's possible that due to the Poissonian fluctuation, the background needed to be subtracted is higher than the source count itself leading to a negative value. However, due to low event rates in such cases, removing a possible source event can be a huge loss. To counteract this we used a technique proposed by Ehlert et al. (2022) in conjunction with background map we developed to test if this could be a valuable addition for the X-ray Multi-Mirror Mission.

This project is structured as follows, Chapter 9 introduces the instrument and the components that make up the background. Chapter 10 explains the mathematical foundation of the estimator and its benefits. Additionally, the workflow to create the background maps and the metrics which were used to evaluate the performance of the estimator are described in Chapter 10. In Chapter 11 the estimator is applied on an artificial source as a proof of concept and later to the real observations. The last chapter; Chapter 12 concludes this part of the thesis.

9 Instruments

9.1 XMM-Newton

The X-ray Multi-Mirror Mission (XMM-Newton) was launched on December 10, 1999 as one of the cornerstone missions in the 'Horizon 2000' program of the European Space Agency (ESA). It was launched into a highly elliptical orbit (apogee $\sim 114000\,\mathrm{km}$) with an orbital period of 48 hours (Jansen et al., 2001), provided which, uninterrupted exposures of up to 65 ks are possible (Jansen et al., 2001). However, because XMM-Newton has no onboard storage capability (Lumb et al., 2012) all obtained data needs to be downlinked to the ground station immediately. Originally planned for a mission lifetime of ten years, XMM-Newton is now over 25 years operational and might continue working until 2030 (Kirsch et al., 2014). The ten meter long and four tons heavy spacecraft has six different instruments on-board. The Optical/UV Monitor (OM) is mounted at the front of the spacecraft, allowing observation in optical and ultraviolet band between $170\,\mathrm{nm}$ and $650\,\mathrm{nm}$ (Mason et al., 2001). Together with the other instruments, it provides the possibility for a simultaneous multiwavelength observation. Behind two of the three X-ray telescopes a Reflection Grating Array (RGA) is installed (seen in Figure 9.1). The RGA deflects about half of the incoming light onto the Focal Plane Camera (RFC), together they form the Reflection Grating Spectrometer (RGS) instrument, providing high-resolution spectroscopy in the 0.3–$2.1\,\mathrm{keV}$ energy range (den Herder et al., 2001). The undeflected light (about 44% of the original flux) is detected by one of the European Photon Imaging Camera (EPIC) Metal Oxide Semi-conductor (MOS) Charge-Coupled Device (CCD) detectors at the focus of the telescope (Turner et al., 2001). At the focus of the third telescope, with an unobscured beam path, another EPIC detector is installed, the EPIC pn-detector. Both EPIC detector types are described in more detail in the following sections.

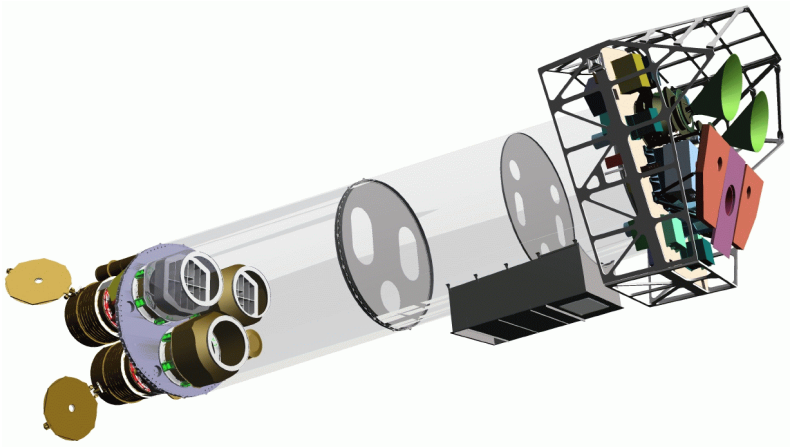

Figure 9.1. – XMM-Newton spacecraft. Image courtesy of Dornier Satellitensysteme GmbH and ESA. ESA/XMM-Newton, CC BY-SA 3.0 IGO. Cropped from original.

EPIC MOS-CCD

The EPIC MOS-CCD detectors (hereafter MOS-detector) consists of seven front-illuminated MOS-CCDs, that partially overlap each other (as seen in Figure 9.2) to minimize dead space (Turner et al., 2001). In the full-frame mode the MOS-detector has an imaging area of 600×600 with a pixel size of $40\,\mu\mathrm{m} \times 40\,\mu\mathrm{m}$, to increase the time resolution it is possible to reduce the imaging area. The different scientific modes of the MOS-detector are described later in this section. The limiting factor for the MOS-detector is its quantum efficiency that limits the detector to an energy range of 0.2–$10\,\mathrm{keV}$ (Turner et al., 2001). With its smaller pixel size the MOS-detector has a better spatial resolution in comparison to the pn-CCDs and a slightly better energy resolution (ESA: XMM-Newton SOC, 2025).

Besides the full frame mode, the MOS-detector has additional three modes, the large and small window mode as well as the timing mode. In each modes, the reduction of the imaging area is only applied to the central CCD. Everything inside the imaging area is kept while everything outside is discarded during the readout. For the full frame mode, the whole central CCD is operational, which means the imaging section of the central CCD is a square of 600×600 pixels, with a time resolution of 2.6 seconds (Turner et al., 2001). For bright sources, it is recommended to either use the large window (300×300 pixels) with a timing resolution of 0.9 seconds or the small window (300×300 pixels) with an even lower time resolution of 0.3 seconds (Turner et al., 2001). In the timing mode, a row of 100 pixels is compressed into one dimension, losing the spatial information of the source but achieving the lowest time resolution (1.75 ms) of all MOS-detector modes (Turner et al., 2001).

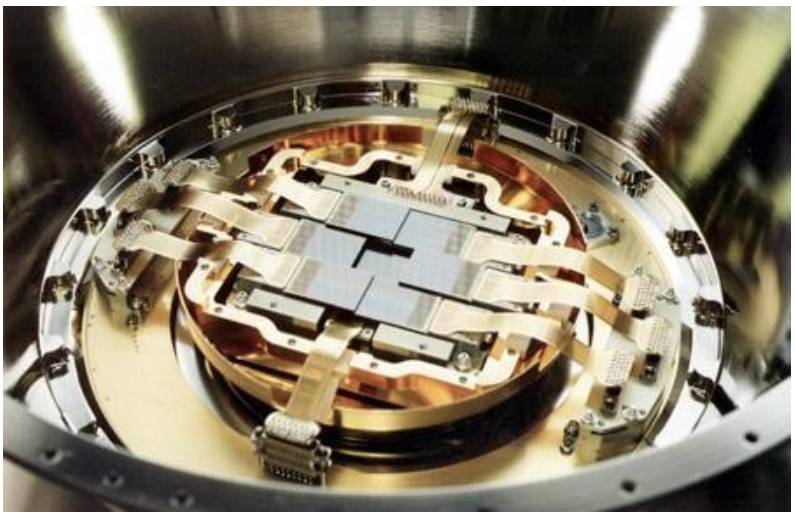

Figure 9.2. – Image of the EPIC MOS-detector. Image courtesy of Leicester University, University of Birmingham, CEA Service d'Astrophysique Saclay and ESA. ESA/XMM-Newton, CC BY-SA 3.0 IGO. Cropped from original.

EPIC PN-CCD

The EPIC pn-detector (hereafter pn-detector) was produced on a single wafer and consists of 12 pn-CCDs (as seen in Figure 9.3) which are back illuminated (Strüder et al., 2001). Similar to the MOS-detector, the pn-detector can be operated in different scientific modes, in the full frame mode the pn-detector has an imaging area of 398×384 pixels with a pixel size of $150\,\mu\mathrm{m} \times 150\,\mu\mathrm{m}$, and a time resolution of 73.4 ms (Strüder et al., 2001; ESA: XMM-Newton SOC, 2025). The MOS-detector might have a higher spatial resolution due to its smaller pixel-size, however the pn-detector has a significantly higher quantum efficiency which allows for efficient detection of photons up to 15 keV (Strüder et al., 2001).

The different modes in which the pn-detector can be operated are the full frame, extended full frame, large and small window mode as well as timing and burst mode. In the full frame and extended full frame mode the whole pn-detector is read out. This means a total of 376×384 pixels need to be read out, which results in a time resolution of 73.4 ms for the full frame mode as described earlier (ESA: XMM-Newton SOC, 2025). In the extended full frame mode the readout time stays the same, however, the integration time is increased for a total time resolution of 199.1 ms, which makes this mode suitable for extended sources (ESA: XMM-Newton SOC, 2025). In the large window mode only the inner half of the CCDs are used for imaging (198×384 pixels), this lowers the time resolution to 47.7 ms (ESA: XMM-Newton SOC, 2025). In the small window mode, the imaging area is decreased to 63×64 pixels on one of the twelve CCDs, with that an even faster readout is achieved

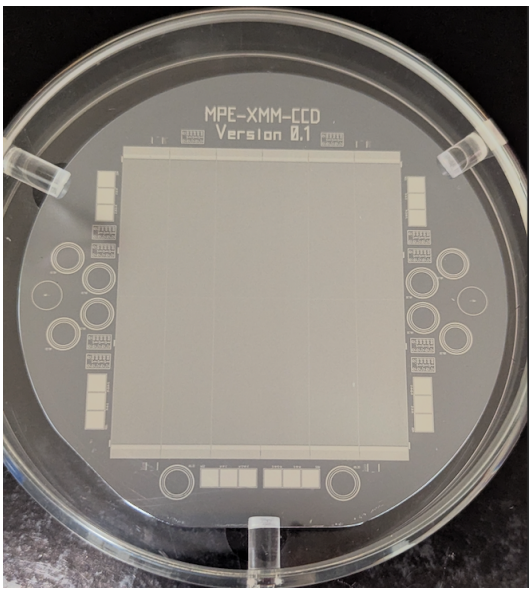

Figure 9.3. – Image of the EPIC pn-detector prototype at the Institute for Astronomy and Astrophysics in Tübingen.

Window Mode	Time resolution [ms]		Image Size [pixel]	
	MOS	pn	MOS (cent. CCD)	pn
ext. full frame		199.1		376×384
full frame	2600	73.4	600×600	376×384
large window	900	47.7	300×300	198×384
small window	300	5.7	100×100	63×64
timing	1.75	0.03	100×600	64×200
burst		0.007		64×180

Table 9.1. – The different science modes for the EPIC MOS-detector and the EPIC pn-detector with their imaging area in pixels and their respective time resolution.

further reducing the time resolution to 5.7 ms (ESA: XMM-Newton SOC, 2025). Similar to the timing mode in the MOS-detector, a row of pixels are compressed into one dimension for the timing (64×200 pixels) and burst modes (64×180 pixels), achieving a time resolution of 0.03 ms and $7\,\mu$s respectively (ESA: XMM-Newton SOC, 2025). A full list can be seen in Table 9.1.

9.2 Background Components

As XMM-Newton is flying through space, there are interactions of the detector with its surrounding which can not be avoided. Such interactions can be separated into particle-like, electronic noise, and photon background. Each of these exhibit a unique temporal, spectral, and spatial behaviour. In the following sections, the components are described in further detail.

Soft Protons

Soft protons are one of the particle components in the EPIC background. They are solar soft protons, that are accelerated by magnetospheric reconnection events in the sun reaching energies of a few hundred kilo-electron volts. Thereafter, they are trapped by the Earth's magnetosphere, where they get collected by the mirrors and focused onto CCDs. Soft protons are the dominating component in times of high background as seen in the lightcurve of the XMM-Newton observation 0841320101 (Figure 9.4a) however, XMM-Newton's analysis software has tools to remove those times of high background as seen in Figure 9.4b. The soft proton flares are highly unpredictable, affecting around 36% of the observation time (Kuntz and Snowden, 2008). However, as mentioned in Kuntz and Snowden (2008), regions such as the ones closer to the magnetopause have a higher possibility of flares. (Kuntz and Snowden, 2008) also mention that greatest flare-free times occur when the satellite is outside the bowshock in summer or when it is deep within the magnetotail in winter. The intensity of the soft proton flares is also highly variable and can reach up to 1000% of the intensity in quiescence (Carter and Read, 2007). As the soft protons are focused, they are typically only observed within the Field of View (FOV), but during intense unfocused solar flares the counts outside the FOV can also be increased (Carter and Read, 2007). The spectrum of soft protons are variable in shape and intensity, but the continuum for energies above $0.5\,\mathrm{keV}$ can be modeled with a broken power-law with a break-energy at around $3.2\,\mathrm{keV}$ (Kuntz and Snowden, 2008).

Cosmic-ray Induced

The cosmic-ray induced instrumental background is the component of the background produced by the interaction of high energy particles with the detector. While the component typically varies up to 10% during an observation (Carter and Read,

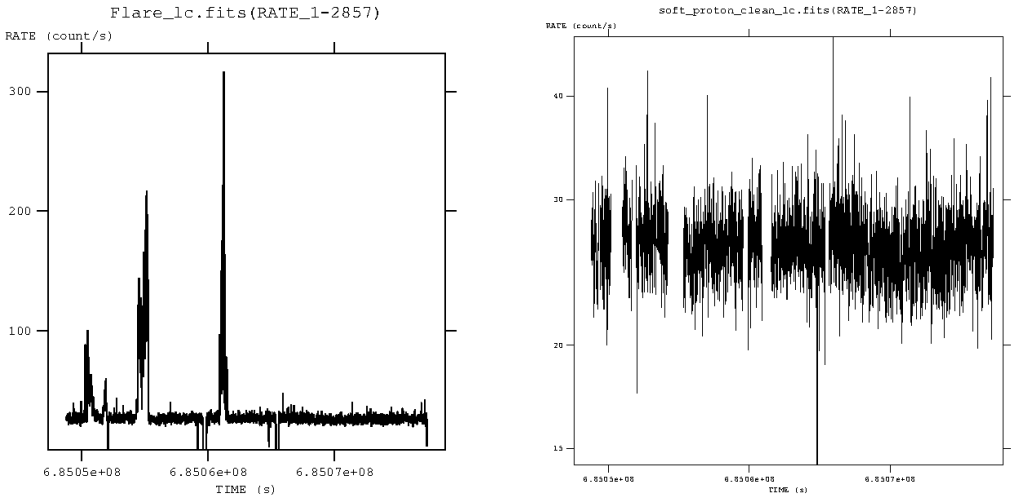

(a) (b)

Figure 9.4. – Lightcurves of the observation 0841320101. Figure 9.4a shows the original lightcurve before clean-up. Figure 9.4b is the lightcurve after removing times of soft proton flares.

2007), the changes between observations can be more significance, since it depends on the flux of the particles which has a larger timescale than usual observations (De Luca and Molendi, 2004). During the intense solar flares this component can vary up to 10 times the normal intensity (Carter and Read, 2007). The interaction of cosmic rays with the detector typically result in instrumental fluorescence lines, for the pn-detector those lines can be seen at $1.5\,\mathrm{keV}$ (Al-K) or in the energy range of 7.48–$9.57\,\mathrm{keV}$ for the Ni-,Cu-, and Zn-lines (Freyberg et al., 2004), see Figure 9.5 for a spectrum of the Filter-Wheel-Closed data with visible instrumental lines. The intensities of the instrumental lines show spatial variation from the electronic board (Figure 9.6) behind the detector, the most prominent variation being the copper-free zone in the center of the pn-detector (Figure 9.7) (Carter and Read, 2007). Some residual contributions of minimum ionizing particles can be seen close to the CMOS Amplifier and MultiplEXer (CAMEX) readout at the top and bottom of the detector (Figure 9.8).

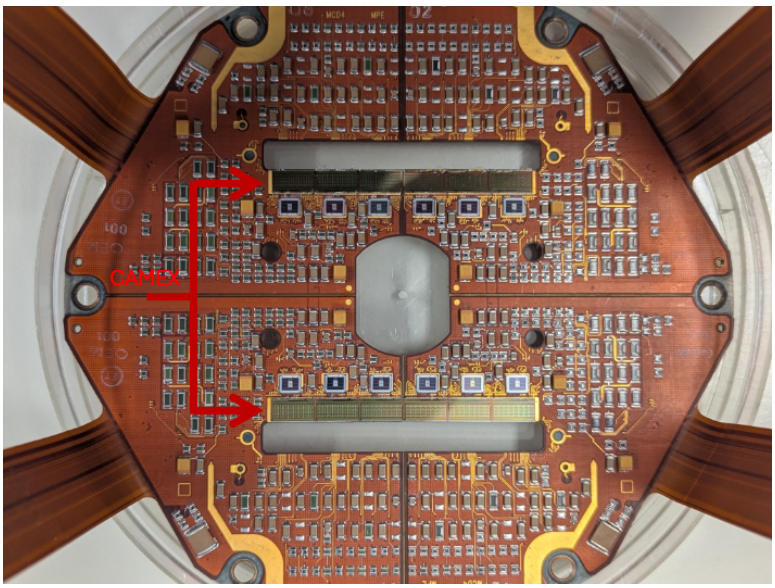

Figure 9.6. – Image of the electronic board on which the pn-detector is mounted. The red arrows indicates the CAMEX read-out chips at the top and bottom of the detector.

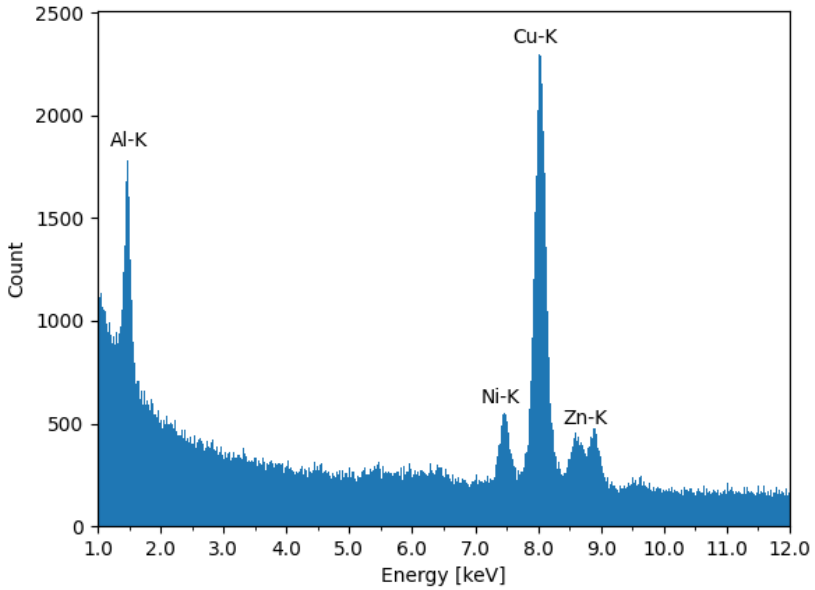

Figure 9.5. – EPIC pn-spectrum in 1.0–12.0 keV energy range, created from the Filter Wheel Closed data. Instrumental lines are clearly visible at around 1.5 keV and 7.0–9.0 keV.

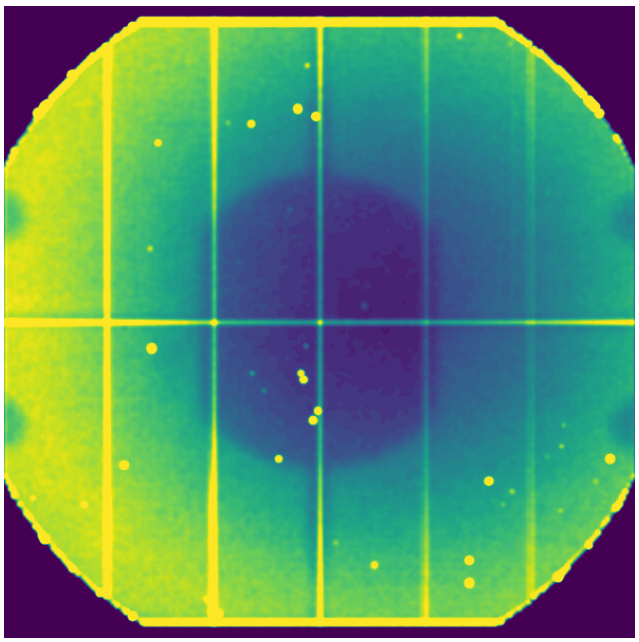

Figure 9.7. – Image of the background in the energy range 7.2–9.2 keV. The "copper-hole" is clearly visible in the center of the image, as well as the four screw holes at the edge of the detector.

Electronic Noise

The electronic noise component of the background includes bright pixels, bright columns, and the read-out noise of the CAMEX (Figure 9.6). The bright pixels and columns, for example caused by micro-meteorites can vary up to 10% during an observation (Carter and Read, 2007), but an even larger fluctuation can be seen between observations, since sometimes they do not contribute to the observations while on other occasions they are active again. The CAMEX read-out noise on the other hand is mostly stable during a single observation and its variation depends on the observation-mode. The lowest read-out noise is achieved in the extended full frame mode, while the small window mode suffers the most (Carter and Read, 2007). Bright pixels and columns are seen at the location where the detector is damaged (Figure 9.8), while the read-out noise is at the top and the bottom of the CCD near the CAMEX (Figure 9.8).

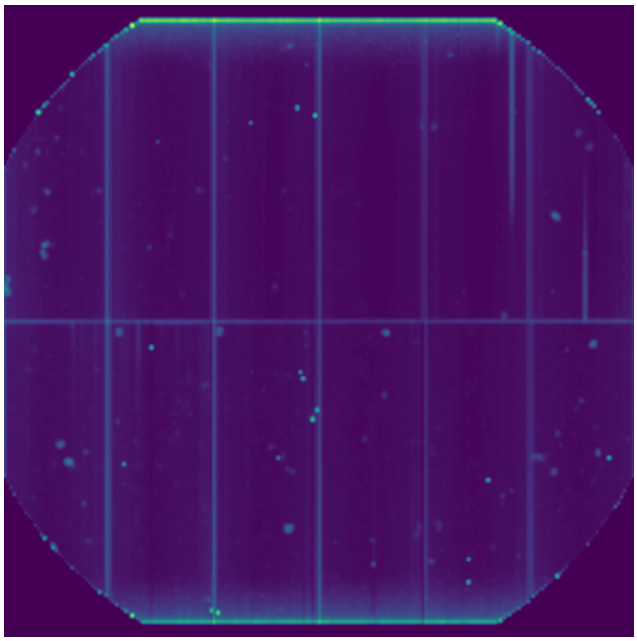

Figure 9.8. – Image of the background in the energy range 200–400 eV. Increased background levles are visible at the top and bottom of the CCD close to CAMEX. Also bright pixels are visible, distributed all over the CCD, and bright columns in the top right corner.

X-ray

The photon background can be further classified into nonthermal (hard) X-rays and thermal (soft) X-rays.

Hard X-rays: The main contributors of hard X-rays in the FOV of the detector are unresolved Active Galactic Nuclei (AGN), apart from that, straylight from sources outside the FOV and Out-of-Time (OoT) events in case of the pn-detector (Carter and Read, 2007) also contribute to the same. The hard X-ray component is the dominant factor below $5\,\mathrm{keV}$ in times of low background and can be modeled by a power-law with photon-index of ~ 1.4 (Carter and Read, 2007). Straylight could originate from all kinds of sources outside the FOV which are singly reflected by a mirror shell into the FOV (Carter and Read, 2007), producing arcs in the resulting image as seen in Figure 9.10.
OoT events are typically seen in observation of bright sources. As the detector registers the photons during the readout, it is possible that some of these photons get a wrong position assigned on the CCD (ESA: XMM-Newton SOC, 2025). Because such OoT events happen during the readout, they can be seen as a straight line between the source and the readout (Figure 9.9) (ESA: XMM-Newton SOC, 2025). OoT events are also mode-dependent, similar to the electronic read-out noise. Since, the amount of OoT events depends on the read-out time, modes with faster read-out are typically experience fewer OoT events. The full-frame mode has the highest fraction of OoT events followed by the extended full frame which has the same readout-time but a higher integration time (Carter and Read, 2007). The large window mode, with 0.16% has the lowest fraction of OoT events (ESA: XMM-Newton SOC, 2025).

Soft X-rays: The effect of soft X-rays show similar behavior as the hard X-rays, this includes OoT events, straylight as well as the diffuse X-ray background. However, the origin of the diffuse X-ray background differs from the origin of hard X-rays. Instead of unresolved AGNs the soft X-rays originate from the local bubble, the galactic halo, and galactic disk but could also originate from the Solar Wind Charge Exchange (SWCX) (Carter and Read, 2007). As described in Cravens (1997) and Snowden et al. (2004) the SWCX is the interaction of highly charged ions in the solar wind with neutral material in the heliosphere or the Earth's exosphere. In long observation the SWCX-component of the soft X-ray background can affect the observation Carter and Read (2007). Spectral-wise observations which were influenced by SWCX exhibit stronger features of the OVII and OVIII emission lines

(Carter and Sembay, 2008). The contributions from galactic sources show a thermal component with emission lines below $1\,\mathrm{keV}$, whereas the extragalactic component above $0.8\,\mathrm{keV}$ can be modeled with a power-law with photon-index of 1.4 (Carter and Read, 2007). The diffuse contributions are also pointing-dependent and can vary up to 35% depending on right ascension (RA) and declination (DEC) (Carter and Read, 2007). Straylight and OoT events influence the observations in the same way as the hard X-ray.

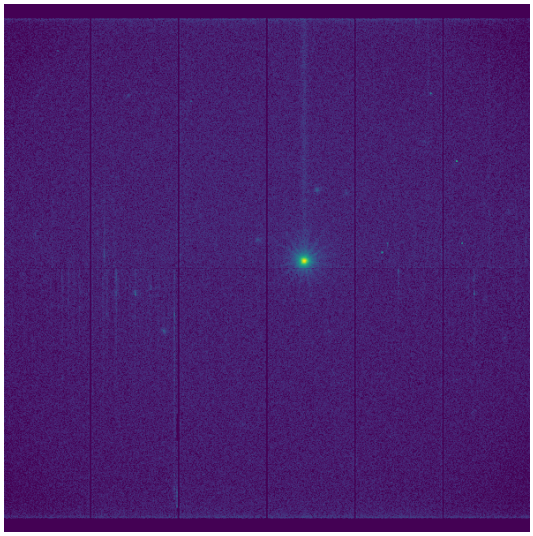

Figure 9.9. – Image of Her X-1 with a straight line between the source and the readout at the top, caused by OoT events.

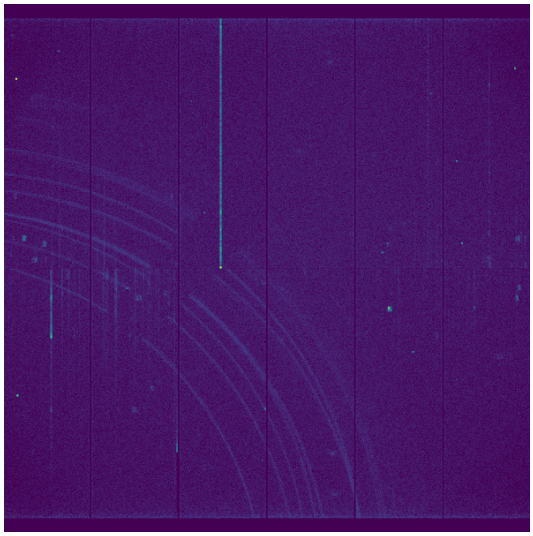

Figure 9.10. – Image of a region where photons from a out-FOV bright source (SPICY 70967), are single-reflected into the FOV, producing the Straylight-arcs.

10 Methods

10.1 Statistical Methods

High energy astrophysics deals with mostly single incoming photons hence, it is reasonable to assume a Poisson distribution in this scenario. The probability of observing k photons from a source while expecting μ Photons can be calculated using the following equation:

$$P(k|\mu) = \frac{e^{-\mu}\mu^k}{k!} \tag{10.1}$$

It is however important to note that the photons from the source, and the photons from the background are usually drawn from two independent Poisson distributions. However, the subtraction of the background from the source results into a distribution that is no longer a Poisson distribution, but a Skellam distribution Skellam (1946). Let's consider an observation with k events, it is then possible to hypothesize that k_N events originate from the background and k_S from the source. It is evident that both values are non-negative and add up to k. It is important to note that, since it is only possible to measure the combination of k_N and k_S directly and not individually, the probabilistic estimator should account for all possible realizations of k_N and k_S (i.e. k_N reaching from 0 to k). In order to comprehend the probabilistic estimator, it is first necessary to understand what a microstate is. Within the area of interest, the microstate is defined as one of many combinations of k_N and k_S to sum up to k. For each of these microstates, the posterior probability density function (PDF) [1] for an expectation value of μ_S is calculated, while observing k_S events and assuming that every value of μ_S has the same probability to be correct (i.e. an uniform prior for μ_S). The posterior PDF of this microstate is given by the normal Poisson distribution:

$$P(\mu_S|k_S) = \frac{e^{-\mu_S}\mu_S^{k_S}}{k_S!} \tag{10.2}$$

Since $P(\mu_S|k_S) \sim P(k_S|\mu_S)P(\mu_S)$ and given the uniform prior, it can be deduced that the posterior PDF will be maximum where:

[1] posterior PDF: probability density function of a hypotheses after observing new data.

$$\frac{\partial P(k_S|\mu_S)}{\partial \mu_S} = 0 \tag{10.3}$$

The result of this calculation is the point $\mu_S = k_S$. Substituting k_S by the relation $k = k_S + k_N$ would result in the maximum at $\mu_S(k_N) = k - k_N$. It is possible to calculate the probability of observing a given number of background counts, given an estimated expected background count μ_N and the overall counts k:

$$w(k_N|\mu_N, k) = \frac{e^{-\mu_N}\mu_N^{k_N}}{k_N!} \tag{10.4}$$

The expected source count μ_S^* in the region of interest can be calculated by utilizing $\mu_S(k_N)$ and $w(k_N|\mu_N, k)$ in the following formula:

$$\mu_S^* = \frac{1}{V_1}\sum_{k_N=0}^{k} \mu_S(k_N) * w(k_N|\mu_N, k) \tag{10.5}$$

with V_1 being the sum of the weights $w(k_N|\mu_N, \mu_S, k)$:

$$V_1 = \sum_{k_N=0}^{k} w(k_N|\mu_N, \mu_S, k) \tag{10.6}$$

Examples of the newly calculated μ_S^* are shown in Figures 10.1 to 10.3. All histograms show the probability $w(k_N|\mu_N, k)$ of observing $k_N = k - k_S$ background events while expecting μ_N events originating from the background and k total events. While the red line indicates the expectation value for the source events as calculated from the probabilistic estimator.

Figure 10.1 shows the case where a total of $k = 2$ events were detected and it is expected that $\mu_N = 0.5$ of such events originate from the background. Using a simple subtraction would result in an expected source count of $\mu_S = 1.5$, however, the calculation from the probabilistic estimator reveals an expected source count of $\mu_S^* \sim 1.5385$ (marked by the red line in Figure 10.1). The real benefits of the probabilistic estimator however, lies in the low, and high count limits.

The low count limit in our case is where the expected background count exceeds the overall count by a significant amount. Two cases of the low count limit are shown in Figure 10.2. Figure 10.2a shows the result for an expected background count of $\mu_N = 10$ and an overall count of $k = 3$ while Figure 10.2b shows the result for $\mu_N = 50$ and $k = 3$. A subtraction would yield in both cases an unphysical

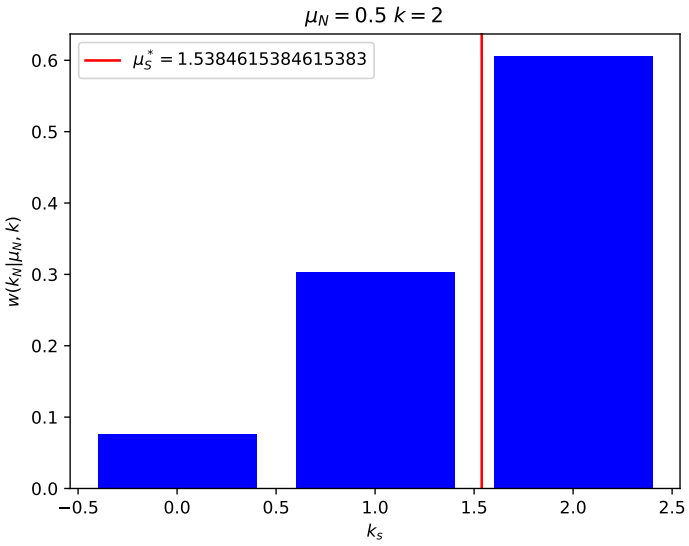

Figure 10.1. – Histogram for an expectation value for the background of $\mu_N = 0.5$ and an overall count rate of $k = 2$.

negative expected source count; $\mu_S = -7$ for the $\mu_N = 10$-case and $\mu_S = -47$ for the $\mu_N = 50$-case. The probabilistic estimator, on the other hand, outputs a non-negative expected source count, in case of $\mu_N = 10$ the resulting expected source count is $\mu_S^* = 0.3206$ and in the $\mu_N = 50$-case it is $\mu_S^* = 0.0611$.

The high count limit, in our case is when there is a significant number of overall events, in this case the desired outcome should be similar to a simple subtraction. Figure 10.3 shows two of such high count limit cases. Figure 10.3a shows the case where the expected background count is $\mu_N = 10$ and the overall count is $k = 20$, the other case is for $\mu_N = 10$ and $k = 1000$. In these scenario, a simple subtraction would yield an expected source count of $\mu_S = 10$ and $\mu_S = 990$ respectively. In the best scenario, the estimator would output similar values, and indeed for the case of $k = 20$ the estimator calculates the expected source count to be $\mu_S^* = 10.0187$. For $k = 1000$, it is even more prominent, as the expected source count of the estimator is $\mu_S^* = 990.0000$.

In conclusion, the probabilistic estimator shows some advantageous features in comparison to a simple subtraction. In the low count limit it stays positive and converges to zero (as seen in Figure 10.2) in comparison to negative counts for a simple subtraction. Whereas, in the high count limit it converges to a similar result as a simple subtraction as seen in Figure 10.3.

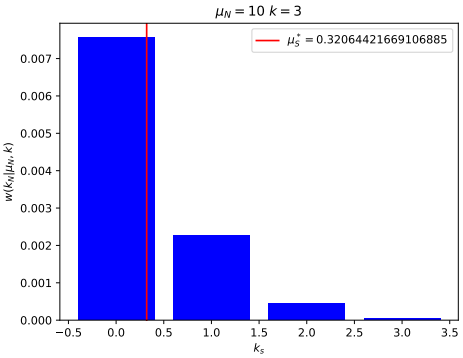

(a) Histogram for an expectation value for the background of $\mu_N = 10$ and an overall count rate of $k = 3$.

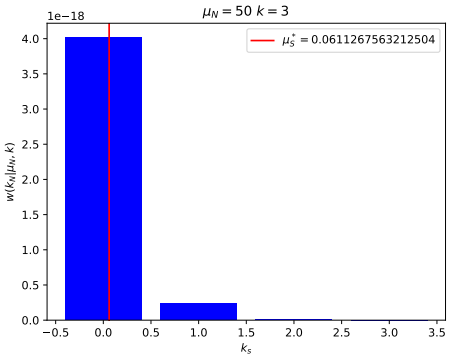

(b) Histogram for an expectation value for the background of $\mu_N = 0.5$ and an overall count rate of $k = 2$.

Figure 10.2. – Example calculation of the probabilistic estimator in low count limits.

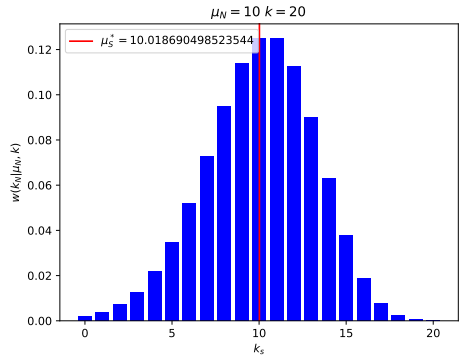

(a) Histogram for an expectation value for the background of $\mu_N = 10$ and an overall count rate of $k = 20$.

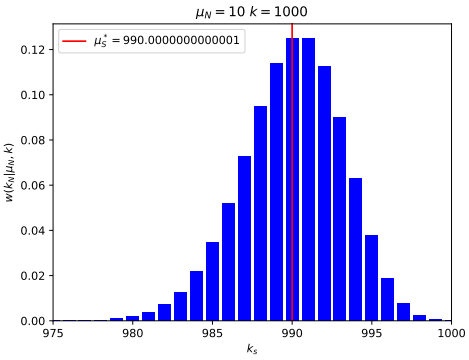

(b) Histogram for an expectation value for the background of $\mu_N = 10$ and an overall count rate of $k = 1000$.

Figure 10.3. – Example calculations of the probabilistic estimator in high count limits.

So far, we have only calculated an expected source count. However, this alone does not help to clean up an event list from potential background events. For the probabilistic estimator to be useful, another parameter needs to be defined which uses the output of the estimator. By combining the estimated expected background count μ_N and the newly calculated expectation value for the source counts μ_S^*, it is possible to estimate the probability that an individual event originates form a source photon as:

$$p_S = \frac{\mu_S^*}{\mu_N + \mu_S^*} \tag{10.7}$$

Similarly, the probability that the event originates from the background can be calculated as:

$$p_N = \frac{\mu_N}{\mu_N + \mu_S^*} \tag{10.8}$$

Three distinct techniques to create meaningful images using p_S or p_N were proposed by Ehlert et al. (2022).

First technique is the 'Random Removal'. In this technique, a random number is drawn from a uniform distribution between 0 and 1. This is then compared with the p_S-value of an individual event. Depending on whether the number is greater than or less than p_S, the event is flagged as either a background or a source event. The process of drawing a random number and comparing it with the p_S-value is repeated for every individual event. A principal disadvantage of this technique is predicated on its random nature. It is conceivable that, on the one hand, hot pixels or areas with an artificial high event count can survive the process. Conversely, events from a 'real' source could be removed, thereby reducing its Signal-to-noise ratio (SNR).

Another alternative to the 'Random Removal' method is the creation of a fractional photon map. The 'Fractional Photon' technique does not remove events outright, rather it assigns a fraction of a photon to the event. The fraction of the photon is determined by the probability of the event originating from a source photon p_S. Since no events are entirely removed, there are far more non-zero value pixels in comparison to the 'Simple Subtraction' technique.

The third technique described by Ehlert et al. (2022), that utilizes the estimator, would be the false probability map. Instead of the p_S-value, this method makes use of the p_N-value. In the scenario where a mission involves multiple telescopes with similar performance, the probability can be calculated as follows:

$$p_F = \prod_j p_{N,j} \tag{10.9}$$

with $p_{N,j}$ being the p_N-value of one of the telescopes. The false probability is then calculated as $1-p_F$. This technique can be used to identify regions with an atypically high source count rate.

10.2 Data Processing

In order for the background calculation to work, two parameters must be considered. Firstly, the overall count of the observation k and secondly, the expected background count μ_N. The total count is easily obtainable by using the eventlist of the observation. However, the process of obtaining μ_N is somewhat more complex. A long-term observation, which does not show any known sources, could be a good estimation of the background, including an instrumental, and astrophysical source of the background, which could help reduce the computation time. Such long-term observation does not exist therefore, the idea was to stack the background maps of multiple observations, creating a single background map which serves as a database for the background count estimation. However, it is anticipated that the background will vary according to the energy band. Consequently, it was imperative to devise distinct background maps for each energy band in order to estimate μ_N accurately. The following chapter will provide a comprehensive explanation of the methods used in achieving this goal.

Observation Selection

XMM-Newton has accumulated a significant number of observations over the course of its 25-year scientific operation, it is imperative to select a suitable set of observations for the following steps.

In order to find suitable observation, the XMM-Newton Serendipitous Source Catalogue in the 4XMM Version, in particular, the Data release 13 (4XMM-DR13) was utilized (Webb et al., 2020).

With the provided information of start and end of the observation as well as the summed up Good Time Interval (GTI) time (time of low background activity) of the pn-CCD, it was possible to calculate the ratio between observation-time and GTI time. Depending on the ratio, only observations were selected with at least 10% of their total exposure time contained in the pn-GTI. Following the initial selection of observations, an additional filtering step was required, since XMM-Newton has a

variety of different imaging modes and depending on that the image size is different as described in Section 9.1.

In order to guarantee that the images have a common size, only observations in which MOS1/MOS2 and PN operated in PrimeFullWindow-Mode (Table 9.1 for a summary of the window modes) were selected. A further point to consider was, that XMM-Newton has the capability to remove point-like sources however, the process of removing extended sources like supernova remnants is more complicated. Fortunately, the 4XMM catalogue includes a parameter that facilitates the identification of observations with extended sources. This parameter is referred to as 'EP_EXTENT' and indicates the extended radius in arcsec of an object as determined by **emldetect**. It was determined that observations in which sole objects with a $\mathrm{EP\_EXTENT} = 0$ were detected should be selected for further processing. After all those prerequisites, a total of 1339 unique observation IDs were obtained for further processing.

Energy-Band Separation

As mentioned above, it is expected that the background differs depending on the energy range. Consequently, it is required to define energy ranges in which the background-maps are created. Katayama et al. (2004) separated the full energy range (0.2–$12\,\mathrm{keV}$) into seven energy bands. Their lowest energy band is the 0.2–$0.4\,\mathrm{keV}$. It is characterized by the dominating X-ray noise around the read-out nodes. Three other energy bands (0.4–$1.3\,\mathrm{keV}$, 1.7–$4.0\,\mathrm{keV}$, 4.0–$7.2\,\mathrm{keV}$) are characterized by the Cosmic X-ray Background (CXB). In addition to the CXB component, the 1.7–$4.0\,\mathrm{keV}$ and 4.0–$7.2\,\mathrm{keV}$ energy band also shows internal instrument background. This internal background is also a characterizing feature in the 9.2–$12.0\,\mathrm{keV}$ energy band. The instrumental lines are the characteristics of the 1.3–$1.7\,\mathrm{keV}$ (Al-K) and 7.2–$9.2\,\mathrm{keV}$ (Ni-K, Cu-K and Zn-K) energy band. Inspired by the aforementioned separation, we devised energy bands seen in Table 10.1.

In order to encompass both the lowest and the highest energies, two additional energy-bands were created ($< 0.2\,\mathrm{keV}$ and $> 12\,\mathrm{keV}$). Furthermore, the 1.7–$4.0\,\mathrm{keV}$ and 4.0–$7.2\,\mathrm{keV}$ energy bands were combined into one single 1.7–$7.2\,\mathrm{keV}$ energy band, as they exhibit the same features and to reduce the runtime of the extraction.

Nr	Name	Energy-Range (keV)
1	very low	<0.2
2	low	0.2–0.4
3	CXB Internal 1	0.4–1.3
4	AlK	1.3–1.7
5	CXB Internal 2	1.7–7.2
6	NiCuZn	7.2–9.2
7	CXB Internal 3	9.2–12.0
8	very high	>12.0

Table 10.1. – The eight energy ranges in which the full range of 0–$12\,\mathrm{keV}$ was seperated.

μ_N-Map Creation

Following the selection of observations to be used for further processing and the definition of the energy bands in which the μ_N should be created, the proper data processing can begin. The initial step in the process was to download the observation. In order to do so, the observation ID was used to search through the XMM Science Archive [2], and the corresponding Observation Data File (ODF) was then downloaded. After unpacking the files, the XMM-Newton Science Analysis System (XMM-SAS) start-up was done as explained on XMMs data analysis thread[3]. The Calibration Index File (CIF) and the SAS summary file (SAS) were created using **cifbuild** and **odfingest** respectively. As the event list is one of the obligatory inputs in the majority of the following procedures, the subsequent step was to create the event list. This was done using **epchain** for the pn-detector and **emchain** for both MOS-detectors. It may appear counterintuitive to create the event list for the MOS-detectors, given that the current focus is to test the method first on the pn-detector before extending it to the MOS-detectors in the future. However, it should be noted that the MOS event lists are a prerequisite for the **cheese** task, which should remove the point-like sources.

As the pn-CCDs are subjects to OoT events, it was necessary to rerun the **epchain** task with **withoutoftime**=True. The **epchain** and **emchain** tasks provide some filtering of the data, e.g. removing bad pixels. However, to filter soft-proton contamination, a specific task can be utilised. The functionality of **espfilt** involves an attempt to fit a gaussian onto the histogram, which was created by using the lightcurve values from the events in the FOV of the detector. The peak of the gaussian is then considered to be the nominal count rate, and everything above a certain σ that can be set by the user (in our case 3σ) are discarded.

[2] https://nxsa.esac.esa.int/nxsa-web/#home
[3] https://www.cosmos.esa.int/web/xmm-newton/sas-thread-startup

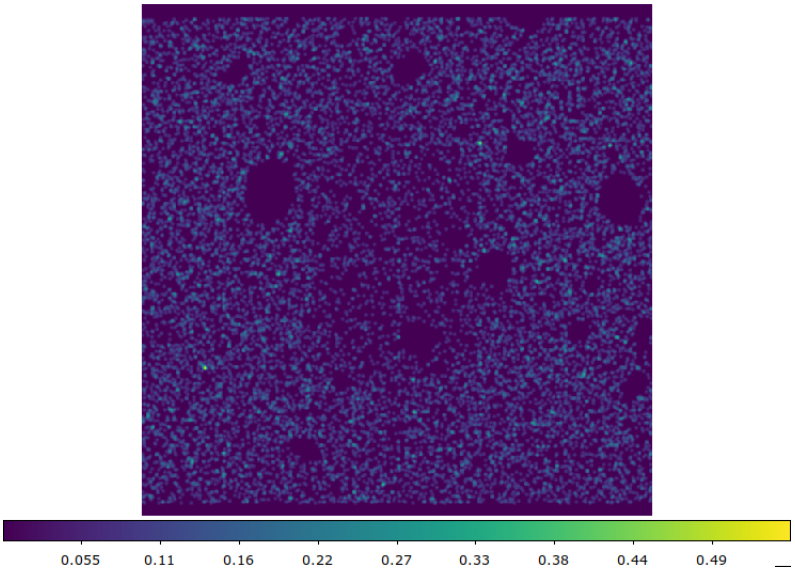

Figure 10.4. – Resulting image in the linear scale in the energy band $7.2 - 9.2\,\mathrm{keV}$ after using region-file outputed by **cheese**-task.

XMM-SAS provides the user with the **cheese** task to remove point-like sources. One of the parameters that must be specified in the **cheese** task is the energy range. In this instance, the task required multiple iterations to encompass all the energy ranges presented in Table 10.1. In addition to the energy bands previously mentioned, the task was repeated once more for the $0.4 - 1.25\,\mathrm{kev}$ energy-band. This decision was made on the basis that the result obtained using this energy-band showed promise in terms of point-like source removal, which had previously been disregarded in the other energy-bands. The most important output of the **cheese** task is the region file, which contains all the different regions utilised in the observation to conceal the sources. Using the region file in the 'expression'-parameter in the **evselect** task, an image can be created in which the point-like sources are covered by these regions, therefore no counts from such sources contribute in this area. Such a resulting image without point-like sources is shown in Figure 10.4.

In order to obtain an exposure-corrected image, it was first necessary to create exposure maps in the corresponding energy bands. This was achieved by utilizing the **eexpmap** task. It was possible to create the 'cheese'-images using **evselect**; however, it was proven to be impossible to create "cheesy"-exposures utilizing the same method. In order to create the "cheesy"-exposures, it was necessary to create a region-mask using **regionmask** task. In a later stage of the process, the region-masks were used in conjunction with the exposure-maps in their respective energy-bands to create the "cheesy"-exposures. Despite the fact that a total of 1339 observations were selected for further processing, it was not possible to process all of them,

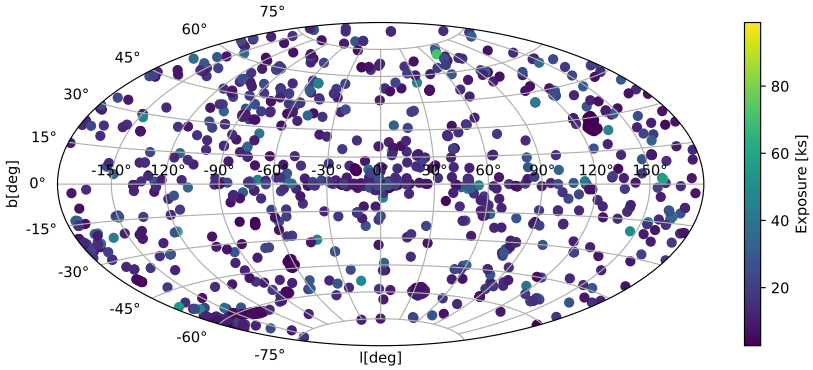

Figure 10.5. – Galactic coordinate map of the observation which were used to generate the μ_N-maps.

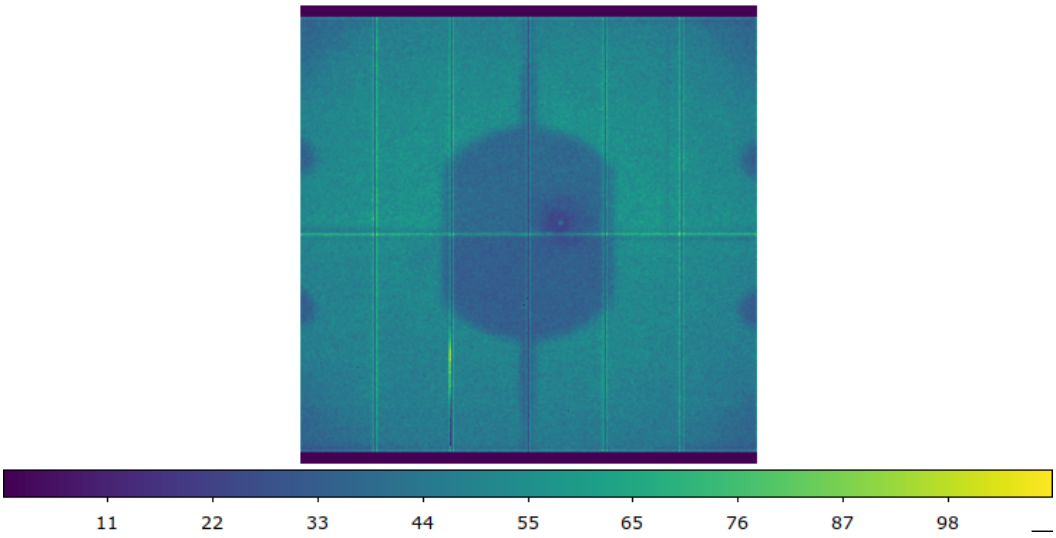

Figure 10.6. – Resulting image in linear scale in the 7.2–$9.2\,\mathrm{keV}$ energy range after stacking.

due to missing data. A total of 1282 single images and exposure maps, from 1282 observations were obtained for each of the energy bands, from all areas in the sky as seen in Figure 10.5

However, all of these images contained "holes". The objective was to obtain a background map without such "holes". In order to address this issue, the images were stacked. The underlying idea was that the sources are not always detected in the same position within the CCD. This means that the "holes" present in one observation can be masked by other observations, ensuring that the final product is a single image in every energy band without any zero-count areas. As an example, the resulting image in the energy range 7.2–$9.2\,\mathrm{keV}$ is shown in Figure 10.6 The exposure maps were processed in a similar manner; however, it should be noted that XMM-SAS

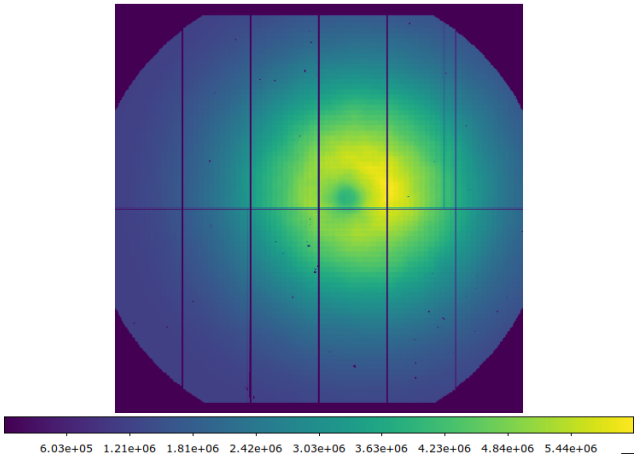

Figure 10.7. – Resulting exposure map in linear scale for the 7.2–9.2 keV energy range after stacking of the individual "cheesy"-exposures.

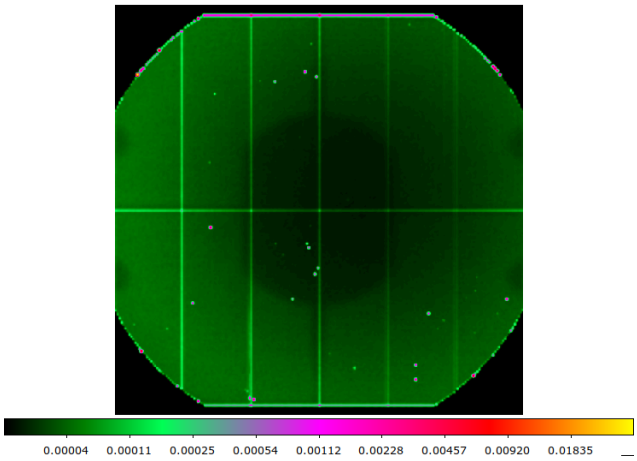

Figure 10.8. – Exposure-corrected background image in the 7.2–9.2 keV energy range. A different colorscale was selected to make the copper-free region in the center of the CCD more visible.

does not possess the capability to generate the same "cheesy"-exposures as for normal images, as previously described. Therefore, the exposure maps were multiplied with the masked produced by **regionmask**, thereby producing the "cheesy"-exposures prior to their stacking. A resulting stacked exposure maps in the same energy range than Figure 10.6 can be seen in Figure 10.7. In order to carry out the exposure correction, the stacked image was divided by its corresponding exposure map in each energy-band. This process resulted in the creation of exposure corrected μ_N-map, which can be utilised in conjunction with the probabilistic estimator to calculate the expected source count μ_S. Figure 10.8 shows the exposure-corrected μ_N-map for the 7.2–9.2 keV energy band.

Eventlist Preparation

The preceding step yields one of the two ingredients needed for the probabilistic background removal. The images which can be used to calculate the expected background counts μ_N. The other main ingredient is the overall counts k which is the combination of the expected background counts μ_N and the expected source counts μ_S. To obtain the overall counts it is necessary to extract and filter the XMM-Newton observation which should be analysed.

The steps for obtaining the event list are analogous to the steps in the creation of the background images. First, the setup steps as explained in the previous section with **cifbuild** and **odfingest**. Because only the calibrated event list of the pn-detector is of interest, this time only the **epchain** task is necessary. After that, the event list is cleaned up from soft proton events with the help of the **espfilt** task. With that, all the necessary ingredients for the background removal are ready. The expected background counts in different energy bands as an image and the overall counts as an event list.

Background Removal

The first step to implement the background removal technique, is to separate the events in their corresponding energy bands. The following steps are then done for every energy band individual, starting with transforming the detector coordinates into image coordinates to make them comparable with the already created background images described in the previous chapter. As described in the image extraction [4] within the **evselect** task, the LTM_{11}, LTM_{22}, LTV_1, and LTV_2 parameters can be used to transform the physical coordinates into image coordinates. After transforming the coordinates, the **binned_statistic_2d** function from the Python **scipy.stats** package can be used to create an image of the distribution of the counts. It is possible to use other functions which also create two-dimensional histograms like the **histogram2d** from the **numpy** package. However, the key advantage of **binned_statistic_2d** is that with the parameter **expand_binnumbers**=true the function can also output the bin numbers which proves useful later on. To get the expected background μ_N, the stacked image in the specific energy range is multiplied by the live time of the central CCD. This time can be found in the header of the event list under the keyword 'LIVETIME'. With the image of the overall counts and the expected background count image in the same energy range, the probabilistic estimator can now calculate the expected source counts μ_S^*.

[4] https://xmm-tools.cosmos.esa.int/external/sas/current/doc/evselect/node10.html

After calculating μ_S^*, it is finally possible to calculate the probability for the events to be originating from the source p_S. The output of this procedure is a p_S-map in the same size than the original image, because it is an important parameter for both background removal techniques ('Fractional Photons' and 'Random Removal') this p_S-map is saved in a separate file. But the values should be also part of the event list, for example if someone wants to filter the event list with XMM-SAS commands. For that, the image coordinates of the p_S-map needs to be transformed back to the detector coordinates, to ensure that every event gets assigned the right value. Now the expanded bin number comes in handy, because the additional output has the same size as the X- and Y-list which was used to create the image, therefore, the first element in the bin number list also belongs to the first event in the filtered event list for the specific energy range. So by seeing into which bin (or better pixel) this event belongs, it is possible to retrieve the right value from the p_S-map by checking the value of the pixel. In the end, the entire list of p_S-values can be attached to the event list. Simultaneously, to retrieve the p_S-value a random number between zero and one is drawn from a uniform distribution, and compared to the p_S-value. This step is important for the background removal using the 'Random Removal' technique. If the random number is smaller, than the p_S-value an 1 is attached to the event while for the other cases an 0 is attached. This value is saved in a similar fashion as the p_S-value in a separate column in the event list.

10.3 Evaluation Methods

Signal to Noise Ratio

To later evaluate the performance of the background removal methods, we made use of different statistical metrics, which are typically used in X-ray astronomy. First of all, we used the Signal-to-noise ratio (SNR) to quantify the detected source against the statistical fluctuation of the background. The calculation of the SNR was done using:

$$SNR = \frac{C_S}{\sqrt{C_{tot}}} \tag{10.10}$$

with C_S the reconstructed source count and C_{tot} the total counts (i.e. detected background and source counts), which was adopted from Goldwurm and Gros (2022). The corresponding uncertainty is calculated using error propagation, under

the assumption that C_{tot} consists of two independent variables C_S (Source-Count), and C_B (Background-Count):

$$C_{tot} = C_S + C_B \tag{10.11}$$

As mentioned earlier, it is expected that the background changes in the different energy ranges, therefore, we calculated the source counts as well as the total counts for every energy range individual. In the end, all the individual values were combined using a slightly modified version of Equation (10.10):

$$\frac{\sum_{i=2}^{7} C_{S,i}}{\sqrt{\sum_{i=2}^{7} C_{tot,i}}} \tag{10.12}$$

with $C_{S,i}$ being the source count in the energy range 'i' described in Table 10.1 and $C_{tot,i}$ the total detected counts in the same energy range. The reason why the very low and the very high energy range are excluded originates from the fact that with the normal filtering we applied, there are typically no events left in those energy ranges. In all of the three different background removal methods, the total count $C_{tot,i}$ is calculated in the same way, by using every event in the event list in a specific energy band and creating an image with those events. However, the source count $C_{S,i}$ might differ depending on the method in use.

For the 'Simple Subtraction', the source count is reconstructed by creating an image of the expected background using the stacked background images and multiplying it with the exposure time of the observation. Then the background image is subtracted from the image of the total counts. In areas with low overall counts this can result in negative counts, since this would be unphysical, those events are set to zero instead. For the 'Fractional Photon' method a weight map is created which assigns every pixel in the image a probability p_S to contain a source event. The image of all events is then multiplied with the weight map to receive the image for the reconstructed source counts. As explained earlier, the event list has an additional column which contains a numerical value for every event to indicate if it should be discarded as a non-source event (0) or kept as a source event (1). So to obtain the source counts using the 'Random Removal' technique, only the events with an assigned value of 1 are used to create the image.

Li-Ma Significance

As a second performance metric the significance of the pixel was calculated. To do so we used the calculation from Li and Ma (1983):

$$S = \sqrt{2}\Bigg\{ N_{on}\, ln\left[\frac{1+\alpha}{\alpha}\left(\frac{N_{on}}{N_{on}+N_{off}}\right)\right] + N_{off}\, ln\left[(1+\alpha)\left(\frac{N_{off}}{N_{on}+N_{off}}\right)\right]\Bigg\}^{1/2} \tag{10.13}$$

with $\alpha = t_{on}/t_{off}$, N_{on} the counts during the on-time and N_{off} the counts during the background measurement.

While Li and Ma (1983) used the on-source time t_{on} and the off-source time t_{off} to calculate α, we instead decided to use an on-source region A_{on} and an off-source region A_{off}:

$$\alpha = \frac{A_{on}}{A_{off}} \tag{10.14}$$

Because the calculation needs to be done for every pixel in the image, we are only considering pixels with counts, with this limitation the computational time could be reduced. For the on-source region A_{on} we selected an area around the pixel we want to calculate the significance for with a typical radius of one pixel. For the off-source region A_{off} the area was increased to a radius of two pixels, however only the events laying between r_{on} and r_{off} are considered background counts. After collecting all on-source counts N_{on} and all off-source counts N_{off}, the significance was calculated using Equation (10.13).

11 Test and Analysis

11.1 Proof of Concept

In Section 10.1 the mathematical concepts behind the probabilistic estimator as well as the practical applications of its outputs were discussed, with that in mind, the next chapter should serve as a demonstration of the applicability of the probabilistic estimator using an artificially generated source and background.

X- and Y-coordinates were sampled from a normal distribution, to generate an artificial source. To have sufficient source counts, a total of 50000 pairs of coordinates were created. For creating the artificial background, a similar technique was utilized, but instead of using a normal distribution, the coordinates were drawn from a uniform distribution. Since, the background should cover a wider range of coordinates, a total of 1000000 coordinate pairs were sampled to have sufficient background counts everywhere in the resulting image. Subsequently, the coordinate pairs were used to generate an image with dimensions of 600 pixels in both directions. The resulting images produced by these coordinate pairs can be seen in Figure 11.1a for the source and in Figure 11.1b for the background. The combination of background and source is displayed in Figure 11.1c. For the estimator, Figure 11.1c is used for the overall count k and Figure 11.1b for the estimated expected background μ_N.

Using Equation (10.5) the probabilistic estimator is calculating the μ_S^*-value for every pixel individual using the k- and μ_N-value of the pixels in the corresponding images. After calculating μ_S^*, it can be used with Equation (10.7) to get the probability of the pixels to be associated with a source event and with Equation (10.8) to get the probability to be associated with a background event. As an example, Figure 11.2 shows the probability map to be associated with a source event.

The p_S-Map can then be used with the 'Random Removal' and 'Fractional Photon' technique. First, let's discuss the 'Fractional Photon' technique and its result. To assign every pixel its "fractional photon" we used the p_S-Map from Figure 11.2 as a weight map and multiplied it with the combined image (Figure 11.1c). The resulting image can be seen in Figure 11.3a, in comparison to the Figure 11.1c it is evident

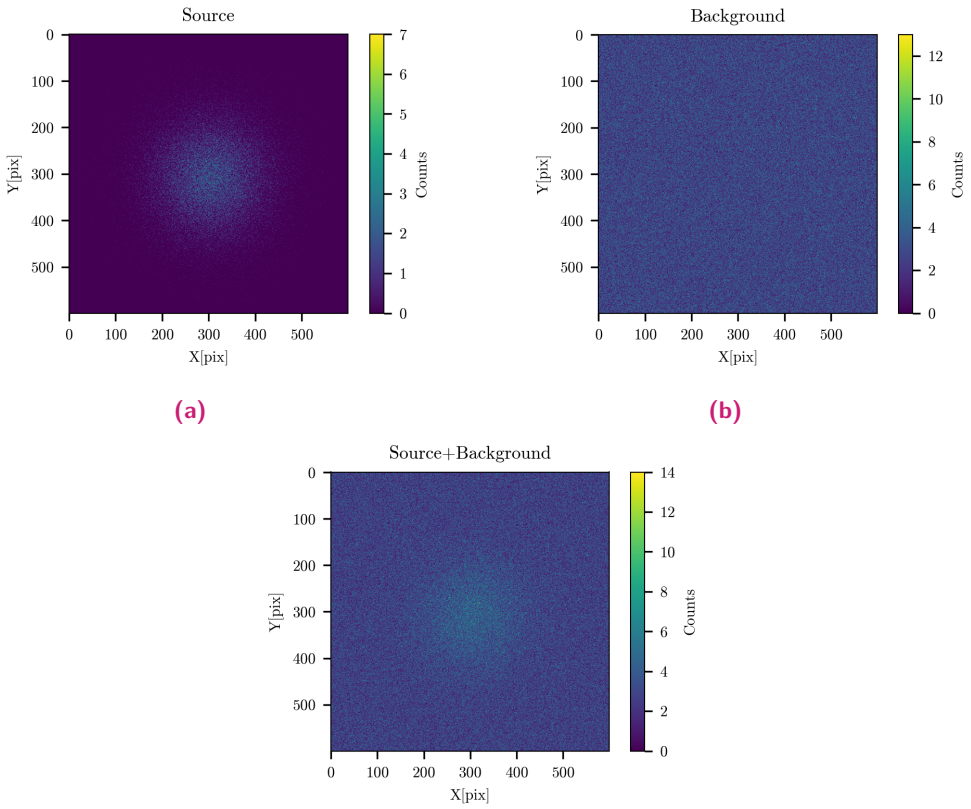

Figure 11.1. – Figure 11.1a is the artifical created source using generalized normal distribution to sample 5×10^4 X/Y-coordinate-pairs. Figure 11.1b is the artifical background generated by sampleing 10^6 X/Y-coordinates from a uniform distribution. Figure 11.1c is the combination of source and background.

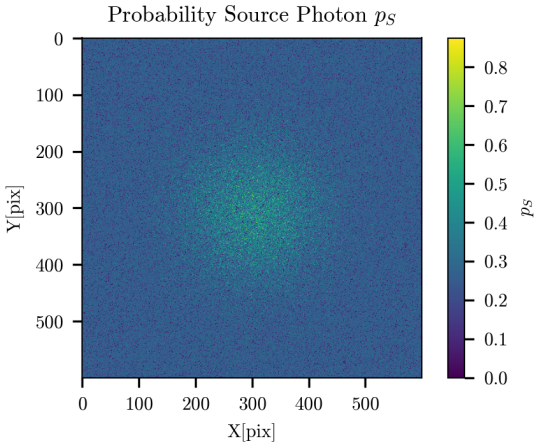

Figure 11.2. – p_S-map calculated from Equation (10.7). Using the expected background μ_N from Figure 11.1b and the estimated expected source count μ_S from Equation (10.5).

that the image from the Fractional Photon technique is less noisy than the combined image and the artificial source in the center is more visible.

In case of the 'Random Removal' technique the random number is drawn for every pixel and then compared with the pixel value in th p_S-map. This creates a matrix containing only 0 (for background events) and 1 (for source events). The combined image (Figure 11.1c) is then multiplied with the matrix. The result of this technique can be seen in Figure 11.4a. In comparison to the combined image, the resulting image from the 'Random Removal' technique contains less noisy pixels, and the source is slightly more prominent. But in comparison to the 'Fractional Photon' technique, it is less distinct.

The last technique we want to compare is the 'Simple Subtraction'. For the 'Simple Subtraction', we calculated the mean pixel value of the background image and then subtracted it from every pixel in the combined image. The resulting image is displayed in Figure 11.5a, there is no change because every value gets reduced by the same amount, however, at the colorbar the present of negative pixel-values are visible. Those negative values are not physical and should be set to zero. Figure 11.6a shows the resulting image if the negative values are set to zero. The resulting image is comparable with the image from the 'Random Removal' technique as it shows also less noisy pixels but in comparison to the 'Fractional Photon' technique, the source is nearly indistinguishable.

Comparing the pixel-values and their occurrence-frequency is also a good way to show the benefits of novel calculation in comparison to the 'Simple Subtraction'. In case of the 'Simple Subtraction' technique, the histogram (Figure 11.5b) shows the downside of this method as the lowest pixel value which occurs is negative. As described before, this can be avoided by setting all negative values to zero (Figure 11.6b), at the cost of information loss.

On the other hand, the histogram for the 'Random Removal' technique (Figure 11.4b) and for the 'Fractional Photon' technique (Figure 11.3b) does not show any negative pixel values, so indeed the new calculation is positive definite.

If the histogram of the 'Fractional Photon' technique is compared with both histograms of the 'Random Removal' technique and the 'Simple Subtraction' technique it also shows that it has fewer zero-value pixels, as this technique does not remove any events outright in comparison to the other two techniques.

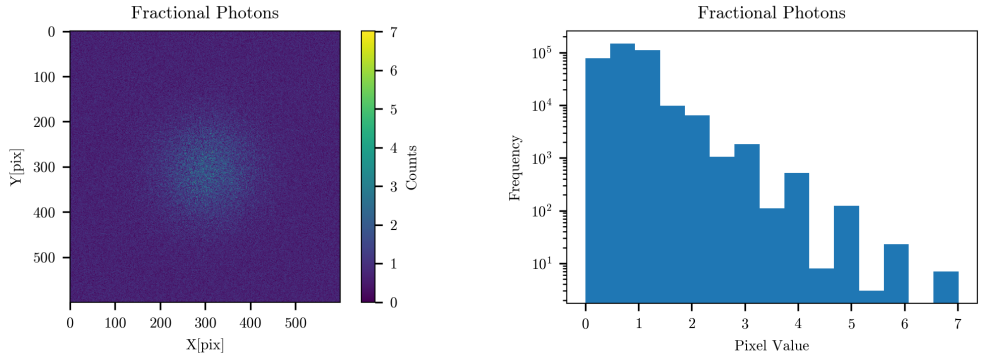

(a) (b)

Figure 11.3. – Figure 11.3a is the resulting image using the 'Fractional Photon' technique and the p_S values from Figure 11.2. Figure 11.3b is the histogram of the pixel-values in Figure 11.3a.

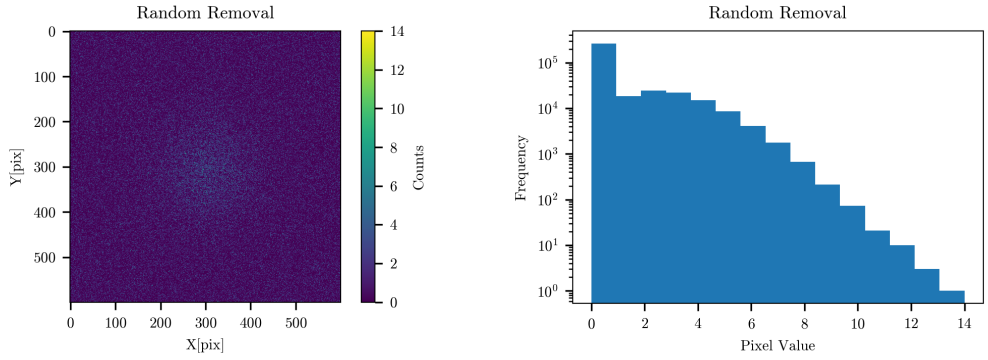

(a) (b)

Figure 11.4. – Figure 11.4a is the result of the 'Random Removal' technique using the p_S values calculated from Equation (10.7). Figure 11.4b is the histogram for the pixel values in Figure 11.4a.

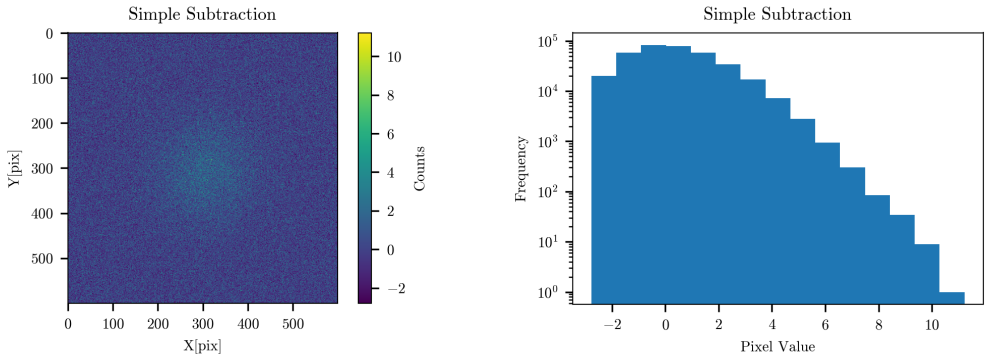

(a) (b)

Figure 11.5. – Figure 11.5a is the resulting image if using the 'Simple Subtraction' technique. Figure 11.5b shows the pixel-values and their frequency in which they occur in Figure 11.5a.

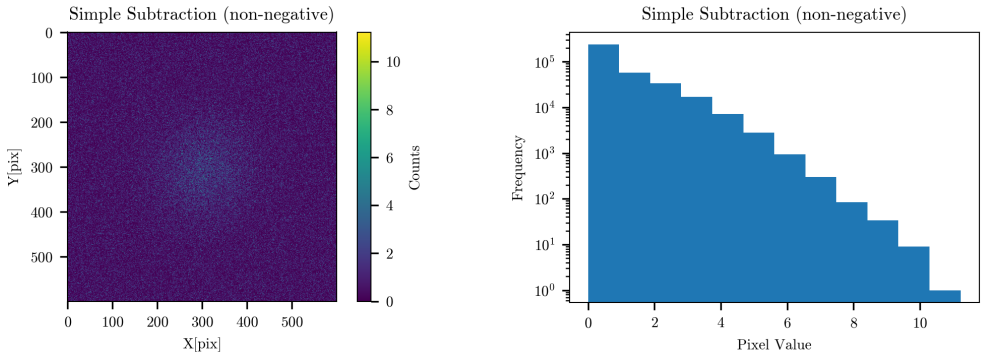

(a) (b)

Figure 11.6. – Figure 11.6a is the result of replacing all negative values with zero. Figure 11.6b is the histogram of pixel values in this case.

In Section 10.1 the concept of the false probability map was also introduced. Even though it is not used as one of the background removal techniques, it was still used with the artificial source. Figure 11.7 shows with Figure 11.7a the probability map to be associated with background events, while Figure 11.7b is the inverse of the probability map. Similar to the background removal techniques the inverse probability maps (Figure 11.7b) shows an increased probability in the center of the image, where the artifical source was placed. The p_N-map on the other hand shows a decrease in the center.

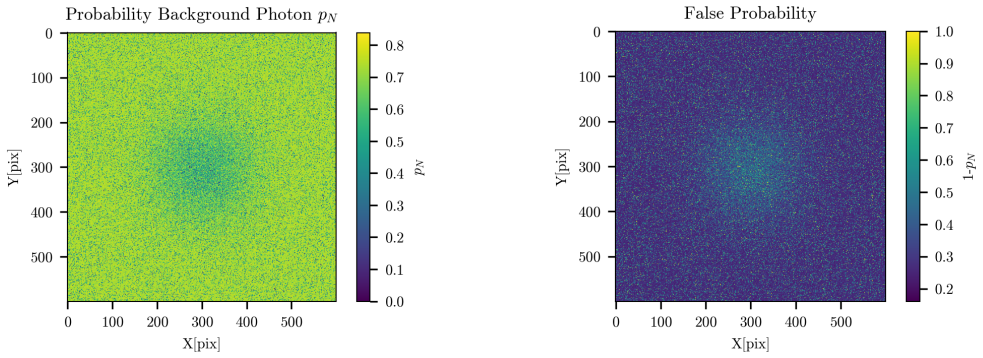

(a) (b)

Figure 11.7. – Figure 11.7a shows the p_N-map calculated from Equation (10.8). The false probability map is shown in Figure 11.7b and calculated by $1 - p_N$, an area of elevated counts is visible which is consistent with the source location.

11.2 Observations

After explaining the mathematical concept of the probabilistic estimator in Section 10.1 and applying the method on an artificial source in Section 11.1, it is now time to apply those methods on real data to examine their performance. In order to do so, four different observations were selected and processed, so the estimator can be applied. The four observations include a variety of different astrophysical sources, most of them point-like sources, but we also included extended sources. The following paragraphs are introducing the selected observation first, before continuing to the single source analysis.

ObsID_0504810301: The observation with the ID 0504810301 was done on August 25, 2007 between 2:49 and 23:34 for a duration of around 75 ks. The target of this observation was the supernova remnant shell RCW86 NW (RA: 14h 41m 59.42s, DEC: -62d 13' 00.9") (Rodgers et al., 1960), which is frequently identified as part of the supernova remnant Cen X-1 or at least interacting with it. This observations, was selected since its diffuse structure covers a great part of the CCD in addition to that, some faint "filaments" are visible which offer an opportunity to test if the method shows any improvement in comparison to the normal clean-up.

ObsID_0743850101: The galaxy cluster merger A2744 (RA: 00h 14m 20.00s, DEC: -30d 23' 18.0") (Eckert et al., 2016) was observed by XMM-Newton between December 18th 2014 (19:09) and December 20th 2014 (2:14) for around 100 ks. Its observation ID is 0743850101 and it was selected due to its extended source in the center of the CCD, which is many times brighter than RCW86.

ObsID_0932200801: Since the method should not be exclusively tested on extended sources the observation with the ID 0932200801 was selected to test it also on point-like sources. The target of this observation was a part of the galactic plane around RA: 17h 53m 12.02s DEC: -25d 29' 02.3". XMM-Newton observed it on October 2nd 2023 between 1:15 and 7:38 for a total of 23 ks.

ObsID_0804300501: The last observation which was used has the ID 0804300501. The observation was done between March 25th 2018 (3:27) and March 26th 2018 (15:21) for a total of $\sim 129\,\mathrm{ks}$. The target of this observation was a part of the supernova remnant RX J1713.7-3946 (Pfeffermann and Aschenbach, 1996). First

the idea was to use this observation to study another supernova remnant, but this was discarded in the course of the analysis, instead one of the bright sources visible in the observation was selected for further analysis.

11.3 Single Source Analysis

After the short introduction of the four observations from which sources were picked, it is time to introduce the sources and report on the finding after applying the different removal techniques. To cover a wide variety of different sources, we decided to use two faint and two bright point-like sources as well as one bright and one faint extended source. The result of the analysis for every individual source is listed in the following section as well as in the summary table (Table 11.2).

A2744: A2744 is an X-ray bright merged cluster of galaxies (Eckert et al., 2016). It is the central-observed object in the observation with the observation ID 0743850101 (Figure 11.8). The selection of circular region with a radius of 41 pixels around the most prominent features of the cluster resulted in a surface brightness of $32.24 \pm 0.078\,\mathrm{counts\,pixels}^{-2}$ in case of the original event list. In all three cases of background removal, a slight decrease in surface brightness could be seen. For the Fractional Photon method, it decreased to $27.71 \pm 0.072\,\mathrm{counts\,pixels}^{-2}$ whereas for the Random Removal technique it decreased to $27.73 \pm 0.072\,\mathrm{counts\,pixels}^{-2}$. In case of a simple subtraction, the surface brightness is found to be $27.03 \pm 0.071\,\mathrm{counts\,pixels}^{-2}$. The Signal-to-noise ratio calculation described in Section 10.3 in conjunction with the identical region as in the measurement for the surface brightness, resulted in a SNR for the 'Simple Subtraction', 'Fractional Photon' and 'Random Removal' technique of $4.38(53)$, $4.49(50)$, and $4.50(50)$ respectively. Therefore, the 'Fractional Photon' method improved the result by 2.7% while 'Random removal' showed an improvement of 2.8%. In addition to the SNR, the significance was also calculated as outlined in Section 10.3. From the original event list, the significance of A2744 was determined to be 5.78σ. With regard to the other three methods, it is observed that the significance decreases in the following order: first 'Fractional Photons' and 'Random Removal' to 5.29σ each and second 'Simple Subtraction' to 5.19σ.

RCW 86 Filaments: A2744 was one of the extended sources which were used as a testing ground for the novel methods. However, given the brightness of A2744, it would be also appropriate to test the methods on fainter object. For that purpose, a

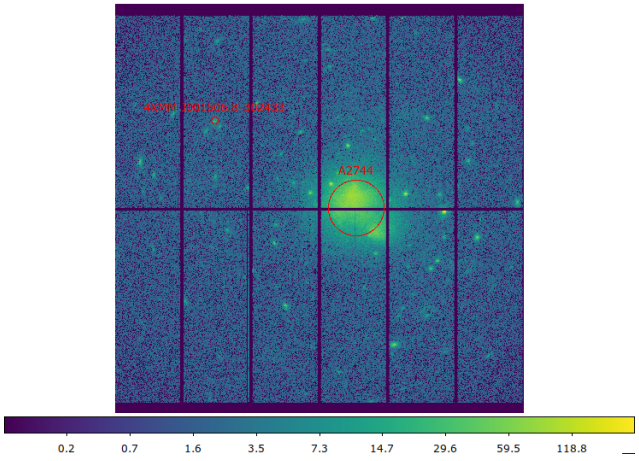

Figure 11.8. – Image of observation 0743850101 in detector coordinates and a logarithmic scale with the galaxy cluster merger A2744 in the center. The circular region with a radius of 41 pixels around the source is also used in the following analysis steps. 4XMM J001506.8-302433 is the other source analysed from this observation, in this case, a circle with a radius of 5 pixels was used.

part of the supernova remnant RCW86 (Rodgers et al., 1960) was selected, especially a small part on the outer edge of the supernova remnant with fine "filaments" as seen in Figure 11.9. The image of the event list showed that the filaments had a surface brightness of $6.63 \pm 0.03\,\mathrm{counts\,pixels^{-2}}$, while in the other cases it decreased to $4.31 \pm 0.03\,\mathrm{counts\,pixels^{-2}}$ ('Fractional Photons'), $4.30 \pm 0.03\,\mathrm{counts\,pixels^{-2}}$ ('Random Removal') and $3.35 \pm 0.02\,\mathrm{counts\,pixels^{-2}}$ ('Simple Subtraction'). The significance was the highest for the event list with 2.72σ followed by 'Random Removal' and 'Fractional Photons' with 2.16σ each and 'Simple Subtraction' with 1.87σ. The SNR for 'Fractional Photons' ended up to be $1.61(53)$ and for 'Random Removal' $1.61(49)$, while for the 'Simple Subtraction' the SNR was $1.24(53)$. In the case of those faint "filaments", 'Fractional Photons' as well as 'Random Removal' showed an improvement of 31% compared to the 'Simple Subtraction'.

4XMM J175337.3-253241: 4XMM J175337.3-253241 (hereafter J175337) is one of the sources in observation 0932200801, which was selected for further investigation. The object is a rather faint source (as seen in Figure 11.10), with a flux in the 0.2–$12\,\mathrm{keV}$ energy range of $(8.49 \pm 3.63) \times 10^{-15}\mathrm{erg\,s^{-1}\,cm^{-2}}$ as denoted in the 4XMM-DR14 Catalogue (Webb et al., 2023). J175337 had a surface brightness of $0.95 \pm 0.11\,\mathrm{counts\,pixels^{-2}}$, $0.64 \pm 0.09\,\mathrm{counts\,pixels^{-2}}$, $0.62 \pm 0.09\,\mathrm{counts\,pixels^{-2}}$ and $0.43 \pm 0.07\,\mathrm{counts\,pixels^{-2}}$ for the original event list, 'Fractional Photons', 'Random Removal', and 'Simple Subtraction', respectively. The SNR for J175337 was $0.54(20)$ ('Fractional Photons'), $0.53(10)$ ('Random Removal') and $0.36(40)$ ('Simple

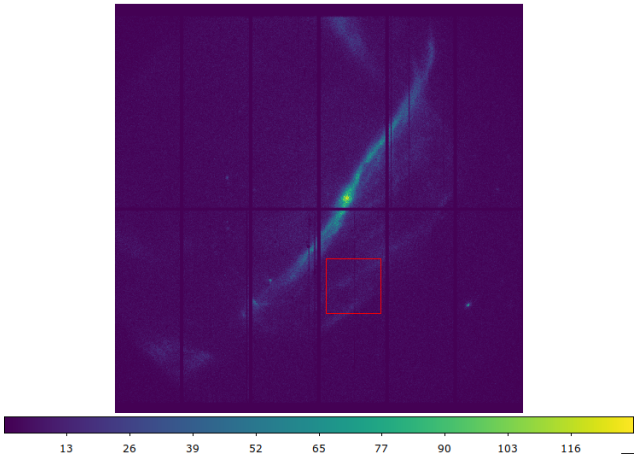

Figure 11.9. – Image of observation 0504810301 in detector coordinates and a linear scale. It shows the north-west part of the supernova remnant RCW 86. The red box shows the area which contains some faint filamnents of the supernova remnant which was selected for further studies.

Subtraction'). In comparison to the 'Simple Subtraction', the 'Fractional Photon' method was able to improve the SNR by 49% and the 'Random Removal' technique by 47%. For J175337 the significance for the methods was 0.98σ (original event list), 0.78σ ('Fractional Photons'), 0.77σ ('Random Removal') and 0.62σ ('Simple Subtraction').

4XMM J175304.3-253449: The other object in observation 0932200801, which was also selected for further studies is 4XMM J175304.3-253449 (hereafter J175304), which is a bright source (as seen in Figure 11.10) in comparison to J175337 with a flux of $(4.68 \pm 1.30) \times 10^{-13}\,\mathrm{erg\,s^{-1}\,cm^{-2}}$. The image derived from the original event list, reveals that J175304 had a surface brightness of $2.54 \pm 0.18\,\mathrm{counts\,pixels^{-2}}$. For the 'Fractional Photons', 'Random Removal' and 'Simple Subtraction' J175304 showed a surface brightness of $1.92 \pm 0.16\,\mathrm{counts\,pixels^{-2}}$, $1.95 \pm 0.16\,\mathrm{counts\,pixels^{-2}}$ and $1.54 \pm 0.14\,\mathrm{counts\,pixels^{-2}}$ respectively. In the case of J175304, the SNR-value was determined to be $1.05(38)$ for the 'Fractional Photon' method, $1.06(31)$ for 'Random Removal' and $0.88(53)$ for the 'Simple Subtraction'. In conclusion, the 'Fractional Photons' and the 'Random removal' improved the SNR by 20% compared to the 'Simple Subtraction'. The significance in the case of J175304, was the highest for the original event list with 1.64σ followed by 'Random Removal' with 1.41σ and 'Fractional Photon' with 1.40σ the lowest significance showed the 'Simple Subtraction' with 1.26σ.

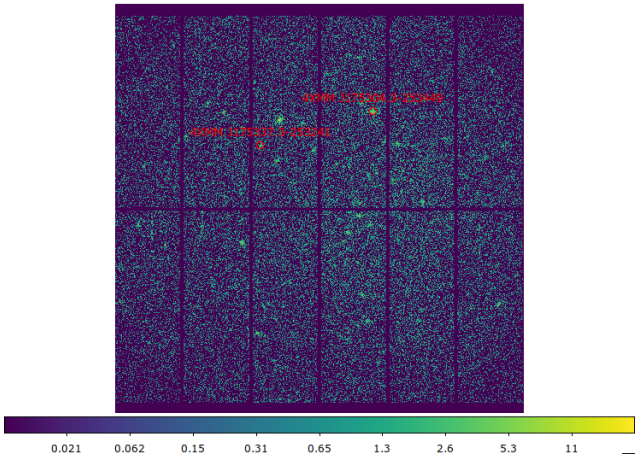

Figure 11.10. – Image of observation 0932200801 in detector coordinates and a logarithmic scale. 4XMM J175337.3-253241 and 4XMM J175304.3-253449 were selected for further analysis. In both cases, the circle around the sources has a radius of 5 pixels.

4XMM J171339.1-392659: The X-ray emitting star 4XMM J171339.1-392659 (hereafter J171339) (Lin et al., 2012) is another bright point-like source with a flux of $(2.050 \pm 0.26) \times 10^{-13}\,\mathrm{erg\,s^{-1}\,cm^{-2}}$ in the energy-range of 0.2–$12\,\mathrm{keV}$. This source had a surface-brightness of $37.14 \pm 0.68\,\mathrm{counts\,pixels^{-2}}$ and a significance of 6.14σ in case of the event list, while for the 'Fractional Photon' method this decreased to $32.16 \pm 0.63\,\mathrm{counts\,pixels^{-2}}$ and 5.64σ respectively. For the 'Random Removal', it decreased further to $32.11 \pm 0.63\,\mathrm{counts\,pixels^{-2}}$ and 5.62σ. The 'Simple Subtraction method' showed the lowest values with $30.04 \pm 0.61\,\mathrm{counts\,pixels^{-2}}$ and 5.54σ. While in the analysis of the other sources, it was found that the 'Simple Subtraction' typically exhibits the lowest SNR this was not the case for J171339. Here, the 'Random Removal' has the lowest SNR of $4.514(444)$, followed by the 'Simple Subtraction' with $4.526(518)$ and 'Fractional Photon' with $4.527(449)$. Whereas this was an marginal improvement of 0.01% for the 'Fractional Photon', it was a degradation of 0.27% for the 'Random Removal' in comparison to the 'Simple Subtraction'.

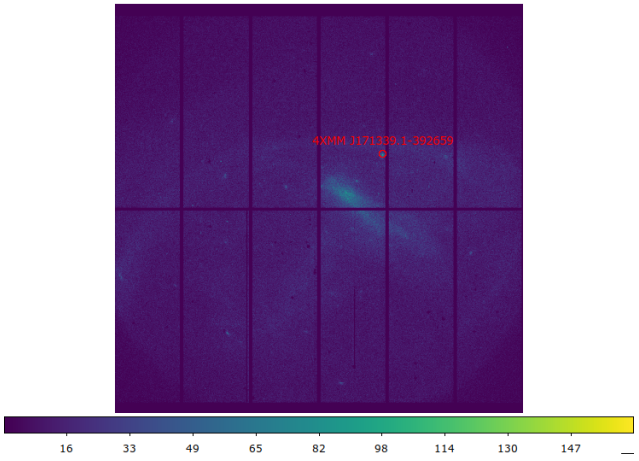

Figure 11.11. – Image of observation 0804300501 in detector coordinates and a linear scale. Encircled in red is the point-like source 4XMM J171339.1-392659.

4XMM J001506.8-302433: The Quasar 4XMM J001506.8-302433 (hereafter J001506) (Véron-Cetty and Véron, 2010) is a low luminosity source in comparison to other sources analysed in this section, with a flux of $7.53 \pm 0.86 \times 10^{-14}\,\mathrm{erg\,s^{-1}\,cm^{-2}}$ in the 0.2–$12\,\mathrm{keV}$ range. Its surface brightness, in case of the image created from the original event list, was $11.00 \pm 0.38\,\mathrm{counts\,pixels^{-2}}$ and it showed a significance of 3.47σ. In the image of the 'Fractional Photon' it showed a surface brightness of $6.49 \pm 0.29\,\mathrm{counts\,pixels^{-2}}$ and a significance of 2.56σ while for the 'Random Removal' it was $6.45 \pm 0.29\,\mathrm{counts\,pixels^{-2}}$ and 2.53σ. The outcome of the 'Simple Subtraction' was a significance of 2.29σ and a surface brightness of $5.20 \pm 0.26\,\mathrm{counts\,pixels^{-2}}$. The 'Fractional Photon' method showed the highest SNR with $1.69(50)$, followed by 'Random Removal' with $1.66(45)$ and 'Simple Subtraction' with $1.41(50)$. In comparison to the 'Simple Subtraction', 'Fractional Photon' enhanced the SNR by 20% and 'Random Removal' by 18%.

J001506 was also used to validate the usability of the probabilistic background method. As the previous results suggested, that the 'Fractional Photon' as well as the 'Random Removal' method might yield better results in a comparison to the 'Simple Subtraction'. For that, we compared the aforementioned methods for one single source with an alternative subtraction method. However, in this method rather than extracting the expected background from the stacked image, a region is selected using the XMM-SAS task **ebkgreg**. The necessary inputs for **ebkreg** are the source location as well as an image, and the result of this task is then a region that is recommended by the algorithm to utilise as the background region. The mean pixel-value of the recommended region is then used as the local background.

This process was repeated for each energy band and the results can be seen in Table 11.1.

Subsequently, the local background levels were subtracted from the images generated by the event list. The subtraction of local background resulted in a Surface-Brightness for J001506 of $8.82 \pm 0.34\,\mathrm{counts\,pixels}^{-2}$, a significance of 3.12σ and a SNR of $2.54(56)$.

Energy-Band	mean pixel value
low	0.160
CXB Internal 1	0.359
AlK	0.157
CXB Internal 2	0.677
NiCuZn	0.438
CXB Internal 3	0.192

Table 11.1. – Energy-bands and their mean pixel-values which were used as local background levels .

Methods	Surface Brightness (in $\frac{\text{counts}}{\text{pixels}^2}$)	Significance (in σ)	Signal-to-noise ratio	Improvement (in %)
A2744				
Fractional Photons	27.71 ± 0.072	5.29	4.49(50)	2.7
Random Removal	27.73 ± 0.072	5.29	4.50(50)	2.8
Simple Subtraction	27.03 ± 0.071	5.19	4.38(53)	
RCW 86 Filaments				
Fractional Photons	4.31 ± 0.03	2.16	1.61(53)	31
Random Removal	4.30 ± 0.03	2.16	1.61(49)	31
Simple Subtraction	3.35 ± 0.02	1.87	1.24(53)	
4XMM J175337.3-253241				
Fractional Photons	0.64 ± 0.09	0.78	0.54(20)	49
Random Removal	0.62 ± 0.09	0.77	0.53(10)	47
Simple Subtraction	0.43 ± 0.07	0.62	0.36(40)	
4XMM J175304.3-253449				
Fractional Photons	1.92 ± 0.16	1.40	1.05(38)	20
Random Removal	1.95 ± 0.16	1.41	1.06(31)	20
Simple Subtraction	1.54 ± 0.14	1.26	0.88(53)	
4XMM J171339.1-392659				
Fractional Photons	32.16 ± 0.63	5.64	4.527(449)	0.01
Random Removal	32.11 ± 0.63	5.62	4.514(444)	-0.27
Simple Subtraction	30.04 ± 0.61	5.54	4.526(518)	

4XMM J001506.8-302433				
Fractional Photons	6.49 ± 0.29	2.56	1.69(50)	20
Random Removal	6.45 ± 0.29	2.53	1.66(45)	18
Simple Subtraction	5.20 ± 0.26	2.29	1.41(50)	
Local Simple Subtraction	8.82 ± 0.34	3.12	2.54(56)	

Table 11.2. – Summary table of the source analysis to compare the different background removal techniques. The table includes the surface brightness of the source for all techniques as well as the significance of the detection and the Signal-to-noise ratio of the image. The last column shows the improvment of the two novel methods in respect to the 'Simple Subtraction'.

12 Conclusion

In this part of the thesis, we combined the probabilistic background removal technique proposed by Ehlert et al. (2022) and the exposure-corrected stacked images, which can be used to estimate the expected background rate, to reduce the background in XMM-Newton observations. As seen in the last chapter, the 'Fractional Photon' method as well as the 'Random Removal' method have advantages in comparison to the 'Simple Subtraction' method, provided that the expected background counts are derived from the stacked image. However, compared to results from the background subtraction using a local area around the source which should be analyzed (which is usually done), neither the 'Fractional Photon' method nor the 'Random Removal' method show any discernible improvements. On the other hand, using the local background, requires the careful manual selection for every source individually. This is not necessary for 'Fractional Photons' and 'Random Removal', as these are solely dependent on the exposure-corrected stacked images. It was also demonstrated that the performance gain for bright sources is marginal and in some cases (4XMM J171339.1-392659) even absent. This was as expected, as explained in Section 10.1 both techniques show diminishing return and higher computation times in the high-count regime, in comparison to the 'Simple Subtraction'. However, for faint sources (e.g. 4XMM J175337.3-253241), this probabilistic method can prove useful especially for source identification. While this method might not surpass the results of already established algorithms in pointing instruments like XMM-Newton, it might present a valuable addition for faint source detection in future telescopes.

Acknowledgement

This work made use of Astropy:[1] a community-developed core Python package and an ecosystem of tools and resources for astronomy (Astropy Collaboration et al., 2013, 2018, 2022). In addition to Astropy this work used a wide variety of different python modules, including NumPy (Harris et al., 2020), SciPy(Virtanen et al., 2020), Matplotlib (Hunter, 2007) as well as different modules from the astroquery package Ginsburg et al. (2019). The finding charts were created with the help of hips2fits,[2] a service provided by CDS and NASA's *SkyView* facility (http://skyview.gsfc.nasa.gov) located at NASA Goddard Space Flight Center.

This work highly benefitted from the SIMBAD database, operated at CDS, Strasbourg, France, as well as from the VizieR catalogue access tool, CDS, Strasbourg Astronomical Observatory, France (Ochsenbein et al., 2000) in order to access source information and instrument catalogues. Additionally, this work made use of data and software facilities provided by the High Energy Astrophysics Science Archive Research Center (HEASARC), a service provided by the Astrophysics Science Division at NASA/GSFC.

In the infrared wavelength, this research made use of data products from the Two Micron All Sky Survey, which is a joint project of the University of Massachusetts and the Infrared Processing and Analysis Center/California Institute of Technology, funded by the National Aeronautics and Space Administration, and the National Science Foundation.

Further, the data products from the Wide-field Infrared Survey Explorer (Wright et al., 2010) is used for this work, which is a joint project of the University of California, Los Angeles, and the Jet Propulsion Laboratory/California Institute of Technology, funded by the National Aeronautics and Space Administration as well as data products from NEOWISE (Mainzer et al., 2011), which is a project of the Jet Propulsion Laboratory/California Institute of Technology, funded by the Planetary Science Division of the National Aeronautics and Space Administration.

The work carried out in the optical wavelength, this work has made use of data from the European Space Agency (ESA) mission *Gaia* (`https://www.cosmos.`

[1] http://www.astropy.org
[2] https://alasky.cds.unistra.fr/hips-image-services/hips2fits

esa.int/gaia), processed by the *Gaia* Data Processing and Analysis Consortium (DPAC, https://www.cosmos.esa.int/web/gaia/dpac/consortium). Funding for the DPAC has been provided by national institutions, in particular the institutions participating in the *Gaia* Multilateral Agreement.

The X-ray analysis in this research is based on observations obtained with XMM-Newton, an ESA science mission with instruments and contributions directly funded by ESA Member States and NASA. Data was obtained from the 4XMM XMM-Newton serendipitous source catalogue compiled by the XMM-Newton Survey Science Centre consortium. In addition to XMM-Newton this research has made use of data obtained from the Chandra Source Catalog, provided by the Chandra X-ray Center (CXC) and data supplied by the UK Swift Science Data Centre at the University of Leicester.

Parts of this Thesis are based on observations with INTEGRAL, and ESA project with instruments and science data centre funded by ESA member states (especially the PI countries: Denmark, France, Germany, Italy, Switzerland, Spain), and Poland, and with the participation of Russia and the USA.

Research is something we do together, therefore, I would like to express my appreciation to people who have helped me along this journey.

First and foremost, I wish to thank Prof. Dott. Andrea Santangelo who welcomed me in his group, gave me the possibility to work on this thesis and helped with scientific questions. I thank Prof. Dr. Klaus Werner for reviewing my thesis. I extend my thank to Prof. Dr. Josef Jochum and PD. Dr. Christoph Schäfer who agreed to be part of my PhD committee.

My deepest gratitude goes to my two supervisors Victor Doroshenko, and Youli Tuo who shaped my scientific career, whose offices I was always welcome in, and for always supporting me.

Thank you, Ritika for proofreading my thesis, sharing snacks, Spezi and, the delicious meals with me. Also for our runs together with me in my Zone 2 and you in your Zone 4.

I thank Bastian for supporting my triathlon ambitions and our bikes rides. Thank you, Mariachiara for joining the triathlon team, for the running t(r)ips and for encouraging me to participate in the faster heat of the Erbe Lauf.

I also thank Thomas and Chris, for your continuous support in scientific questions, the lectures about digital electronics, our bike adventures, and all the delicious cake.

Thank you, Christian for always helping me with my questions about XMM-Newton and helping me survive the forest of PhD bureaucracy. Another thanks go to Paul, Sam and Xianqi, for our nice weekend-trips, the awesome Skiing-trips and the Biergarten-Tuesdays on a Friday.

To Charles, for helping me polish my English language skills, our gaming sessions, the help during my Scotland vacation and most importantly our Edeka adventures ('Edeka mit dir war so geil').

Thank you, Nhan for nice conversations, and recommendations for my Japan vacation and awesome PhD and cat memes.

I also thank Sabine Lauer, for all you help in the jungle of bureaucracy (in and around the institute), for our nice conversations, and all the help you provided not only during the Christmas party.

Thanks Christoph for all your silly comments, and your support for the A&A tutoring and the nice time at the Universe on Tour in Reutlingen.

Thank you, Radu for always being very helpful with problems in and around our offices and for receiving some of my parcels which otherwise would have ended up in some DHL station.

I want to thank all the long-lasting members of the office A125 (Moritz, Leon, Atul, Charles, Ritika, Shuaitongze, Pano, Joachim, Tim), I really enjoyed working with all of you in this office, you made this a warm and crazy place.

I would like to mention other people who made these years a pleasant journey and the institute a wonderful place: Artur, Jonas, Lorenzo, Alejandro, Roisin, Alexej, Enza, Heiko, Inga, Camille, Leon, Mirjam, Wilhelmina, Anto and Fabian.

To my friends, Simon, Marc, Paula and Sarah for supporting me since High School. To my fellow colleagues Maggie, Dr. Lena, Sina, Marie, Lukas, Arne, Thomas and Paul with whom I had a pleasure to study together.

I would specially like to thank all my siblings for their continuous support, and for all the memories we have shared since you came into my life, and for the memories we will make in the future. I am so grateful that I have you all in my life.

Last, but not the least, my biggest thanks goes to Axel (my father), and to (my "bonus"-mother) Sabine for their unconditional love, and guidance throughout my life. I am truly lucky to have such extremely supportive parents.

> *Take my hand, there's so much more to see way up high in a distant galaxy*

— **Sefa**
(Infinity)

Bibliography

F. Anders, A. Khalatyan, A. B. A. Queiroz, et al. Photo-astrometric distances, extinctions, and astrophysical parameters for Gaia EDR3 stars brighter than G = 18.5. *A&A*, 658:A91, 2022. URL http://dx.doi.org/10.1051/0004-6361/202142369.

Astropy Collaboration, A. M. Price-Whelan, B. M. Sipőcz, et al. The Astropy Project: Building an Open-science Project and Status of the v2.0 Core Package. *AJ*, 156(3):123, 2018. URL http://dx.doi.org/10.3847/1538-3881/aabc4f.

Astropy Collaboration, Adrian M. Price-Whelan, Pey Lian Lim, et al. The Astropy Project: Sustaining and Growing a Community-oriented Open-source Project and the Latest Major Release (v5.0) of the Core Package. *ApJ*, 935(2):167, 2022. URL http://dx.doi.org/10.3847/1538-4357/ac7c74.

Astropy Collaboration, T. P. Robitaille, E. J. Tollerud, et al. Astropy: A community Python package for astronomy. *A&A*, 558:A33, 2013. URL http://dx.doi.org/10.1051/0004-6361/201322068.

A. Avakyan, M. Neumann, A. Zainab, V. Doroshenko, J. Wilms, and A. Santangelo. XRBcats: Galactic low-mass X-ray binary catalogue. *A&A*, 675:A199, 2023. URL http://dx.doi.org/10.1051/0004-6361/202346522.

A. Avakyan, A. Zainab, V. Doroshenko, J. Wilms, A. Schwope, V. Suleimanov, D. Buckley, J. Brink, and A. Santangelo. XMM-Newton follow-up of two eROSITA X-ray binary candidates. *Experimental Astronomy*, 60(1):6, 2025. URL http://dx.doi.org/10.1007/s10686-025-10016-w.

V. S. Avedisova. A Catalog of Star-Forming Regions in the Galaxy. *Astronomy Reports*, 46(3):193–205, 2002. URL http://dx.doi.org/10.1134/1.1463097.

Arash Bahramian and Nathalie Degenaar. Low-Mass X-ray Binaries. In *Handbook of X-ray and Gamma-ray Astrophysics*, page 120. 2023. URL http://dx.doi.org/10.1007/978-981-16-4544-0_94-1.

C. A. L. Bailer-Jones, J. Rybizki, M. Fouesneau, M. Demleitner, and R. Andrae. Estimating Distances from Parallaxes. V. Geometric and Photogeometric Distances

to 1.47 Billion Stars in Gaia Early Data Release 3. *AJ*, 161(3):147, 2021. URL http://dx.doi.org/10.3847/1538-3881/abd806.

Max Camenzind. *Compact objects in astrophysics : white dwarfs, neutron stars, and black holes*. 2007. URL http://dx.doi.org/10.1007/978-3-540-49912-1.

Sergio Campana and Tiziana Di Salvo. Accreting Pulsars: Mixing-up Accretion Phases in Transitional Systems. In Luciano Rezzolla, Pierre Pizzochero, David Ian Jones, Nanda Rea, and Isaac Vidaña, editors, *Astrophysics and Space Science Library*, volume 457 of *Astrophysics and Space Science Library*, page 149. 2018. URL http://dx.doi.org/10.1007/978-3-319-97616-7_4.

J. A. Carter and A. M. Read. The XMM-Newton EPIC background and the production of background blank sky event files. *A&A*, 464(3):1155–1166, 2007. URL http://dx.doi.org/10.1051/0004-6361:20065882.

J. A. Carter and S. Sembay. Identifying XMM-Newton observations affected by solar wind charge exchange. Part I. *A&A*, 489(2):837–848, 2008. URL http://dx.doi.org/10.1051/0004-6361:200809997.

Sylvain Chaty. *Accreting Binaries; Nature, formation, and evolution*. 2022. URL http://dx.doi.org/10.1088/2514-3433/ac595f.

T. E. Cravens. Comet Hyakutake x-ray source: Charge transfer of solar wind heavy ions. *Geophys. Res. Lett.*, 24(1):105–108, 1997. URL http://dx.doi.org/10.1029/96GL03780.

A. De Luca and S. Molendi. The EPIC/MOS view of the 2-8 keV Cosmic X-ray Background Spectrum. *arXiv e-prints*, astro-ph/0402233, 2004. URL http://dx.doi.org/10.48550/arXiv.astro-ph/0402233.

J. W. den Herder, A. C. Brinkman, S. M. Kahn, et al. The Reflection Grating Spectrometer on board XMM-Newton. *A&A*, 365:L7–L17, 2001. URL http://dx.doi.org/10.1051/0004-6361:20000058.

D. Eckert, M. Jauzac, F. Vazza, M. S. Owers, J. P. Kneib, C. Tchernin, H. Intema, and K. Knowles. A shock front at the radio relic of Abell 2744. *MNRAS*, 461(2):1302–1307, 2016. URL http://dx.doi.org/10.1093/mnras/stw1435.

S. Ehlert, C. T. Chen, D. Swartz, R. C. Hickox, A. Lutovinov, A. Semena, R. Krivonos, A. Shtykovsky, and A. Tkachenko. A probabilistic method of background removal for high energy astrophysics data. *MNRAS*, 515(4):5185–5197, 2022. URL http://dx.doi.org/10.1093/mnras/stac2072.

ESA: XMM-Newton SOC. *XMM-Newton Users Handbook, Issue 2.23, 2025*, 2025. URL https://xmm-tools.cosmos.esa.int/external/xmm_user_support/documentation/uhb/.

Ian N. Evans, Janet D. Evans, J. Rafael Martínez-Galarza, et al. The Chandra Source Catalog Release 2 Series. *ApJS*, 274(2):22, 2024. URL http://dx.doi.org/10.3847/1538-4365/ad6319.

P. A. Evans, K. L. Page, J. P. Osborne, et al. 2SXPS: An Improved and Expanded Swift X-Ray Telescope Point-source Catalog. *ApJS*, 247(2):54, 2020. URL http://dx.doi.org/10.3847/1538-4365/ab7db9.

Michael J. Freyberg, Ulrich G. Briel, Konrad Dennerl, Frank Haberl, Gisela D. Hartner, Elmar Pfeffermann, Eckhard Kendziorra, Marcus G. F. Kirsch, and David H. Lumb. EPIC pn-CCD detector aboard XMM-Newton: status of the background calibration. In Kathryn A. Flanagan and Oswald H. W. Siegmund, editors, *X-Ray and Gamma-Ray Instrumentation for Astronomy XIII*, volume 5165 of *Society of Photo-Optical Instrumentation Engineers (SPIE) Conference Series*, pages 112–122. 2004. URL http://dx.doi.org/10.1117/12.506277.

Gaia Collaboration, T. Prusti, J. H. J. de Bruijne, et al. The Gaia mission. *A&A*, 595:A1, 2016. URL http://dx.doi.org/10.1051/0004-6361/201629272.

Gaia Collaboration, A. Vallenari, A. G. A. Brown, et al. Gaia Data Release 3. Summary of the content and survey properties. *A&A*, 674:A1, 2023. URL http://dx.doi.org/10.1051/0004-6361/202243940.

M. Gilfanov. Low-mass X-ray binaries as a stellar mass indicator for the host galaxy. *MNRAS*, 349(1):146–168, 2004. URL http://dx.doi.org/10.1111/j.1365-2966.2004.07473.x.

Adam Ginsburg, Brigitta M. Sipőcz, C. E. Brasseur, et al. astroquery: An Astronomical Web-querying Package in Python. *AJ*, 157(3):98, 2019. URL http://dx.doi.org/10.3847/1538-3881/aafc33.

T. Gold. Rotating Neutron Stars as the Origin of the Pulsating Radio Sources. *Nature*, 218(5143):731–732, 1968. URL http://dx.doi.org/10.1038/218731a0.

Andrea Goldwurm and Aleksandra Gros. Coded Mask Instruments for Gamma-Ray Astronomy. In Cosimo Bambi and Andrea Sangangelo, editors, *Handbook of X-ray and Gamma-ray Astrophysics*, page 15. 2022. URL http://dx.doi.org/10.1007/978-981-16-4544-0_44-1.

H. J. Grimm, M. Gilfanov, and R. Sunyaev. High-mass X-ray binaries as a star formation rate indicator in distant galaxies. *MNRAS*, 339(3):793–809, 2003. URL http://dx.doi.org/10.1046/j.1365-8711.2003.06224.x.

Alice K. Harding. Physics in Ultra-Strong Magnetic Fields. In Eleonora Troja and Matthew G. Baring, editors, *Neutron Star Astrophysics at the Crossroads: Magnetars and the Multimessenger Revolution*, volume 363 of *IAU Symposium*, pages 149–161. 2023. URL http://dx.doi.org/10.1017/S1743921322000886.

Charles R. Harris, K. Jarrod Millman, Stéfan J. van der Walt, et al. Array programming with NumPy. *Nature*, 585(7825):357–362, 2020. URL http://dx.doi.org/10.1038/s41586-020-2649-2.

A. Hewish, S. J. Bell, J. D. H. Pilkington, P. F. Scott, and R. A. Collins. Observation of a Rapidly Pulsating Radio Source. *Nature*, 217(5130):709–713, 1968. URL http://dx.doi.org/10.1038/217709a0.

J. D. Hunter. Matplotlib: A 2d graphics environment. *Computing in Science & Engineering*, 9(3):90–95, 2007. URL http://dx.doi.org/10.1109/MCSE.2007.55.

F. Jansen, D. Lumb, B. Altieri, et al. XMM-Newton observatory. I. The spacecraft and operations. *A&A*, 365:L1–L6, 2001. URL http://dx.doi.org/10.1051/0004-6361:20000036.

H. Katayama, I. Takahashi, Y. Ikebe, K. Matsushita, and M. J. Freyberg. Properties of the background of EPIC-pn onboard XMM-Newton. *A&A*, 414:767–776, 2004. URL http://dx.doi.org/10.1051/0004-6361:20031687.

Marcus G Kirsch, Anders Elfving, Rainer Kresken, et al. Extending the lifetime of esa's x-ray observatory xmm-newton. In *SpaceOps 2014 Conference*, page 1608. 2014.

Peter Kretschmar, Felix Fürst, Lara Sidoli, et al. Advances in Understanding High-Mass X-ray Binaries with INTEGRALand Future Directions. *New A Rev.*, 86:101546, 2019. URL http://dx.doi.org/10.1016/j.newar.2020.101546.

R. Krivonos, S. Tsygankov, A. Lutovinov, M. Revnivtsev, E. Churazov, and R. Sunyaev. INTEGRAL/IBIS nine-year Galactic hard X-ray survey. *A&A*, 545:A27, 2012. URL http://dx.doi.org/10.1051/0004-6361/201219617.

Rolf-Peter Kudritzki and Joachim Puls. Winds from Hot Stars. *ARA&A*, 38:613–666, 2000. URL http://dx.doi.org/10.1146/annurev.astro.38.1.613.

K. D. Kuntz and S. L. Snowden. The EPIC-MOS particle-induced background spectra. *A&A*, 478(2):575–596, 2008. URL http://dx.doi.org/10.1051/0004-6361:20077912.

Henny J. G. L. M. Lamers and Joseph P. Cassinelli. *Introduction to Stellar Winds*. 1999.

T. P. Li and Y. Q. Ma. Analysis methods for results in gamma-ray astronomy. *ApJ*, 272:317–324, 1983. URL http://dx.doi.org/10.1086/161295.

Dacheng Lin, Natalie A. Webb, and Didier Barret. Classification of X-Ray Sources in the XMM-Newton Serendipitous Source Catalog. *ApJ*, 756(1):27, 2012. URL http://dx.doi.org/10.1088/0004-637X/756/1/27.

Q. Z. Liu, J. van Paradijs, and E. P. J. van den Heuvel. Catalogue of high-mass X-ray binaries in the Galaxy (4th edition). *A&A*, 455(3):1165–1168, 2006. URL http://dx.doi.org/10.1051/0004-6361:20064987.

Q. Z. Liu, J. van Paradijs, and E. P. J. van den Heuvel. A catalogue of low-mass X-ray binaries in the Galaxy, LMC, and SMC (Fourth edition). *A&A*, 469(2):807–810, 2007. URL http://dx.doi.org/10.1051/0004-6361:20077303.

Malcolm S. Longair. *High Energy Astrophysics*. 2011.

David H Lumb, Norbert Schartel, and Fred A Jansen. XMM-Newton (X-Ray Mulit-Mirror Mission) Observatory. *arXiv e-prints*, arXiv:1202.1651, 2012. URL http://dx.doi.org/10.48550/arXiv.1202.1651.

A. Mainzer, J. Bauer, T. Grav, et al. Preliminary Results from NEOWISE: An Enhancement to the Wide-field Infrared Survey Explorer for Solar System Science. *ApJ*, 731(1):53, 2011. URL http://dx.doi.org/10.1088/0004-637X/731/1/53.

Federico Marocco, Peter R. M. Eisenhardt, John W. Fowler, et al. The CatWISE2020 Catalog. *ApJS*, 253(1):8, 2021. URL http://dx.doi.org/10.3847/1538-4365/abd805.

Rebecca G. Martin, Chris Nixon, Philip J. Armitage, Stephen H. Lubow, and Daniel J. Price. Giant Outbursts in Be/X-Ray Binaries. *ApJ*, 790(2):L34, 2014. URL http://dx.doi.org/10.1088/2041-8205/790/2/L34.

K. O. Mason, A. Breeveld, R. Much, et al. The XMM-Newton optical/UV monitor telescope. *A&A*, 365:L36–L44, 2001. URL http://dx.doi.org/10.1051/0004-6361:20000044.

I. Negueruela, D. M. Smith, P. Reig, S. Chaty, and J. M. Torrejón. Supergiant Fast X-ray Transients: A New Class of High Mass X-ray Binaries Unveiled by INTEGRAL. In A. Wilson, editor, *The X-ray Universe 2005*, volume 604 of *ESA Special Publication*, page 165. 2006. URL http://dx.doi.org/10.48550/arXiv.astro-ph/0511088.

M. Neumann, A. Avakyan, V. Doroshenko, and A. Santangelo. XRBcats: Galactic High Mass X-ray Binary Catalogue. *A&A*, 677:A134, 2023. URL http://dx.doi.org/10.1051/0004-6361/202245728.

F. Ochsenbein, P. Bauer, and J. Marcout. The VizieR database of astronomical catalogues. *A&AS*, 143:23–32, 2000. URL http://dx.doi.org/10.1051/aas:2000169.

Kyuseok Oh, Michael Koss, Craig B. Markwardt, et al. The 105-Month Swift-BAT All-sky Hard X-Ray Survey. *ApJS*, 235(1):4, 2018. URL http://dx.doi.org/10.3847/1538-4365/aaa7fd.

A. T. Okazaki and I. Negueruela. A natural explanation for periodic X-ray outbursts in Be/X-ray binaries. *A&A*, 377:161–174, 2001. URL http://dx.doi.org/10.1051/0004-6361:20011083.

J. R. Oppenheimer and G. M. Volkoff. On Massive Neutron Cores. *Physical Review*, 55(4):374–381, 1939. URL http://dx.doi.org/10.1103/PhysRev.55.374.

M. Orellana and G. E. Romero. Gamma-Ray Emission from Be/X-ray Binaries. *Ap&SS*, 297(1-4):167–178, 2005. URL http://dx.doi.org/10.1007/s10509-005-7618-6.

Feryal Özel and Paulo Freire. Masses, Radii, and the Equation of State of Neutron Stars. *ARA&A*, 54:401–440, 2016. URL http://dx.doi.org/10.1146/annurev-astro-081915-023322.

B. Paczynski and R. Sienkiewicz. Gravitational radiation and the evolution of cataclysmic binaries. *ApJ*, 248:L27–L30, 1981. URL http://dx.doi.org/10.1086/183616.

G. G. Pavlov, D. Sanwal, and M. A. Teter. Central Compact Objects in Supernova Remnants. In Fernando Camilo and Bryan M. Gaensler, editors, *Young Neutron Stars and Their Environments*, volume 218 of *IAU Symposium*, page 239. 2004. URL http://dx.doi.org/10.48550/arXiv.astro-ph/0311526.

Eric Pfahl, Saul Rappaport, and Philipp Podsiadlowski. The Galactic Population of Low- and Intermediate-Mass X-Ray Binaries. *ApJ*, 597(2):1036–1048, 2003. URL http://dx.doi.org/10.1086/378632.

E. Pfeffermann and B. Aschenbach. ROSAT observation of a new supernova remnant in the constellation Scorpius. In H. U. Zimmermann, J. Trümper, and H. Yorke, editors, *Roentgenstrahlung from the Universe*, pages 267–268. 1996.

P. Predehl, R. Andritschke, V. Arefiev, et al. The eROSITA X-ray telescope on SRG. *A&A*, 647:A1, 2021. URL http://dx.doi.org/10.1051/0004-6361/202039313.

A. B. A. Queiroz, F. Anders, B. X. Santiago, et al. StarHorse: a Bayesian tool for determining stellar masses, ages, distances, and extinctions for field stars. *MNRAS*, 476(2):2556–2583, 2018. URL http://dx.doi.org/10.1093/mnras/sty330.

S. Rappaport, P. C. Joss, and R. F. Webbink. The evolution of highly compact binary stellar systems. *ApJ*, 254:616–640, 1982. URL http://dx.doi.org/10.1086/159772.

H. Ritter and U. Kolb. Catalogue of cataclysmic binaries, low-mass X-ray binaries and related objects (Seventh edition). *A&A*, 404:301–303, 2003. URL http://dx.doi.org/10.1051/0004-6361:20030330.

A. W. Rodgers, C. T. Campbell, and J. B. Whiteoak. A catalogue of Hα-emission regions in the southern Milky Way. *MNRAS*, 121:103, 1960. URL http://dx.doi.org/10.1093/mnras/121.1.103.

G. J. Savonije. Roche-lobe overflow in X-ray binaries. *A&A*, 62(3):317–338, 1978.

G. J. Savonije. Roche-lobe overflow and massive X-ray binary systems. *A&A*, 71:352–358, 1979.

G. J. Savonije, M. de Kool, and E. P. J. van den Heuvel. The minimum orbital period for ultra-compact binaries with the helium burning secondaries. *A&A*, 155:51–57, 1986.

Stuart L. Shapiro and Saul A. Teukolsky. *Black holes, white dwarfs and neutron stars. The physics of compact objects*. 1983. URL http://dx.doi.org/10.1002/9783527617661.

J. G. Skellam. The frequency distribution of the difference between two poisson variates belonging to different populations. *Journal of the Royal Statistical Society*, 109(3):296–296, 1946. ISSN 09528385, 23972335. URL http://www.jstor.org/stable/2981372.

M. F. Skrutskie, R. M. Cutri, R. Stiening, et al. The Two Micron All Sky Survey (2MASS). *AJ*, 131(2):1163–1183, 2006. URL http://dx.doi.org/10.1086/498708.

S. L. Snowden, M. R. Collier, and K. D. Kuntz. XMM-Newton Observation of Solar Wind Charge Exchange Emission. *ApJ*, 610(2):1182–1190, 2004. URL http://dx.doi.org/10.1086/421841.

L. Strüder, U. Briel, K. Dennerl, et al. The European Photon Imaging Camera on XMM-Newton: The pn-CCD camera. *A&A*, 365:L18–L26, 2001. URL http://dx.doi.org/10.1051/0004-6361:20000066.

H. Tananbaum, H. Gursky, E. M. Kellogg, R. Levinson, E. Schreier, and R. Giacconi. Discovery of a Periodic Pulsating Binary X-Ray Source in Hercules from UHURU. *ApJ*, 174:L143, 1972. URL http://dx.doi.org/10.1086/180968.

S. A. Tjemkes, E. J. Zuiderwijk, and J. van Paradijs. Optical light curves of massive X-ray binaries. *A&A*, 154:77–91, 1986.

Richard C. Tolman. Static Solutions of Einstein's Field Equations for Spheres of Fluid. *Physical Review*, 55(4):364–373, 1939. URL http://dx.doi.org/10.1103/PhysRev.55.364.

M. J. L. Turner, A. Abbey, M. Arnaud, et al. The European Photon Imaging Camera on XMM-Newton: The MOS cameras. *A&A*, 365:L27–L35, 2001. URL http://dx.doi.org/10.1051/0004-6361:20000087.

M. P. Véron-Cetty and P. Véron. A catalogue of quasars and active nuclei: 13th edition. *A&A*, 518:A10, 2010. URL http://dx.doi.org/10.1051/0004-6361/201014188.

Pauli Virtanen, Ralf Gommers, Travis E. Oliphant, et al. SciPy 1.0: Fundamental Algorithms for Scientific Computing in Python. *Nature Methods*, 17:261–272, 2020. URL http://dx.doi.org/10.1038/s41592-019-0686-2.

N. A. Webb, M. Coriat, I. Traulsen, et al. The XMM-Newton serendipitous survey. IX. The fourth XMM-Newton serendipitous source catalogue. *A&A*, 641:A136, 2020. URL http://dx.doi.org/10.1051/0004-6361/201937353.

N. A. Webb, M. Coriat, I. Traulsen, et al. VizieR Online Data Catalog: XMM-Newton Serendipitous Source Catalogue 4XMM-DR13 (Webb+, 2023). VizieR On-line Data Catalog: IX/69. Originally published in: 2020A&A...641A.136W, 2023.

Edward L. Wright, Peter R. M. Eisenhardt, Amy K. Mainzer, et al. The Wide-field Infrared Survey Explorer (WISE): Mission Description and Initial On-orbit Performance. *AJ*, 140(6):1868–1881, 2010. URL http://dx.doi.org/10.1088/0004-6256/140/6/1868.